2014-04-01

Development and Microscaling of a Novel Glucose Biosensor for Application in a Minimally Invasive Sampling Platform

Jones, Tristan

UNIVERSITY OF CALGARY

Development and Microscaling of a Novel Glucose Biosensor for Application in a Minimally Invasive Sampling Platform

by

Tristan Jones

A THESIS
SUBMITTED TO THE FACULTY OF GRADUATE STUDIES
IN PARTIAL FULFILLMENT OF THE REQUIREMENTS FOR THE
DEGREE OF MASTER OF SCIENCE

DEPARTMENT OF BIOMEDICAL ENGINEERING

CALGARY, ALBERTA
March, 2014

Abstract

Diabetes Mellitus is approaching epidemic proportions in North America and many regions in the world. Current treatment involves self-monitoring of blood glucose levels by analysis of a blood sample obtained by "finger-pricking". This suffers from non-compliance, and samples at a rate much lower than the Shannon frequency of blood glucose levels. The e-Mosquito provides near-painless sampling, is apply-and-forget, and provides a higher sampling rate.

This thesis concerns miniaturiziation of a novel glucose transducer, for integration in the e-Mosquito, that consists of iridium and glucose oxidase on a gold electrode, and which obeys Michaelis-Menten kinetic. The transducers were characterized using their I_{max} and K_m values. Sensors include a transducer, micropotentiostat, power supply, and an ADC that communicates with the e-Mosquito microprocessor.

Testing of the transducer showed current densities of 250-400 $\mu A/cm^2$, though with high inter-transducer variability. The potentiostat was also characterized and demonstrated to have adequate sensitivity and bandwidth.

Acknowledgements

I would like to acknowledge and express my sincerest gratitude to my supervisory committee: Dr. Martin Mintchev, Dr. Viola Birss, and Dr. Karan Kaler. Their unwavering support and assistance allowed this project to happen.

I am also grateful to the examination committee of Dr. Keith Sharkey, Dr. Kartikeya Murari, and Dr. Orly Yadid-Pecht, as well as Dr. Roman Krawetz who volunteered his time to serve as the neutral chair.

It is impossible to overstate the assistance that I have received from the other members of the Birss research group, including Holly Bri Campbell, Corie Horwood, Hany El-Sayed, Scott Paulson, and Jason Young. From the research group of Dr. Mintchev, Alvaro Arrigada provided invaluable advice and assistance on the electronics portion of this project.

I would furthermore like to acknowledge the endless hours of work donated by Mark Toonen, of the glass-making lab, to manufacture our electrodes and electrochemical cells. Tibor Bata of the Department of Electrical Engineering technologist group was invaluable in developing and performing the photolithography technique used to construct the miniaturized transducer.

Funding support for this project was generously provided by research grants from the National Science and Engineering Research Council, and further financial assistance was provided through teaching assistantships provided by the Department of Electrical and Computer Engineering. Without these generous organizations, this project would not have been possible.

My acknowledgements could not be complete without mentioning the support that I received from my parents, Randi Nesset and Michael Jones. Their encouragement, along with that of my partner, Lindsay Brooks (with the occasional exasperated sigh) motivated me to put in the work to finish this project.

This thesis is dedicated to my parents, Randi Nesset and Michael Jones, who taught me to question everything and to try to find out the answers for myself.

Table of Contents

Abstract ii

Acknowledgements iii

Table of Contents v

List of Tables viii

List of Figures ix

List of Abbreviations xiii

1 Introduction 1
- 1.1 Thesis Background and Objectives . . . 1
  - 1.1.1 Project Objectives . . . 2
    - 1.1.1.1 Statement of Hypothesis . . . 3
- 1.2 Diabetes Mellitus (DM) . . . 3
  - 1.2.1 Epidemiology . . . 4
  - 1.2.2 Pathophysiology and Classification . . . 5
    - 1.2.2.1 Insulin-Dependent Diabetes Mellitus (Type 1) . . . 6
    - 1.2.2.2 Non-Insulin-Dependent Diabetes Mellitus (Type 2) . . . 7
  - 1.2.3 Disease Progression and Treatment . . . 8
- 1.3 Michaelis-Menten Kinetics . . . 11
- 1.4 Glucose Sensor History . . . 17
  - 1.4.1 Patch- and Microneedle-based Monitoring Devices . . . 23
  - 1.4.2 Clarke Error Grid . . . 25
- 1.5 The Iridium Oxide-based Glucose Biosensor . . . 27
- 1.6 Enter the Electronic Mosquito . . . 29
  - 1.6.1 Limitations of Current Glucose Monitoring . . . 29
  - 1.6.2 Goals of the Electronic Mosquito . . . 31
  - 1.6.3 Current Prototype . . . 33
    - 1.6.3.1 Blood Sampling Control . . . 34
    - 1.6.3.2 Result Reporting . . . 36

2 Methods for Construction and Testing of Transducer Electrodes 40
- 2.1 Reagents . . . 40

2.1.1 Ir Nanoparticle Sol . . . 41
2.1.2 Glucose Oxidase Solution . . . 41
2.1.3 Nafion® Solution . . . 42
2.1.4 Sulphuric Acid . . . 42
2.1.5 Phosphate Buffer Solution . . . 42
2.1.6 Phosphate Buffered Saline Solution . . . 43
2.2 Working Electrode Preparation . . . 43
2.2.1 Gold Thin Films . . . 44
2.2.1.1 Sputter Deposition on Glass (Silica) Slides . . . 44
2.2.1.2 Sputter Deposition on Poly(methyl methacrylate) (Plexiglass) 45
2.2.2 Deposition of the Glucose-Active Layer . . . 45
2.2.2.1 Electrophoretic Deposition of Glucose Oxidase . . . 47
2.2.2.2 Aliquot Deposition Technique . . . 47
2.2.2.3 Sequential Aliquot Deposition Technique . . . 48
2.3 Electrochemical Methods . . . 48
2.3.1 Electrode Cleaning . . . 48
2.3.2 Iridium Oxidation . . . 49
2.3.3 Glucose Response Characterization . . . 51

3 Characterization of Transducer Glucose Response 53
3.1 Electrophoretically Deposited GOx Electrodes . . . 54
3.1.1 Au Cleaning . . . 54
3.1.2 Ir Oxidation . . . 54
3.1.3 Electrophoretic Deposition of GOx . . . 57
3.1.4 Glucose Response Testing . . . 57
3.1.5 Validation of Michaelis-Menten Model . . . 60
3.2 Aliquot Deposited GOx Electrodes . . . 61
3.2.1 Au Cleaning . . . 61
3.2.2 Ir sol, GOx, and Nafion® Deposition . . . 62
3.2.3 Ir Oxidation . . . 63
3.2.4 Glucose Response Testing . . . 64
3.2.5 Validation of Michaelis-Menten Model . . . 67
3.3 Sequential Aliquot Deposited Electrodes . . . 68
3.3.1 Au Cleaning . . . 69
3.3.2 Ir sol, GOx, and Nafion® Sequential Aliquot Deposition . . . 69
3.3.3 Ir Oxidation . . . 70
3.3.4 Glucose Response Testing . . . 72
3.3.5 Validation of Michaelis-Menten Model . . . 73
3.4 Nanoparticulate Nature of Iridium Sol . . . 74
3.5 Error Analysis . . . 77

3.5.1 Transducer Percent Error Quantification . . . 77
3.5.2 Sources of Error . . . 81
3.5.3 Ir Oxidation Variability and i_{max} and K_m Interaction . . . 82
3.5.3.1 Electrophoretically Deposited Electrodes . . . 83
3.5.3.2 Aliquot Deposited Electrodes . . . 85
3.5.3.3 Sequential Aliquot Deposited Electrodes . . . 86
3.5.4 i_{max} and K_m Interaction . . . 87
3.6 Summary . . . 88

4 Potentiostat Design and Testing **90**
4.1 Existing Systems . . . 90
4.2 Design and Implementation . . . 91
4.2.1 Design Specification . . . 92
4.2.2 Micropotentiostat Design . . . 93
4.2.2.1 The Ideal Operational Amplifier . . . 93
4.2.2.2 Basic Design . . . 95
4.2.2.3 Power Supply . . . 100
4.2.2.4 Analog-to-Digital Conversion and I^2C Interface . . . 103
4.2.3 Component Selection . . . 106
4.2.4 Concentration Calculation . . . 108
4.3 Testing and Validation . . . 109
4.3.1 Potentiostat . . . 109
4.3.2 Combined Counter and Reference Electrode . . . 110
4.3.3 Integrated System . . . 113
4.4 Summary . . . 115

5 Conclusion **117**

6 Future Work **121**

Bibliography **124**

A Michaelis Menten Sensitivity Analysis **132**
A.1 Algebraic Inspection . . . 134
A.2 One Factor At A Time (OFAT) . . . 135

B Transimpedance Amplifier **138**

C Construction Method Flowchart **142**

D Component List **143**

List of Tables

2.1 Volume of glucose solution added to the cell solution per addition. 52

3.1 Electrode performance parameters for electrophoretically deposited test electrodes 60
3.2 Summary of calculated NRMSEs for the electrophoretically deposited GOx electrodes. 61
3.3 Electrode performance parameters for aliquot deposited electrodes 66
3.4 Summary of calculated NRMSEs for the aliquot deposited GOx electrodes. 68
3.5 Electrode performance parameters for sequentially aliquoted test electrodes . 73
3.6 Summary of calculated NRMSEs for the sequential aliquot deposited GOx electrodes. 74
3.7 Summary of p-values for the correlation between the maximum anodic and cathodic IrOx CV currents (i_a and i_c), and the Michaelis-Menten values i_{max} and K_m for the electrophoretically-deposited electrodes. 84
3.8 Summary of p-values for the correlation between the maximum anodic and cathodic IrOx CV currents (i_a and i_c), and the Michaelis-Menten values i_{max} and K_m for the aliquot deposited electrodes. 85
3.9 Summary of p-values for the correlation between the maximum anodic and cathodic IrOx CV currents (i_a and i_c), and the Michaelis-Menten values i_{max} and K_m for the aliquot deposited electrodes. 87

List of Figures

1.1 Worldwide prevalence of all forms of diabetes mellitus (%) 5
1.2 Varying concentration of substrate S, enzyme E, complex ES, and product P over time according to Michaelis-Menten kinetics. 14
1.3 Comparison of numerically differentiated Michaelis-Menten plot with the steady-state prediction. 17
1.4 3D structure of glucose oxidase enzyme from *Aspergillus niger* 18
1.5 The mediator chain used in common glucose-sensing electrodes. The GOx enzyme and mediator are alternately reduced and oxidized, with the net effect of transporting negative charge from the glucose molecule to the electrode. The dotted line shows the 'path' of the electrons from the glucose molecule to the electrode via the enzyme and the mediator. 19
1.6 The original Clarke Error Grid. 27
1.7 Sample glucose levels monitored continuously over the course of a day 30
1.8 CAD drawing of the e-Mosquito patch. 32
1.9 The e-Mosquito contains a matrix of individual blood-sampling 'cells' that can be addressed individually. This schematic shows a sample matrix having three columns of addressable cells and n rows. The structure of an individual cell is shown in Figure 1.10. 32
1.10 Schematic of an individual e-Mosquito cell. Piezoelectric bending cantilevers (a) actuate the sampling platform (b) downwards into the patient's skin (c). The microneedle (d) then penetrates to an appropriate depth to retrieve a blood sample in the sampling and sensing chamber (e). The entire platform is then retracted from the skin and the sample is analyzed and the result communicated to the control electronics by electrical leads (f). 33
1.11 Cross-sectional diagram of human skin, with relevant structures labeled . . . 34
1.12 Descent profile of the feedback-controlled microneedle. 35
1.13 High-level overview of a closed-loop artificial pancreas. 36
1.14 CAD rendering of the large-scale e-Mosquito prototype. 37
1.15 Plot of the actuator potential and the glucose-detection signal vs. time. . . . 38
1.16 Block-diagram of the wireless control scheme. This shows both the transceiver on the e-Mosquito, and the USB-based transceiver dongle used on the PC side. 39

2.1 Mask pattern for the PMMA electrodes 46
2.2 Cross-sectional view of the layers on a complete glucose-sensitive electrode . 46
2.3 Diagrammatic view of the electrochemical cell 49

2.4 Cyclic voltammogram of gold in H_2SO_4 50

3.1 Plot of final Au cleaning CVs for the electrophoretically deposited electrodes. 55
3.2 Sample CV showing the conversion of Ir to IrOx over the course of 65 CV cycles for the electrophoretically deposited electrodes. 55
3.3 Superimposed plots of the final (65^{th}) Ir oxidation cycle for all electrophoretically deposited electrodes. 56
3.4 Example of the conversion of time-based glucose addition plot to Michaelis-Menten plot. 58
3.5 Michaelis-Menten plots for four different electrophoretically deposited electrodes. 59
3.6 Plot of final Au CVs for the aliquot deposition electrodes. 62
3.7 Sample CVs showing the conversion of Ir to IrOx over the course of 65 CV cycles for the aliquot deposited GOx electrodes. 63
3.8 Superimposed plots of the final (65^{th}) Ir oxidation cycle for all aliquot deposited GOx electrodes. 64
3.9 Michaelis-Menten plots for the aliquot deposited electrodes. 65
3.10 Photo showing the aggregation that resulted from combined drying of ethanolic and aqueous solutions. 67
3.11 Plot of final Au cleaning CVs for the sequentially aliquoted electrodes. 69
3.12 Sample CV showing the conversion of Ir to IrOx over the course of 65 CV cycles for the sequential aliquot deposited electrodes. 70
3.13 Superimposed plots of the final (65^{th}) Ir oxidation CVs for all sequential aliquot deposited electrodes. 71
3.14 Michaelis-Menten plots for the sequentially aliquoted electrodes. 72
3.15 Region of the CV that was integrated to determine the amount of charge transferred by underpotential adsorption of hydrogen. 75
3.16 Mathematical model of the e-Mosquito sensor used for error quantification . 78
3.17 Error plot used in quantifying the error of individual glucose transducers . . 80
3.18 Example of the maximum anodic and cathodic currents on a sample Ir oxidation CV. 83
3.19 Correlation plot of i_{max} (left) and K_m (right) with the anodic and cathodic currents for the electrophoretically deposited electrodes. 84
3.20 Correlation plot of i_{max} (left) and K_m (right) with the anodic and cathodic currents for the aliquot deposited electrodes. 85
3.21 Correlation plot of i_{max} (left) and K_m (right) with the anodic and cathodic currents for the sequentially aliquoted electrodes. 86
3.22 Interaction plot of K_m (x-axis) vs. i_{max} (y-axis). 88

4.1 Schematic representation of an operational amplifier and the various connections and signals associated with it. 93
4.2 Schematic of the relationship between the output and load impedances of an opamp. As can be seen, this is essentially a simple voltage divider. 95
4.3 Simple representation of a two-electrode electrochemical experiment. The voltage, V_{in}, maintains the working electrode (WE) at a particular potential relative to the reference electrode (RE) and is quite commonly varied in time. The resulting current is measured (I_{meas}) and plotted against the potential. The electrochemical solution in which the electrodes are immersed can be conceptualized as a non-linear complex impedance. 96
4.4 Simple scheme of a three-electrode potentiostat. The operational amplifer causes a current to flow out of the counter electrode (CE) that maintains the specific potential V_{in} between the reference electrode (RE) and the working electrode (WE) at ground. The impedance of the interfaces and the bulk solution under test are represented by Z1 and Z2. 97
4.5 Buffered version of Figure 4.4. The feedback buffer is important to ensure that the current flow out of node RE is effectively zero. 99
4.6 Final circuit design for the e-Mosquito potentiostat. A transimpedance amplifier is used as a nearly-ideal ammeter attached to the working electrode. . 100
4.7 Application/implementation circuit for DC-to-DC voltage step up used to convert +3V DC to +5V DC using the MAX856 IC for high-frequency voltage conversion. 101
4.9 Final circuit design of the e-Mosquito potentiostat's power supply, including the TLE2426 railsplitter. 102
4.8 Resistive virtual ground circuit. With an infinite (or very large) load impedance, the virtual ground is approximately centred between the two rails. However, with a non-infinite load, the virtual ground will deviate from its correct value. 103
4.10 Final circuit design for the e-Mosquito potentiostat. A transimpedance amplifier was used as a nearly-ideal ammeter attached to the working electrode. 104
4.11 CAD layout of the e-Mosquito potentiostat PCB. 107
4.12 The simulated test cell used to validate the potentiostat design. This test cell is known as the "simplified Randles' cell" and has a known and characteristic electrochemical response. 110
4.13 Expected result of a cyclic voltammetry experiment performed on the simplified Randles' cell (Figure 4.12). This was calculated from the known constraints imposed on a cell by an ideal potentiostat. The inset shows the same data formatted in the classical cyclic voltammagram format. 111
4.14 Recorded trace of the physical prototype potentiostat as connected to a physical simplified Randles' cell. 112
4.15 Photo of an unused micro-transducer. 113

4.16 The results from three tests of the complete system. This was performed using the 2-electrode micro-transducer design in conjunction with the micropotentiostat described in this chapter. The test was performed in PBSS under air (no argon was used to deoxygenate the test solution) and without stirring of the test cell solution. The average measured current for each step was computed by the e-Mosquito microprocessor and communicated to the control PC via the wireless communication system onboard the prototype. 115

A.1 Model of the complete e-Mosquito system used for error analysis 134

B.1 Conceptual circuit diagram of the micropotentiostat circuit. 138
B.2 Illustration of the variable voltage drop between the working electrode and ground. 139
B.3 Schematic of a current-to-voltage converter — a transimpedance amplifier. The input current flows entirely through the resistor R, giving rise to a voltage of $I_{in} \cdot R$ at the output. 140

C.1 Flowchart showing the various construction methods used to create transducers. 142

D.1 Final circuit design for the e-Mosquito potentiostat. 143

List of Abbreviations

$[G]$	Concentration of glucose
$[G]_{reported}$	Glucose concentration that is actually reported to the user by the e-Mosquito glucose sensor
$[G]_{true}$	Physical concentration of glucose in a sample solution or blood sample
e^-	Electron
I^2C	Inter-Integrated Circuit communication standard
I_{max}	Michaelis-Menten maximal rate constant, in terms of electrical current
i_{max}	Michaelis-Menten maximal rate constant, in terms of electrical current per unit surface area
I_{meas}	Output current from the glucose sample cell that is measured by the micropotentiostat
k_f	Rate constant of the forward reaction of substrate and enzyme binding to form an enzyme-substrate complex as described by the Michaelis-Menten enzyme kinetics model
K_m	Michaelis-Menten rate constant
k_r	Rate constant of the reverse reaction of substrate and enzyme binding to form an enzyme-substrate complex as described by the Michaelis-Menten enzyme kinetics model
k_{cat}	Rate constant for the product formation reaction that is catalysed by the enzyme as described by the Michaelis-Menten enzyme kinetics model
AC	Alternating Current
ADC	Analog-to-Digital Converter
BAN	Body-Area Network, a theoretical communication network for a persons own medical devices
BG	Blood Glucose
BGSM	Blood Glucose Self-Monitoring
CE	Counter or Current Electrode
CV	Cyclic Voltammetry or Cyclic Voltammogram
DC	Direct Current
DCCT	Diabetes Control and Complications Trial

DKA	Diabetic Ketoacidosis
DM	Diabetes Mellitus
DM1	Type 1 Diabetes Mellitus
DM2	Type 2 Diabetes Mellitus
e-Mosquito	Electronic Mosquito
FAD	Flavin Adenine Dinucleotide cofactor
$FADH_2$	Flavin Adenine Dinucleotide cofactor, reduced form
GLUT	Glucose Transport Enzyme
GND	Circuit Physical Ground
GOx	Glucose Oxidase Enzyme
HHS	Hyperglycemic Hyperosmolar Syndrome
IDDM	Insulin-Dependent Diabetes Mellitus
Ir	Iridium
IrOx	Iridium Oxide
MM	Michaelis-Menten
NIDDM	Non-Insulin-Dependent Diabetes Mellitus
NP	Nanoparticle
NRMSE	Normalized Root Mean-Squared Error
PBS	Phosphate Buffer Solution
PBSS	Phosphate-Buffered Saline Solution
PCB	Printed Circuit Board
RE	Reference Electrode
RHE	Reversible Hydrogen Electrode
SWCNT	Single-Walled Carbon Nanotubes
UKPDS	United Kingdom Prospective Diabetes Study
USD	United States of America Dollar
VGND	Virtual Ground
WE	Working Electrode

Chapter 1

Introduction

1.1 Thesis Background and Objectives

The primary goal of this project is the integration of a glucose sensing system into the e-Mosquito prototype. The e-Mosquito is a patch-based glucose sensing device currently being developed at the University of Calgary to improve blood-sugar monitoring for diabetics. The device itselfs is described in more detail in Section 1.6. Previous industry feedback regarding the e-Mosquito has indicated that this is a requirement prior to further commercialization of the device by biomedical device companies.

Throughout this thesis, the term 'transducer' is used to refer to the electrochemical electrode itself. This is the device that transforms the chemical concentration of glucose into an electrical current. Miniaturization of a novel glucose transducer being developed in the Birss lab at the University of Calgary was undertaken for this project. This transducer was chosen as it promises high current densities, which are an asset in small-scale sensor designs. In addition, the geographic proximity of the research group working on this transducer was a positive factor. The transducer design, construction, and testing is presented in Chapters 2 and 3.

The term 'sensor' is used to refer to the complete integrated system, while 'sensor electronics' refers to the electronics that operate the transducer. These electronics included a small-scale potentiostat to operate the three-electrode glucose transducers. This is important to avoid polarization of the reference and working electrodes, which would result in unpredictable results. The electronics also included a power supply, analog-to-digital converter,

and communications bus, all of which were designed and tested with an existing prototype of the e-Mosquito device. The sensor electronics work is primarily presented in Chapter 4.

1.1.1 Project Objectives

1. Transducer miniaturisation (Chapters 2 and 3)
    - Characterization of transducer response and reproducibility using a 3-electrode test-bed. A 3-electrode system was selected as it is theoretically more precise than a 2-electrode system (less effect of electrode polarization), and because the existing large-scale sensor uses a 3-electrode system for analysis. Finally, a 3-electrode system can easily be used as a 2-electrode system, but the reverse is not true. Thus a 3-electrode system is more generalizable and flexible for future applications.
    - Comparison of transducer construction techniques using:
        - **Iridium Oxide (IrOx)** was selected for this work as it is biocompatible and conductive [1], making it ideal for biosensor application. The IrOx nanoparticles originate as iridium nanoparticles which are then electrochemically oxidized. Under the electrochemical conditions that the sensor operates at (1.2 V vs. RHE), the iridium oxide will be in an oxidized state regardless.
        - **Glucose Oxidase (GOx)** is an enzyme that oxidizes glucose molecules. It was used in the sensor to provide specificity for glucose and to avoid interference as much as possible.The oxidation of glucose produces electrons that are easily detectable by an external electrical circuit, making GOx ideal for sensing purposes.
        - **Nafion®** is a semi-permeable material that acts as a binding agent in the Birss glucose biosensor [2]. It allows cations and small neutral molecules to pass, but blocks anions and large molecules. It has been shown in the past to block many interfering species in glucose biosensors, such as acetaminophen

and uric acid [3].

- Miniaturization of transducer for existing e-Mosquito prototype

2. Sensor electronics development (based on transducer characteristics determined in part 1) (Chapter 4)
   - Design, manufacture, and testing of prototype small-scale potentiostat
   - Design and testing of supporting electronics

     Bipolar power supply

     Analog-to-digital conversion

     Communication bus

1.1.1.1 Statement of Hypothesis

The underlying hypothesis of this thesis work was that a transducer consisting of iridium oxide nanoparticles, glucose oxidase, and Nafion® deposited on a gold substrate could produce a consistent and reproducible sensor with good current density and sample-to-sample variability of less than 25 %, while operated by an in-house custom potentiostat.

1.2 Diabetes Mellitus (DM)

In 1922, Dr. Frederik Banting and his lab assistant, Charles Best, published a paper that changed the lives of millions of people worldwide. Their article, published in the Journal of Laboratory and Clinical Medicine, was the first to demonstrate the effect of pancreatic extract (insulin) in lowering the blood glucose concentration in dogs [4]. This discovery is the direct precursor of modern diabetes treatment, with all of its complexity of insulin regimes and blood glucose monitoring. In order to understand the reason for the complexity of insulin regimens, and the manner in which the Electronic Mosquito revolutionizes this treatment, a basic understanding of the diabetic disease process is required.

1.2.1 Epidemiology

There is little doubt that diabetes mellitus (DM) is one of the great modern health issues. Estimations of prevalence put the number of adults afflicted worldwide at 285 million in 2010, or 6.4 %, with this number predicted to rise to 439 million (7.7 %) by 2030 [5]. In terms of expenditure, this represents an estimated 376 billion USD in 2010, projected to rise to 490 billion USD by 2030. Clearly this represents enormous expenditure and burden on health care systems worldwide, not to mention the indirect costs associated with morbidity and decreased productivity resulting from the disease.

In addition to the economic burden of diabetes, the effect on morbidity and mortality is equally or more important. Analysis of the prominent Framingham Heart Study dataset demonstrated an average reduction in life expectancy of 7.5 to 8.2 years for men and women, respectively [6]. The same study also demonstrated that diabetes resulted in 7.8 to 8.4 fewer years of life free of cardiovascular disease [6].

Well-known associations exist between dietary and lifestyle factors and development of DM, including diets high in fats and sugars, and low levels of exercise. There are also significant genetic risk factors (more predominant in type 1 vs. type 2 diabetes, but present in both) that are sometimes less well-known among laypersons. The combination of lifestyle factors and genetic predisposition leads to an interesting geographical prevalence as well. There are well-known "hotspots" of DM in developed countries, such as Canada, the United States, and Australia. However, the highest prevalence of the disease in the modern world exists in Mexico, Egypt, and Saudi Arabia [7]. Figure 1.1 shows the International Diabetes' Federation's Atlas of Diabetes prevalence per country metric, clearly demostrating this preponderance of disease in North America and the Middle East.

There are two major forms of DM, 'type 1' and 'type 2'. Another very similar classification is as 'insulin-dependent diabetes mellitus' (IDDM) and 'non-insulin-dependent diabetes mellitus' (NIDDM). Both have similar effects on the patient, but are caused by substantially

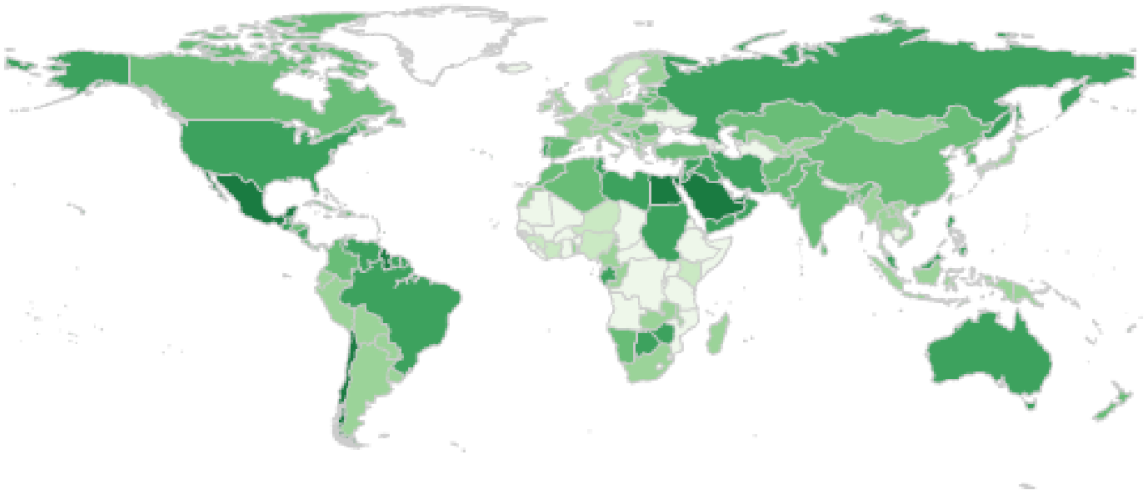

Figure 1.1: This figure shows the prevalence of diabetes mellitus (all types) on a country-by-country basis. Darker green is higher prevalence, with the darkest green (e.g., Mexico or Saudi Arabia) being greater than 12 % prevalence [7].

different mechanisms, and both have differing expression and prevalence in the worldwide population. Type 1 diabetes is an auto-immune process resulting in reduced insulin production, and constitutes roughly 5 % - 10 % of all diabetes [8, 9]. This amounts to over 1 million type 1 diabetics in the United States of America alone who are dependent on some form of insulin dosing for survival. There are additionally a subset of type 2 diabetics who progress to become insulinopenic and hence dependent on exogenous insulin administration as well, amounting to approximately 25 % of diabetics over the course of their lifetime [9]. This represents a large patient population who require frequent blood glucose monitoring, and that could benefit directly from a feedback-controlled artificial pancreas in the future.

1.2.2 Pathophysiology and Classification

The term 'diabetes mellitus' (DM) refers to the group of metabolic disorders that are characterized by abnormally high concentrations of glucose in a person's blood. This condition

can arise from several differing mechanisms, and is traditionally classified as either type 1 or type 2. There are several other nomenclatures as well, which will be mentioned in the relevant sections. There are also some less common variants, the most widely-known being gestational diabetes. This form arises in pregnant women as a result of their pregnancy and generally resolves after delivery (though it confers an increased risk of developing type 2 diabetes later on). As this form of diabetes is similar in mechanism and effect to type 2 diabetes, it will not be discussed in depth.

In a healthy individual, the peptide hormone insulin is produced by the islet β-cells of the pancreas, and has a huge variety of effects on different types of tissue. The most important and well known effect is its regulation of the concentration of glucose in a human being's blood, denoted as $[Glucose]$. This is accomplished through a variety of insulin-sensitive glucose transporters, the most important of which is the GLUT4 protein. This protein is found predominantly in adipose tissue and striated skeletal muscle cells where insulin both induces translocation of GLUT4 to the cell membrane and opens the enzyme channel, allowing passive diffusion of glucose down its concentration gradient out of the blood and into the cell. Once inside the cell, glucose is either glycolysed for energy or stored in the cell as glycogen. Either of these processes deplete the glucose inside the cell and hence maintain the concentration gradient that moves glucose into the cell and removes it from the circulating bloodstream. If insulin is not present, or if cells are not properly "sensitive" to it, the GLUT receptor is not translocated to the cell surface, does not open, and the glucose cannot diffuse into the cell. Instead, the glucose is 'stuck' in the bloodstream where it builds up, eventually to toxic levels.

1.2.2.1 Insulin-Dependent Diabetes Mellitus (Type 1)

Insulin-dependent diabetes mellitus has also been known as juvenile-onset diabetes or type 1 diabetes (DM1). This classification refers to diabetes that arises as a result of insufficient endogenous insulin production, resulting in chronic elevation of plasma glucose concentration.

Possible aetiologies for this lack of production include autoimmune mechanisms, iatrogenic causes, and as a secondary result of another disease process.

The most commonly recognized variant of IDDM or DM1 is autoimmune or 'juvenile diabetes', so named as it often manifests in childhood. There are a variety of genes that have been associated with the development of type 1 diabetes, and a variety of β-cell autoantibodies that can be measured and confer risk of disease development, indicating that there is some genetic component to the disease [10]. The traditional view is that of a genetic predisposition with an environmental inciting trigger, although it is becoming increasingly apparent that there are a large variety of pathologies that contribute to development of the disease [11].

In some patients with chronic pancreatitis, a complete surgical resection of the pancreas can be curative, and can have a beneficial impact on quality of life [12, 13]. However, this procedure often means removal of most or all of a patient's β-islet cell tissue, and approximately 41 % of these patients will become insulin-dependent diabetics [12]. Management of these patients is classically considered 'brittle', although they can still be managed in a similar fashion to normal type 1 diabetics [14, 13].

Finally, IDDM can be the result of another disease. Chronic pancreatitis is a common example, accounting for 5 % - 10 % of all IDDM patients [15]. The prolonged damage to the pancreas by inflammation and leakage of protease enzymes eventually results in an insufficient number of islet cells to maintain glucose homeostasis [15]. In addition, many type 2 diabetics will eventually require exogenous insulin in order to control their disease, and become, in a sense, 'insulin-dependent' [16, 8].

1.2.2.2 Non-Insulin-Dependent Diabetes Mellitus (Type 2)

Type 2 diabetics have fully functional pancreatic islet cells (at least initially) and measurable levels of insulin in their blood. This disease has also historically been referred to as adult-onset diabetes or non-insulin-dependent diabetes mellitus (NIDDM). While insulin is still

produced by the pancreas, the cells in the body become resistant to its effects. The liver, on which insulin typically has an inhibiting effect, begins to release too much glucose into the bloodstream. Conversely, the cells composing skeletal muscle and adipose tissue are stimulated by insulin to take up glucose into their intracellular space; this process is also inhibited by increased insulin resistance [17].

The end result of this process is chronically elevated blood glucose levels that cause damage to other tissues. This damage is known to be caused by reactive oxygen species (ROS) [18] that are generated by impairment of the mitochrondrial electron transport chain. ROSs then damage cells via oxidative stress, i.e., rapid oxidation of key proteins and DNA, that often causes cell apoptosis [19, 20].

The causes of DM2 are well publicized and known by the general public, but the actual mechanisms by which they lead to the disease are less clear. There are a huge number of both lifestyle and genetic factors that have been linked to diabetes, including obesity, poor diet and lack of exercise [9]. Patients' genotypes are also known to play a role, with Poulsen et al. finding a 50 % concordance in development of diabetes in a monozygotic twin study [21].

Iatrogenic causes of diabetes mellitus also exist, the most common of which is administration of exogenous glucocorticoids. These medications both increase cell resistance to the effects of insulin, and upregulate gluconeogenesis in the liver. This results in pathologically elevated blood sugar levels [22].

1.2.3 Disease Progression and Treatment

Aside from the economic cost of the various forms of diabetes, there is a human cost as well. Diabetes is almost unrivaled in terms of the mortality and morbidity that it can incur, and this results predominantly from excess glucose in the blood compartment. Two landmark studies demonstrate this nicely by randomizing patients to various levels of glucose control and demonstrating that tighter glycemic control resulted in fewer long-term

complications. The UK Prospective Diabetes Study (UKPDS) enrolled nearly 4,000 type 2 diabetics and randomized them to either intensive or conventional glycemic control. 40.9 % of intensively-controlled patients developed complications of their disease, compared to 46.0 % of conventionally-controlled patients (p=0.029) [23].

The Diabetes Control and Complications Trial (DCCT) undertook a similar trial for the type 1 diabetic population. This trial enrolled 1,441 patients and also randomized them to either conventional or intensive glycemic control. In the DCCT trial, the incidence of retinopathy, nephropathy, and neuropathy were all reduced by a statistically significant amount [24].

The results from both of these trials, along with an assortment of other smaller trials, suggest that development of complications from diabetes is related to the excess glucose located in the patient's circulation. As a result, modern treatment of diabetes centres around control of glucose concentrations while avoiding potentially dangerous side-effects, such as hypoglycemia [9].

In addition to the chronic tissue damage caused by diabetes, patients are at risk of acute complications as well. Type 1 diabetics typically present with diabetic ketoacidosis (DKA) when they have inadequate insulin administered to meet their body's needs. The body's adipose tissue begins to consume fatty acids due to the low insulin levels, producing ketone bodies and acidifying the blood, resulting in metabolic ketoacidosis. In addition, the excess blood glucose concentration (often $> 20\,\text{mmol/L}$) in the blood leads to an osmotic diuresis, causing dehydration [25]. Untreated DKA is a disorder with high mortality, and the primary reason that type 1 diabetics did not survive into adulthood prior to the availability of exogenous insulin [17]. Type 2 diabetics suffer a similar syndrome, named hyperglycemic hyperosmolar syndrome (HHS). HHS consists principally of osmotic diuresis and dehydration induced by very high blood glucose levels, but does not involve ketosis as type 2 diabetics still typically have sufficient circulating insulin to prevent unregulated fat metabolism [9, 22].

Current treatment of diabetes differs significantly between type 1 and type 2 due to their

differing etiologies. Type 2 diabetics can be controlled for many years by diet, exercise, and oral hypoglycemic agents, before it is necessary to provide exogenous insulin [9]. This thesis is concerned primarily with glucose control in insulin-dependent individuals.

The cornerstone of insulin-dependent diabetic management is self-measurement of blood glucose concentrations at home by the use of a glucometer. This allows patients to appropriately dose their insulin in response to their current needs [9, 26]. The history of blood-glucose self monitoring (BGSM) technology is reviewed in the next section. The data provided by BGSM devices allow the patient to adjust their insulin dosing to account for daily variations in their glucose levels that can be caused by factors such as physical activity, dietary changes, and illness.

There are many different insulin analogues that are available and that vary primarily in their duration and onset of effect, and there are as many differing insulin-dosing regimes [27]. The most commonly used are once-, twice-, or thrice-daily insulin boluses, and basal-bolus. In the bolus regimens, insulin is taken with meals and is titrated directly according to the patient's BGSM reading. No insulin is taken between meals and hence blood sugar levels are relatively uncontrolled [27]. The basal-bolus regimen uses long acting (12- or 24-hour period of effect) 'basal' insulin, administered either once or twice daily, and then boluses at meals, again titrated to measured blood glucose levels. This provides superior glycemic control between meals, although there is an increased risk of hypoglycemia, especially overnight when carbohydrate intake is non-existent but insulin is still present [28]. It is often difficult to determine that these hypoglycemic episodes are occurring, as symptoms are not noted while the patient is asleep. Prolonged hypoglycemia can lead to coma and death [29].

In a non-diabetic patient, the primary defence against hypoglycemia is glucagon, a peptide hormone secreted by α-cells in the pancreas. This hormone acts to raise blood glucose levels through mechanisms such as hepatic gluconeogenesis [17]. Hypoglycemia also causes release of epinephrine, which leads to the clinical symptoms of tachycardia, diaphoresis, and general malaise that can serve to warn patients of their hypoglycemia. In patients with

frequent hypoglycemic episodes, these responses are blunted and hence the risk of severe hypoglycemic coma, heart arrhythmias, or death is increased [17]. As a result, it is very important for the BGSM protocol to allow detection of these events so that the blood glucose concentration can be rectified.

There have been attempts to replace the exogenous function of the human pancreas in type 1 diabetics, culminating in islet-cell transplantation, termed the Edmonton Protocol [30, 31]. Cadaveric islet cells are purified by digestion of the pancreatic collagen matrix and centrifuge extraction of individual islets, which are then injected into the portal venous circulation and deposited in the liver. Patients undergoing the treatment have been shown to be insulin-independant following the procedure for a period of years, but there remains a reasonable rate of relapse to an insulin-dependent state [32, 31]. In addition, transplanted α-cells show no response to circulating glucose levels and do not produce glucagon. Hence, the Edmonton protocol is moderately effective for the treatment of hyperglycemia, but does not protect against hypoglycemia [30].

1.3 Michaelis-Menten Kinetics

A model for the transfer function of the glucose transducers allows the e-Mosquito to calculate a measured glucose concentration from the electrical current measured by the electrode. The Michaelis-Menten model of enzyme kinetics provide an accurate correlation between reaction rate (and hence electron current) and glucose concentration for single-enzyme, single-substrate reactions. The steady-state approximation of the Michaelis-Menten model of enzyme kinetics results in the standard form of the Michaelis-Menten equation (Equation 1.1, where v is the instantaneous reaction rate, v_{max} is the maximum reaction rate, $[S]$ is the substrate concentration, and K_m is the Michaelis-Menten constant.), and this is the equation used in this thesis. The present section gives an overview of the Michaelis-Menten kinetic

model and the derivation of the steady-state equation.

$$v = \frac{v_{max}[S]}{K_m + [S]} \tag{1.1}$$

The classic approach to enzyme kinetics was laid out by Leonor Michaelis and Maud Menten in 1913 [33]. The prototypical enzyme chemical reaction involved the reversible binding of the substrate and enzyme to form an enzyme-substrate complex. This complex then catalyzes the transformation of the substrate into the product, while regenerating the enzyme. This is shown in Reaction 1.2, with S representing the substrate molecule, E representing the enzyme, ES representing the enzyme-substrate complex, and P representing the product. This equation also shows the rate constants for the relevant reactions: k_f is the rate constant of the forward enzyme-binding reaction, k_r is the rate constant for the reverse reaction (unbinding of the complex back into substrate and free enzyme), and k_{cat} is the rate constant for the catalyzed product-forming reaction.

$$\mathrm{S} + \mathrm{E} \underset{k_r}{\overset{k_f}{\rightleftharpoons}} \mathrm{ES} \xrightarrow{k_{cat}} \mathrm{E} + \mathrm{P} \tag{1.2}$$

The rate at which a reaction proceeds is determined by the 'rate equation'. For a generic chemical reaction, such as the one shown in Reaction 1.3, the rate equation has the generic form shown in Equation 1.4 (the square brackets represent the concentration of the enclosed chemical species). This relates the rate constant k to concentration of chemical species A and B, adjusted for the 'order' of the reaction associated with each species (denoted by x and y). The rate of the reaction can then be correlated to the rate of change of the concentrations of the various species, appropriately scaled by their stoichiometric coefficients.

$$\mathrm{aA} + \mathrm{bB} \xrightarrow{k} \mathrm{cC} \tag{1.3}$$

$$rate = k[A]^x[B]^y = -\frac{1}{a} \cdot \frac{d[A]}{dt} = -\frac{1}{b} \cdot \frac{d[B]}{dt} = +\frac{1}{c} \cdot \frac{d[C]}{dt} \tag{1.4}$$

Generalizing the generic rate equation to the Michaelis-Menten chemical equation (Reaction 1.2), representing an enzymatic reaction (where all stoichiometric coefficients are 1), results in a set of 4 simultaneous ODEs that describe the time variation of the concentration of the 4 chemical species involved, as shown in Equations 1.5, 1.6, 1.7, and 1.8.

$$\frac{d[E]}{dt} = -k_f[E][S] + k_r[ES] + k_{cat}[ES] \tag{1.5}$$

$$\frac{d[S]}{dt} = -k_f[E][S] + k_r[ES] \tag{1.6}$$

$$\frac{d[ES]}{dt} = +k_f[E][S] - k_r[ES] - k_{cat}[ES] \tag{1.7}$$

$$\frac{d[P]}{dt} = +k_{cat}[ES] \tag{1.8}$$

This system of equations can be solved by numerical integration methods to yield a plot showing the variation of enzyme, substrate, complex, and product over time (Figure 1.2). This figure was generated using arbitrary rate constants in order to clearly demonstrate the variation in concentrations, and, as such, does not represent any real chemical reaction. As time progresses, the substrate concentration diminishes while the product concentration rises, reflecting the overall conversion reaction of substrate into product that is catalyzed by the enzyme. The concentration of free enzyme initially decreases as it binds the substrate, but then begins increasing again as the complex dissociates into product and releases free enzyme back into the solution. This reaction approaches a steady-state value over time, and is also reflected in the complex concentration which follows the opposite trend.

Haldane and Briggs did further analysis of this chemical system in 1925 and developed the *steady-state approximation* for Michaelis-Menten kinetics [34]. This approximation makes the assumption that the reaction rapidly reaches and maintains a state of equilibrium, and

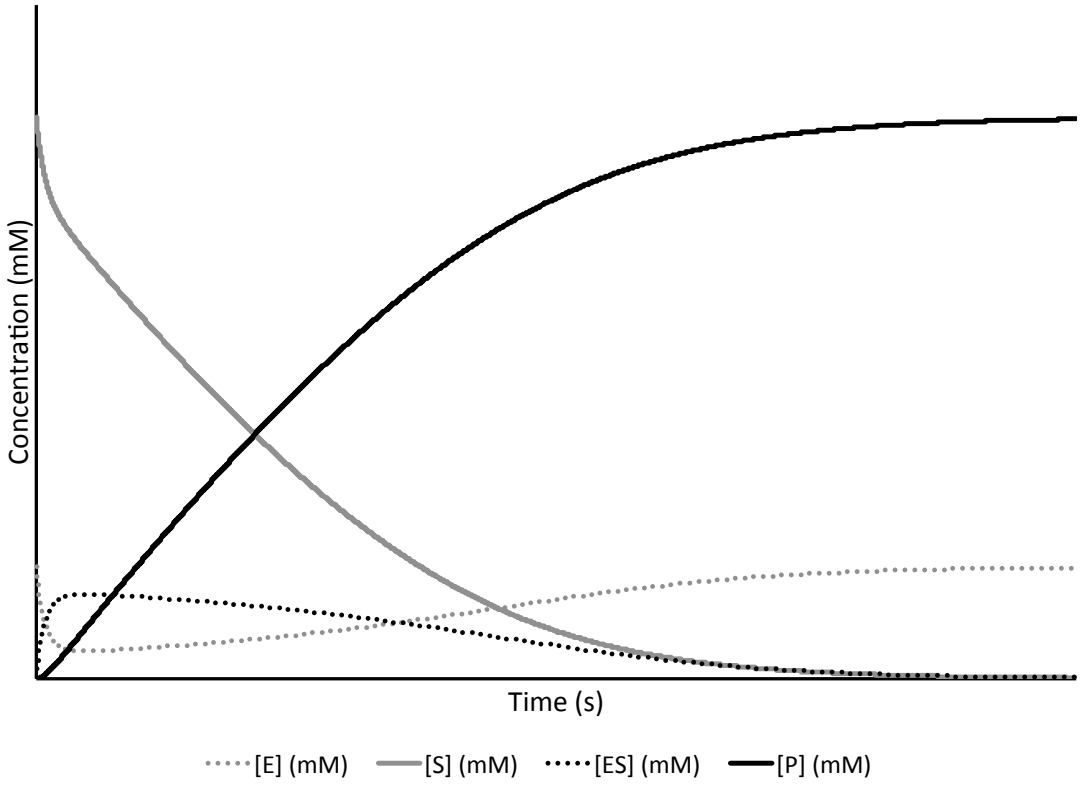

Figure 1.2: Varying concentration of substrate S, enzyme E, complex ES, and product P over time according to Michaelis-Menten kinetics. This plot is a result of arbitrary values for k_f, k_r, and k_{cat} that were chosen in order to clearly show the variation in species concentration over time. The plot was obtained by use of 4^{th} Runge-Kutta numerical integration.

thus that the same amount of complex is generated as is dissociated, with the concentration of complex ES remaining unchanged (Equation 1.9). The second assumption is quite self-evident, and is simply that the total concentration of free enzyme at any point in time is equivalent to the initial amount of enzyme ($[E]_0$) less however much currently exists as part of the complex (Equation 1.10).

$$\frac{d[ES]}{dt} = 0 \tag{1.9}$$

$$[E] = [E]_0 - [ES] \tag{1.10}$$

A useful quantity to measure in enzyme reactions is the rate of formation of the product, or $d[P]/dt$, as this is the outcome of the reaction. By combining the system of ODEs above (Equations 1.5 – 1.8) with the assumptions in Equations 1.9 and 1.10, it is possible to derive an expression for the reaction velocity, $v = d[P]/dt$, under steady state conditions. This expression is found in Equation 1.11.

using 1.9:
$$0 = k_r[ES] + k_{cat}[ES] - k_f[E][S]$$
$$[ES] \cdot (k_r + k_{cat}) = k_f[E][S]$$

using 1.10:
$$[ES] \cdot (k_r + k_{cat}) = k_f[S]([E]_0 - [ES])$$
$$[ES] \cdot (k_r + k_{cat}) = k_f[S][E]_0 - k_f[S][ES]$$
$$[ES] \cdot (k_r + k_{cat} + [S]k_f) = k_f[S][E]_0$$
$$[ES] = \frac{[E]_0[S]k_f}{k_r + k_{cat} + [S]k_f}$$

using 1.8:
$$\frac{d[P]}{dt} = v = \frac{k_{cat}[E]_0[S]}{\frac{k_r + k_{cat}}{k_f} + [S]} \tag{1.11}$$

$$\frac{d[P]}{dt} = v = \frac{v_{max}[S]}{K_m + [S]} \tag{1.12}$$

Equation 1.12 shows the standard form of the Michaelis-Menten equation as originally presented. From this, it is trivial to obtain expressions for the K_m and v_{max} constants in terms of the rate constants and the total amount of enzyme present. These relationships are shown in Equation 1.13 for v_{max} and Equation 1.14 for K_m.

$$v_{max} = k_{cat}[E]_0 \tag{1.13}$$
$$K_m = \frac{k_r + k_{cat}}{k_f} \tag{1.14}$$

Since the value of interest is the rate of formation of the product species ($d[P]/dt$), the plot shown in Figure 1.2 can be numerically differentiated and plotted against the substrate concentration $[S]$ to yield the classic Michaelis-Menten plot of reaction velocity vs. substrate concentration. The result of this process is shown in Figure 1.3 alongside the curve predicted by the steady-state approximation of Haldane and Briggs [34].

The result of this plot is somewhat unexpected, as the numerical solution does not appear to follow the perfect inverse curve of the classic Michaelis-Menten plot. However, the reason for this becomes readily apparent: the complete divergence of the numerical and approximation plots (label 'B' on Figure 1.3) occurs because, at this point, the system is in its initial state, which can be seen to undergo rapid changes of concentration in Figure 1.2, resulting in a highly non-equilibrated state. In most real-life situations, the system equilibrates very rapidly and this divergence occurs too quickly to be seen in most results. Furthermore, the concentration of substrate is normally many orders of magnitude larger than the enzyme, which was not the case in this model system. The small divergence of the curves at point 'A' is thus simply a result of the model system never actually achieving steady-state due to the arbitrary values chosen for this sample in order to clearly demonstrate the model kinetics. It should be noted that, despite the fact that the system chosen is generally very far from being at equilibrium, the numerical and approximation curves are, in fact, very similar, demonstrating the accuracy of the steady-state approximation in most cases.

The Michaelis-Menten approximation was theorized to be an excellent model for the glucose oxidase-glucose reaction that forms the basis of the e-Mosquito sensor project. It was thus used to characterize the response of the glucose transducers manufactured over the course of the project. The remainder of this thesis uses current or current density instead of reaction velocity (e.g., I or i and I_{max} or i_{max} instead of v and v_{max}) as all reaction rates were measured electrochemically. Since the enzymatic reactions of interest produce a fixed number of electrons per reaction, the proportionality $I \propto v$ exists, provided that the rate-limiting step of the process is the enzyme reaction, and not a bulk transport phenomenon.

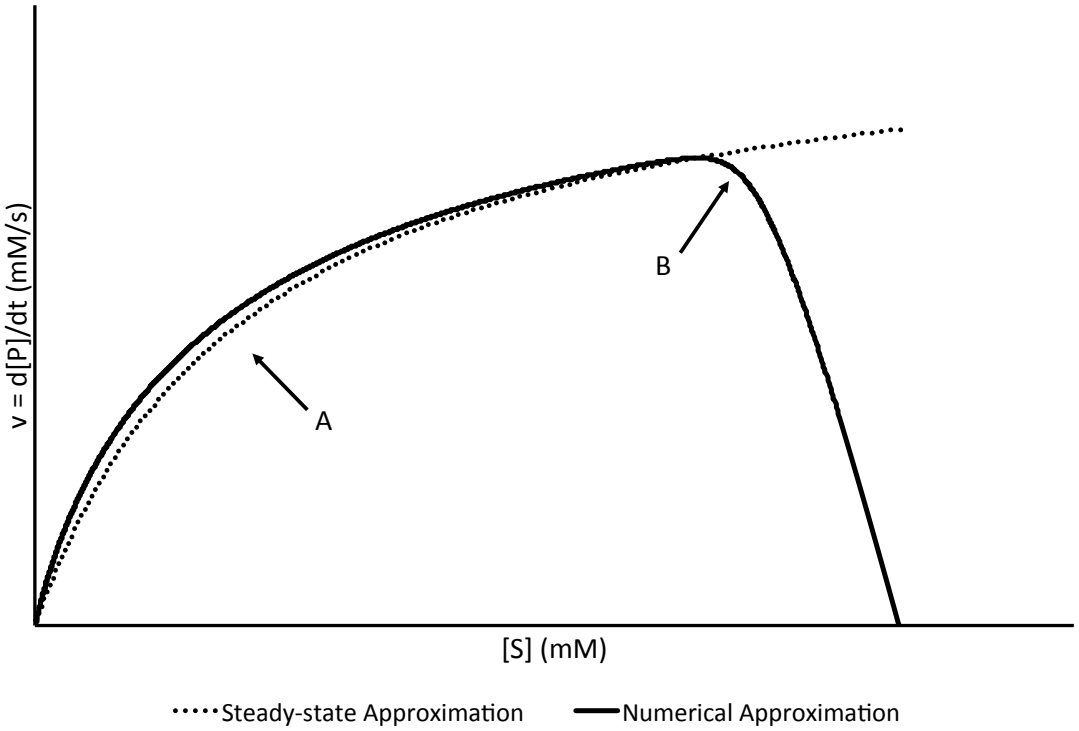

Figure 1.3: Comparison of numerically differentiated Michaelis-Menten plot with the steady-state prediction. The divergence at point 'B' occurs because of the very non-equilibrated starting conditions in the model system. The error at 'A' is a result of the very slow equilibration of this arbitrary model system, while real-life systems typically equilibrate much faster.

1.4 Glucose Sensor History

Direct blood glucose measurement originated in 1962, with Leland Clark's and Champ Lyons' article detailing various blood-based sensing modalities, including a Glucose Oxidase (GOx)-based enzymatic biosensor [35]. This original system operated by detecting oxygen consumption by GOx according to Reaction 1.15. Application of a negative potential to the working electrode allowed detection of oxygen as hydrogen peroxide (H_2O_2), according to Reaction 1.16. The patent for this electrode system was transferred to Yellow Spring Instrument (YSI)

and the first commercial device was produced in 1975 [36].

$$\text{glucose} + \frac{1}{2}O_2 \xrightarrow{GOx} \text{gluconic acid} + H_2O_2 \tag{1.15}$$

$$O_2 + 4H^+ + 4e^- \rightarrow 2H_2O_2 \tag{1.16}$$

GOx is an enzyme found primarily in the fungus *Aspergillus niger*, where it appears to be used to produce hydrogen peroxide to repel invading bacteria. It weighs approximately 150 – 180 kDa and has a complex structure, as shown in Figure 1.4. GOx oxidizes glucose, forming gluconolactone, while reducing oxygen to produce hydrogen peroxide. This results in the transfer of 2 electrons per glucose molecule [37].

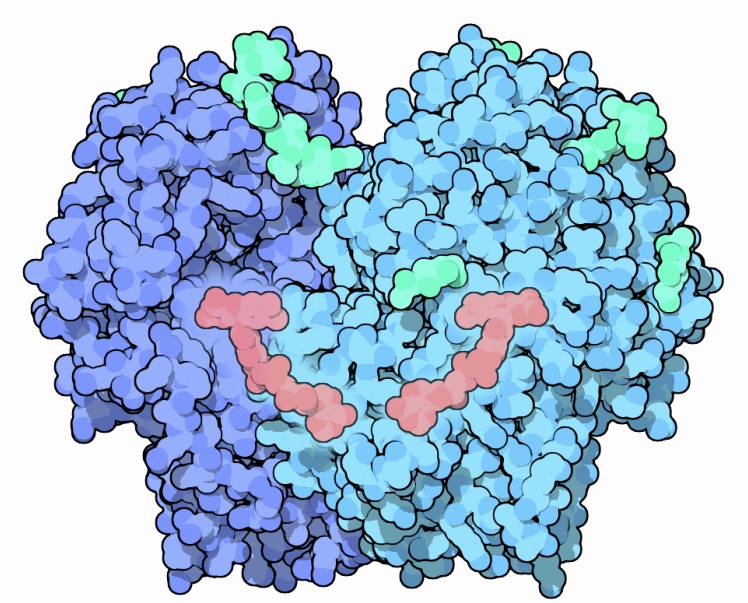

Figure 1.4: 3D structure of glucose oxidase enzyme from *Aspergillus niger* [38].

The first generation of commercially available glucose sensors relied on a similar mechanism, but instead of detecting oxygen consumption they detected the hydrogen peroxide that was produced by GOx. This mechanism both couples the GOx to the surface, and

regenerates the flavin cofactor of GOx (FAD) by reoxidizing it, allowing the GOx molecule to catalyze another reaction (Reaction 1.17) [39, 36].

$$\begin{aligned} GOx(FAD) + \text{glucose} &\rightarrow GOx(FADH_2) + \text{gluconic acid} \\ GOx(FADH_2) + O_2 &\rightarrow GOx(FAD) + H_2O_2 \end{aligned} \tag{1.17}$$

This design also introduced the concept of a 'mediator' for these systems. Figure 1.5 demonstrates the meaning of this graphically. Conceptually, a mediator serves to accept the electrons that are liberated from glucose during oxidation (and becomes reduced), and to transport them to the electrode. At the electrode, the mediator releases its electrons (becomes re-oxidized), which are detected in the external sensing circuit. The reduction of the mediator also allows the GOx enzyme (and its FAD cofactor) to return to its base oxidized state, ready to accept electrons from another glucose molecule.

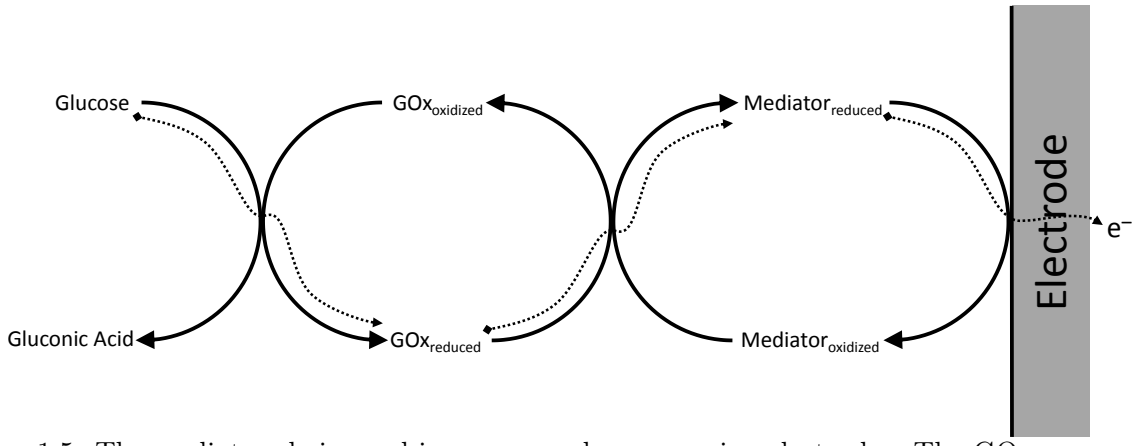

Figure 1.5: The mediator chain used in common glucose-sensing electrodes. The GOx enzyme and mediator are alternately reduced and oxidized, with the net effect of transporting negative charge from the glucose molecule to the electrode. The dotted line shows the 'path' of the electrons from the glucose molecule to the electrode via the enzyme and the mediator.

One issue faced by glucose biosensors is that blood is a very non-homogenous fluid, and thousands of other chemical species co-exist in it in varying concentrations [40]. There are

several chemical species, such as ascorbic acid, uric acid, and acetaminophen that are also known to be electroactive in the range of electrical potentials used in glucose sensors [36]. Without corrective measures, the activity of these chemicals at the surface of the electrode could result in interference and a resultant loss of accuracy. The most common approach to correcting this is to use polymer thin-film layers that are size- or charge- selective, such as polypyrrole, polyphenol, and Nafion® [41, 3]. These strategies have been quite successful and are used in most glucose biosensors today. Irhayem showed that the use of Nafion® as a top-coating in the Birss biosensor effectively eliminated interference from uric acid, ascorbic acid, and acetaminophen [42].

The other issue that glucose sensors contend with is the so-called 'oxygen deficit' in blood. Early glucose biosensors required oxygen in the blood to participate in the glucose oxidation reaction. The amount of oxygen in blood can not only fluctuate and hence change the enzyme kinetics, but also tends to be approximately one order-of-magnitude lower than the physiologic concentration range of glucose in blood. As seen from Reaction 1.15, the molar ratio of glucose to O_2 required for the reaction is 2:1. This leads to the concentration of oxygen acting as the rate-limiting quantity for the transducer reaction [36, 43].

Second-generation glucose biosensors were developed in order to avoid the dependence on oxygen, largely by using synthetic, non-oxygen-based mediators. The most commonly used of these are ferrocene and its related compounds, such as ferricyanide; these are non-biocompatible materials and hence care must be taken not to introduce them into patients. Nevertheless, their use permits significant reduction in the loss of accuracy caused by varying oxygen concentration in the blood [44, 45].

Further attempts have been made to eliminate the diffusion step in mediator-based glucose sensors. Direct 'wiring' of the GOx active site to the electrode using long-chained, conducting polymers has been successfully attempted [36]. In one example, single-walled carbon nanotubes (SWCNT) were used to connect to the FAD active site of the GOx enzyme. When the FAD cofactor was covalently bonded to the SWCNT and then the GOx

reconsituted around it, electron transfer was achieved with a rate constant of $9\,e^{-}/s$ [46].

This led to the development of 'third generation' glucose biosensors that require no mediator and instead have some form of direct electrical connection to the electrode. This promises to both avoid reactions that are limited by bulk transport (which limit the magnitude of the electrical current produced), and reduce interference from other chemical species. This term also incorporates certain novel continuous glucose sensing technologies, such as reverse iontophoresis and microdialysis sensing [36].

Reverse iontophoresis involves the application of an electrical potential to the skin in order to draw ions through the dermis and epidermis. This results in an increase in cation concentration (such as sodium and potassium) at the skin surface, which, in turn, causes an osmotic fluid shift that entrains neutral molecules, such as glucose, transporting them to the skin surface where they can be measured. This has been put to practical use in the 'GlucoWatch' device that provides 12 hours of continuous blood glucose monitoring [47]. This device still requires calibration using a finger-prick BGSM test every 12 hours, and reports exist of the GlucoWatch causing local skin irritation [47, 36, 48].

Continuous glucose monitoring is commercially available in the form of microdialysis catheter monitors integrated with insulin pumps. The microdialysis portion of the name refers primarily to the method of sample collection rather than the structure of the transducer (which is still based on GOx). A microdialysis catheter is a thin tube made of a semi-permeable membrane through which a dialysate fluid that is isotonic with the patient's extracellular fluid environment is circulated. Molecules are then able to diffuse across the dialysis membrane (if they are not larger than the membrane pore size) in proportion to their concentration in the extracellular compartment. The dialysate fluid is circulated through the catheter, which both prevents equalization of the diffusion gradient, and allows the glucose concentration in the dialysate to be measured [49, 36]. By calibrating this measurement using a finger-prick BGSM, continuous glucose monitoring can be attained. While this method provides readily available and practical continuous blood glucose monitoring, the catheters

must be replaced periodically (an invasive process), are at increased risk of infection as they remain *in situ*, and still require frequent calibration with a finger-prick glucose check [50].

Optical glucose sensing is another approach to glucose detection that takes advantage of changes in the optical properties of solutions containing glucose as the concentration changes. This is a selection of the literature concerning optical glucose detection, in order to give an overview of the field. These techniques date back as far as 1969, when the Beer-Lambert law relating the optical transmissivity of a solution to the concentration (Equation 1.18; T is the transmissivity, I is the intensity of the transmitted light, I_0 is the intensity of the incident light, ℓ is the path length of the light, ϵ is the extinction coefficient of the solute, and c is the molar concentration of the solute) was applied to glucose sensing by Trinder [51]. This system was fairly complex, using o-tolidine and o-dianisidine as chromogens: chemicals that become coloured in the presence of peroxide and a peroxidase. This system was intended for use as a bench-top lab analyzer rather than for portable, personal use.

$$T = \frac{I}{I_0} = e^{-\epsilon \cdot \ell \cdot c} \tag{1.18}$$

Another approach used the intrinsic fluorescence of GOx in order to measure glucose concentrations [52, 53]. It was discovered that GOx would fluoresce while converting glucose into gluconolactone if it was excited by 450 nm energy photons. This allowed computation of the glucose concentration by measuring the emitted photons conducted through a glass fiber-optic strand that coupled the transducer surface to the sensor apparatus. This approach was further refined by de Marcos et al. in 1999, where GOx was coupled with fluorescein to provide a higher-wavelength fluorescence response, and was immobilized in a sol-gel matrix for use as a portable, disposable glucose biosensor [54, 55]. This work found that the time between sample addition and detection of an increase in fluorescence was proportional to the concentration of glucose, with an inter-transducer variability of only 6 %. Another fluorescence approach was undertaken by Choi et al., where an oxygen-sensitive optode membrane

was used [56, 55]. This membrane would have its fluorescence quenched in the presence of oxygen, which was consumed by the GOx in its oxidation of glucose. The resulting change in the membrane fluorescence was measured and used to calculate the glucose concentration. This once again required a flowing (and invasively obtained) blood sample to measure the glucose concentration.

One more recent development in optical glucose sensing has been the use of semiconducting quantum dots [57]. Quantum dots are semiconducting nanocrystals that exhibit very high fluorescent yields, making them ideal for microsensing applications. Gill et al. used CdSe/ZnS dots specifically, which were shown to be quenched by the presence of H_2O_2. As shown earlier, peroxide is produced by GOx in the presence of glucose and oxygen, and hence this system provides another method for measuring glucose concentration in a biological fluid sample. Finally, some non-invasive approaches have been described in the literature, such as that of Heinemann et al. [58]. Their approach used measurements of the scattered light from a patient's dermis, and subsequent photospectroscopy to look for absorption patterns specific to glucose. The glucose concentration then correlated with the intensity of the spectra. This approach appeared promising but still required calibration by traditional finger-prick testing, and it proved difficult to be highly selective for glucose in such a complex solution as *in-vivo* blood [58].

1.4.1 Patch- and Microneedle-based Monitoring Devices

Wearable patches and sampling systems using microneedles are currently not in commercial production, and hence are found largely in the form of patents and patent applications. This is hardly a new trend, as blood glucose monitoring devices have been an active area of patenting since their introduction in the 1970s.

Microneedle blood sampling is an active area of research with numerous patents issued in the last ten years. Many relate to the use of matrices of fixed microneedles to harvest macroscopic blood samples from a patient. Yue et al. proposed an array of microneedles

of controllable manufacturing depth on a metal substrate. Unfortunately, while the depth of the microneedles was controllable at fabrication, the depth of penetration could not be controlled at the time of use. Furthermore, their system was optimized towards drug delivery rather than hematological sampling [59]. Several other patents have also been issued that propose similar fixed-microneedle arrays, such as Stiene et al. [60], Kravitz et al. [61], and Black et al. (patent application) [62]. These designs all involve slight differences in the method of manufacture and in the presence of analyte microchannels, but do not significantly differ from each other in the context of a complete, integrated patch system, such as the e-Mosquito. All of these patents consist of an array of microneedles that are actuated in tandem without feedback control, resulting in indiscriminate depth of penetration, and only a single measurement per array.

Prausnitz et al. detailed a similar array-based microneedle device specifically designed to sample bodily fluids and to direct these fluids to a sensing chamber [63]. However, the needles on this device were again designed to penetrate to a fixed depth and were not individually actuated. Each device is used once and then discarded, and cannot be used for multiple measurements over a period of time. Conversely, this patent provides details of various manufacturing methods to construct different sizes and morphologies of microneedles, which may prove important to miniaturization of the e-Mosquito.

Some biofluid-sampling designs, employing individually-actuatable microneedles with integrated thin-film sensing elements, have been proposed that can measure analytes in either blood or interstitial fluid [64]. Currently at the patent application stage, this design uses a restoring force to withdraw the needle, which is provided by a separate spring element, and provides *in situ* sensing when the microneedle is immersed in the fluid of interest *in vivo*. While this is acceptable for some applications, *in situ* sensors are unable to perform total-consumption electrochemical measurements, and are more prone to fouling with constituents of the moving fluid. Furthermore, the depth of penetration of these microneedles cannot be controlled based on required depth for sample retrieval, resulting in an overly-invasive device.

Full patch-based systems with arrays of individually addressable microneedles are few and far between. However, Aceti et al. have designed a patch with individually-actuated microneedles arranged in a circular pattern and connected to individual microfluidic channels, which, in turn, communicate with a single reusable sensor and sensing chamber [65]. This design is in many ways similar to the e-Mosquito – and specifically mentions glucose as an analyte of interest. It is also designed to take a periodic series of measurements from a patient at a higher temporal resolution than is currently possible with conventional glucose monitors. Interesting, there is a passing mention of using feedback control to adjust the needle penetration depth, although this idea is not expanded or elucidated upon in much detail. The single sensor element and chamber is somewhat troubling, however, as it raises issues with subsequent measurements being subject to uncertainty due to residual analyte from previous measurements remaining in the chamber.

None of the patents presented here were focused on the complete design and functionality of an integrated, minimally invasive and pseudo-continuous blood glucose analysis patch. While the patent by Aceti et al. [65] does include many elements of the e-Mosquito design, such as multiple sampling cells and controlled needle descent, it uses a single sensor and sample chamber. The combination of individual needle actuation with depth control, single-user microsensors, pseudo-continuous monitoring, and wireless control stills represent a worthwhile goal.

1.4.2 Clarke Error Grid

The Clarke Error Grid (Figure 1.6) was originally formulated in 1987, and is still considered the gold standard for glucose biosensor error characterization [66]. This grid shows a plot of the true glucose concentration against the glucose concentration that would be reported by the sensor in question. The areas of the grid (A-E) are based around clinical safety, i.e., what areas on the graph would cause errors resulting in no treatment or benign treatment, vs. which areas would result in incorrect or harmful treatment.

It is important to note that the disease process of diabetes mellitus cannot be diagnosed by a random glucose level, as a person with normal insulin dynamics can have short-term high levels, e.g. in the immediate post-prandial period. As a result, it is difficult to firmly delineate hypoglycemia, normoglycemia, and hyperglycemia, as the period of time at a particular level matters. Furthermore, the levels vary on a person-to-person basis. Normoglycemia is considered to be approximately 3.8 mM to 5.5 mM [67]. Levels significantly lower than this, especially in the presence of symptoms, is considered hypoglycemia, and should be remedied by increased carbohydrate intake. Levels significantly higher are considered hyperglycemia, though this is not normally life threatening until levels become extremely high (this cutoff varies patient-to-patient), and are often treated with insulin.

The Clarke Error Grid is subdivided into 5 areas, labeled A-E. Region A encompasses the sensors that give a result within 20 % of the true glucose concentration – the so-called 'clinically-accurate' range. Region B includes those sensors that are less than 20 % accurate, but which would not result in inappropriate therapy. Region C would result in over-correction of otherwise normal glucose levels. Region D includes sensors that would result in a failure to recognize and treat clinically-significant hyper-/hypo-glycemia. Finally, Region E represents those sensors that would actually confuse hyper- and hypo-glycemia. The goal for this project was to stay within a 25 % error band.

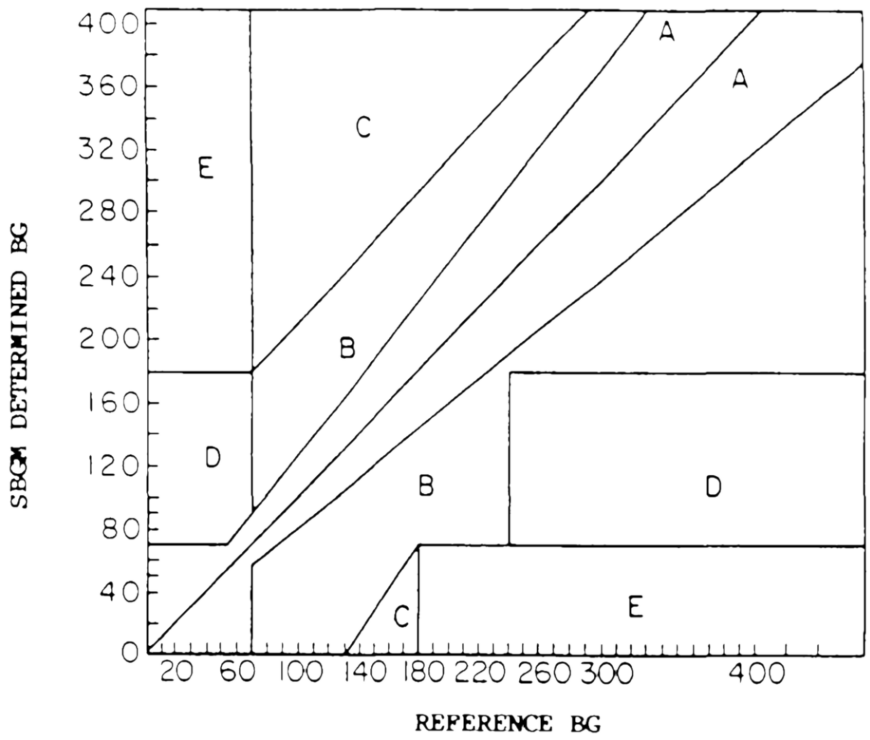

Figure 1.6: The original Clarke Error Grid, plotting the reference blood glucose on the x-axis vs. the glucose concentration reported by the sensor under investigation on the y-axis. Region A: within 20 % of the true glucose concentration. Region B: Greater than 20 % error but not sufficient to cause inappropriate treatment. Region C: measurements that would result in over correction of otherwise normal glucose levels. Region D: measurements that would fail to recognize clinically significant hyper or hypoglycemia. Region E: measurements that would confuse hyperglycemia with hypoglycemia or vice-versa [66].

1.5 The Iridium Oxide-based Glucose Biosensor

One novel approach to direct electron transfer for glucose sensors is to use iridium oxide nanoparticles (IrOx NPs). Iridium oxide is well-suited to this use as it is biocompatible [68, 69, 1], and is an excellent electronic conductor [70]. Work has been ongoing at the University of Calgary on a glucose biosensor using this material in nanoparticle form in order to directly connect GOx to a gold electrode, with the goal of creating a biosensor with fast kinetics and high current densities. This work is being undertaken by the Birss group and was selected for integration with the e-Mosquito device as its template biosensor.

High current densities are especially beneficial as the sensor then has an increased ability to be miniaturized, while still retaining sufficient current output and signal to noise ratio (Equation 1.19, where J_{out} is the output current of the sensor, i is the current density, and A is the surface area of the sensor). As the surface area decreases, so does the output current signal. However, increasing the current density produced by the sensor chemistry helps to offset this.

$$I_{out} = j \cdot A \tag{1.19}$$

The Birss sensor represents a novel approach to mediator-less glucose biosensors, utilizing IrOx nanoparticles to directly couple GOx to the electrode [2]. This is accomplished by deposition of a mixture of an iridium (Ir) nanoparticle sol and GOx molecules in suspension on a sputtered gold electrode, followed by drying and application of a Nafion® film. The Ir is then electrochemically oxidized to iridium oxide (IrOx). IrOx is a water insoluble, biocompatible material [68, 69, 1] that is electrically conductive [70]. In addition, work in the lab has shown that the surface-area of the Ir NPs increases when they are oxidized, providing more area for GOx to contact the IrOx mediator. Further details of transducer construction and testing are given in Chapters 2 and 3. This sensor configuration was shown to have an excellent Michaelis-Menten response to glucose substrate, and to exhibit current densities in the range of 1-4 $\mathrm{mA/cm^2}$ for glucose concentrations ranging from 0-20 mM [71].

The preceding sections have mentioned that oxygen-dependence is a key challenge in glucose sensor design. This is a core issue surrounding the Birss sensor, as oxygen-independence is a favourable trait (as discussed earlier in Section 1.4, due to the 'oxygen gap'). The potentials used for this sensor allow hydrogen peroxide to be oxidized, and hence for the oxygen pathway of GOx regeneration to proceed [72, 73]. Jhas et al. were able to demonstrate that the transducer could operate in both the oxygen-regenerating and IrOx-regenerating modes, depending on the mass ratio of GOx to Ir in the thin-film transducing element [2]. This

sensor has also been shown to be capable of relatively low values of the Michaelis-Menten constant, K_m, allowing it to reliably detect very low glucose levels in the hypoglycemic region, which is uncommon in current glucose sensors [71].

1.6 Enter the Electronic Mosquito

1.6.1 Limitations of Current Glucose Monitoring

Unfortunately, the current methods of blood-glucose self monitoring (BGSM) are invasive (require an uncomfortable needle poke) and have poor temporal resolution (3-4 glucose measurements per day). Significant issues with patient adherence to monitoring regimes have been identified, largely attributable to the discomfort of the process, the inconvenience associated with carrying supplies and performing the check multiple times per day, and the cost of testing supplies [74]. It has been shown that improved adherence to monitoring generally results in better glycemic control amongst those patients with pharmacologically-treated diabetes [75, 76]. Both the DCCT and UKPDS trials have shown that improved glycemic control is associated with decreased risk of diabetic microvascular complications, and in some cases, decreased risk of macrovascular complications and death [24, 23, 77]. While there are currently no trials directly assessing such outcomes in relation to routine BGSM, it is reasonable to assume that such a relationship exists.

Current methods of self-monitoring also suffer from reduced temporal resolution, i.e., a mismatch exists between the frequency of monitoring and the bandwidth of physiological glucose levels in the body. This is a sub-optimal sensing strategy that leads to aliasing of the true signal. The Shannon sampling theorem states that the sampling rate for discretization of a continuous signal should be at least twice the maximal frequency component of the signal [78]. This sample rate (f_s) is called the Nyquist rate (Equation 1.20) [79]. Figure 1.7 shows representative data from both a diabetic and a non-diabetic patient that was oversampled with a period of 5 minutes. From these data, an estimation of the Nyquist rate for these

patients was calculated and found to be 9 minutes for the diabetic patient and 7 minutes for the non-diabetic patient [80]. While some variability is expected person-to-person, it is clear that the sampling period required is significantly shorter than the current recommendation from the Canadian Diabetes Association of 6 hours [26].

$$f_s = 2 \cdot f_{max} \tag{1.20}$$

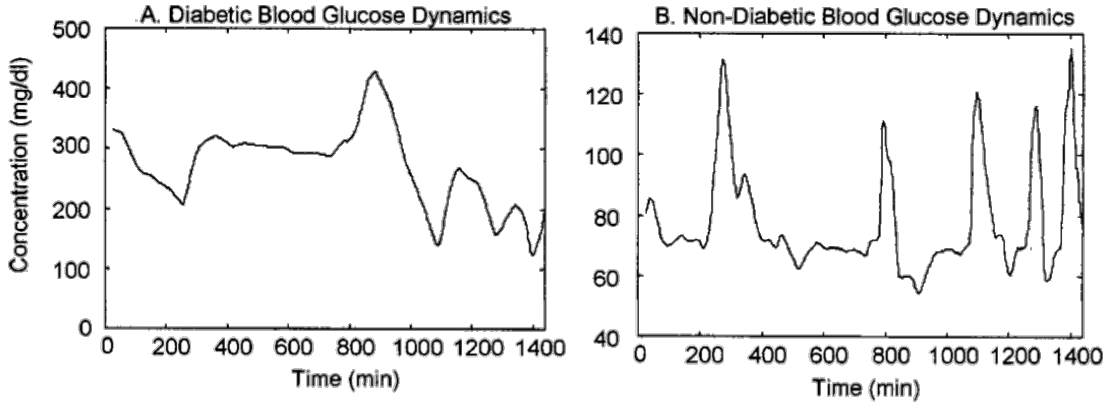

Figure 1.7: Sample glucose levels monitoring continuously over the course of a day from a diabetic subject receiving exogenous insulin once per day (a) and a non-diabetic subject (b). Sampling was performed every 5 minutes and interpolated between data points with straight lines [80].

Another complication of current monitoring regimes lies in the fact that they are predominantly a manual and not automated process (with the exception of insulin pumps with integrated glucose monitoring), and, as such, BGSM is not generally performed overnight. A common issue in insulin dependent patients is overnight hypoglycemia due to the lack of carbohydrate intake during this period of time, a potentially life-threatening complication [81]. Furthermore, unrecognized nocturnal lows can cause the development of hypoglycaemic unawareness in patients with no recognized history of hypoglycaemia [82]. Higher temporal resolution of monitoring (at the Nyquist rate) is also important to the future development of a stable feedback-controlled artificial pancreas [83].

1.6.2 Goals of the Electronic Mosquito

The Electronic Mosquito is a device concept originally developed by Martin Mintchev and Karan Kaler at the University of Calgary, and subsequently developed by Giorgio Gattiker [84] and Geoffery Thomas [85]. The proposed device is a wearable patch that contains a matrix of several tens to several hundreds of blood-sampling units, named 'cells' (Figures 1.8 and 1.9). These cells each contain a microneedle and sample collection chamber with an integrated glucose biosensor (Figure 1.10). The patch will then be worn for a period of 24 hours and glucose samples can be obtained and analyzed with a period $T = 24\ \mathrm{h} \cdot (n \times m)^{-1}$, where $n \times m$ is the total number of individual cells in the patch. Thus, a patch with 160 cells would satisfy the Nyquist period of 9 minutes. This sampling modality is not technically continuous in time, and hence has been termed 'pseudo-continuous sampling', in that no information about the original signal is lost (per the Shannon sampling theorem), but the blood is still only intermittently tested. The patch itself is single-use and applied once per day, significantly decreasing the inconvenience associated with monitoring [86].

As pain and discomfort is strongly associated with decreased compliance with BGSM [74], the e-Mosquito concept takes steps to mitigate this issue by controlling the penetration depth of the microneedle. Typical human skin has the cross-sectional structure shown in Figure 1.11. The epidermis is the strong, outermost layer, and has an average thickness of $120\,\mu$m. It contains no capillary vasculature or nerve endings. Penetration by the needle will not yield a blood sample, but will also not cause any detectable pain. The next layer is the dermis, and contains a complex array of structures, including capillaries throughout and nerve-endings in the deeper aspects of the tissue. It has a depth that ranges from $100\,\mu$m to $3000\,\mu$m [87, 88].

The goal of the e-Mosquito is to collect a blood sample from the capillaries in this layer while minimizing stimulation of the nerve-endings, and hence minimizing pain caused. This is accomplished by a controlled, step-wise descent of the microneedle into the tissue. The

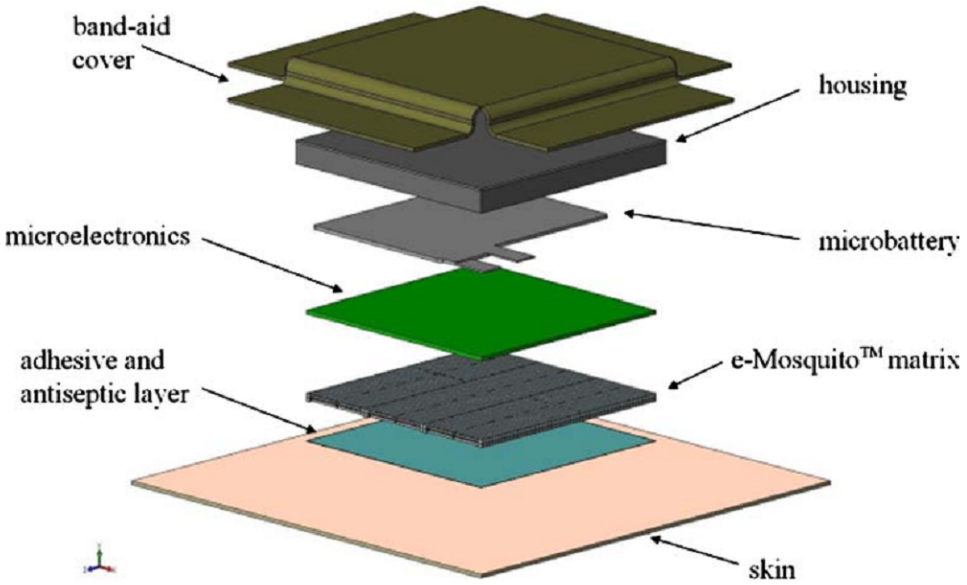

Figure 1.8: CAD drawing of the e-Mosquito patch. This graphic is an exploded view of the patch, showing the various layers contained within. The structure of the layer containing the microneedle and sensor cells, labeled 'e-Mosquito matrix', is further elucidated in Figure 1.9 [85].

sampling chamber contains electrodes that are capable of detecting blood in the sampling chamber, and a feedback control mechanism will retract the microneedle as soon as a blood sample is detected. This results in a microneedle penetration profile such as the one shown in Figure 1.12. The microneedle penetrates only far enough to extract a blood sample, and then retracts from the skin. Detailed implementation of the system was performed by Geoffery Thomas (University of Calgary) [85] and was termed 'minimally-invasive' sampling.

The end-goal application of the e-Mosquito would be as the sensing component in a com-

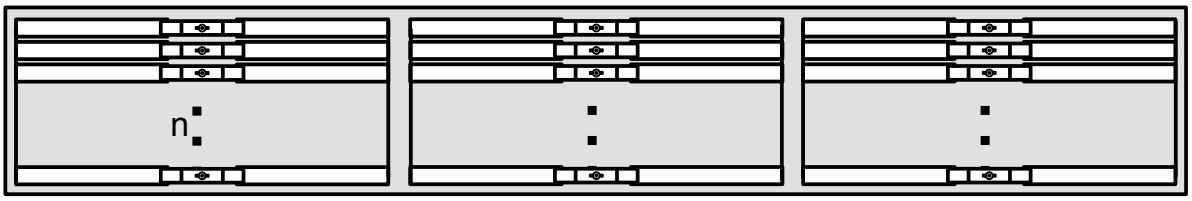

Figure 1.9: The e-Mosquito contains a matrix of individual blood-sampling 'cells' that can be addressed individually. This schematic shows a sample matrix having three columns of addressable cells and n rows. The structure of an individual cell is shown in Figure 1.10.

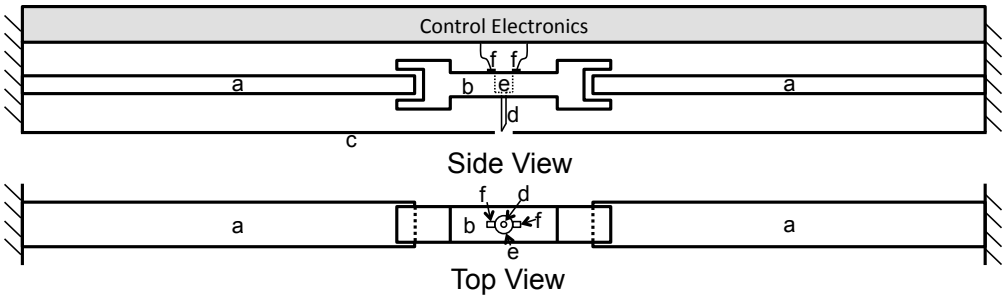

Figure 1.10: Schematic of an individual e-Mosquito cell. Piezoelectric bending cantilevers (a) actuate the sampling platform (b) downwards into the patient's skin (c). The microneedle (d) then penetrates to an appropriate depth to retrieve a blood sample in the sampling and sensing chamber (e). The entire platform is then retracted from the skin and the sample is analyzed and the result communicated to the control electronics by electrical leads (f).

plete, feedback-controlled artificial pancreas. Such a device is conceptualized in Figure 1.13, and consists of an insulin pump, a continuous or pseudo-continuous glucose monitor, and feedback control logic [83]. Note that the control loop specifically shown in Figure 1.13 represents a high-level overview only, and a real device would require a far more complex control system including integral and derivative terms, as well as appropriate patient safety safeguards. A feedback-controlled artificial pancreas device would deliver insulin, as required, to maintain glucose levels in the blood at either steady state or in accordance with a predetermined time-based profile. This is also advantageous compared to cadaveric or living-donor transplants, as there is no risk of immunologic rejection of the device. It is also trivial to add a glucagon pump to the design and have a full biphasic control loop that is able to respond to both hyper- and hypoglycaemia.

1.6.3 Current Prototype

The current e-Mosquito prototype consists of a plexiglass frame and enclosure, containing surface-mount and through-hole mounted electronic components on traditional fiberglass printed circuit boards (PCBs) (Figure 1.14). It is a large-scale prototype that is approximately the size of two decks of cards, and contains three complete sampling cells. Each cell

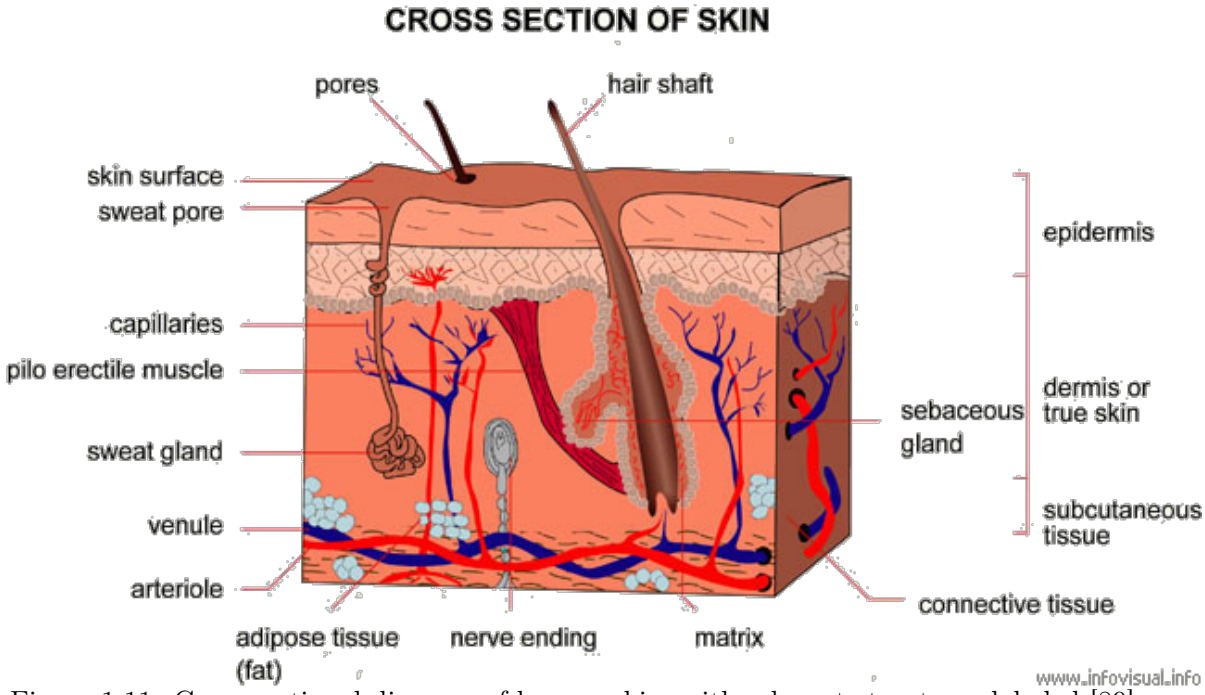

Figure 1.11: Cross-sectional diagram of human skin, with relevant structures labeled [89].

contains two piezoelectric bending actuators that undergo mechanical deflection that varies with the magnitude and polarity of the electrical potential applied. Each arm is fixed to the prototype chassis on one end, and loosely supports a sampling platform on the other. This results in the sampling platform being suspended between the two actuators, which can deflect the platform and its associated microneedle downwards into the patient's skin (Figure 1.10).

1.6.3.1 Blood Sampling Control

The closed-loop depth control for the microneedle descent and retraction has successfully been implemented in the prototype. The needle is descended into the patient's skin in small configurable-depth steps by the piezoelectric actuators, with steps on the orders of tens and hundreds of micrometers. After the needle has made a step, it will hold the resulting position for a pre-determined period of time, generally less than ten seconds, in order to allow blood to move into the sampling chamber by a combination of hydrostatic pressure and capillary

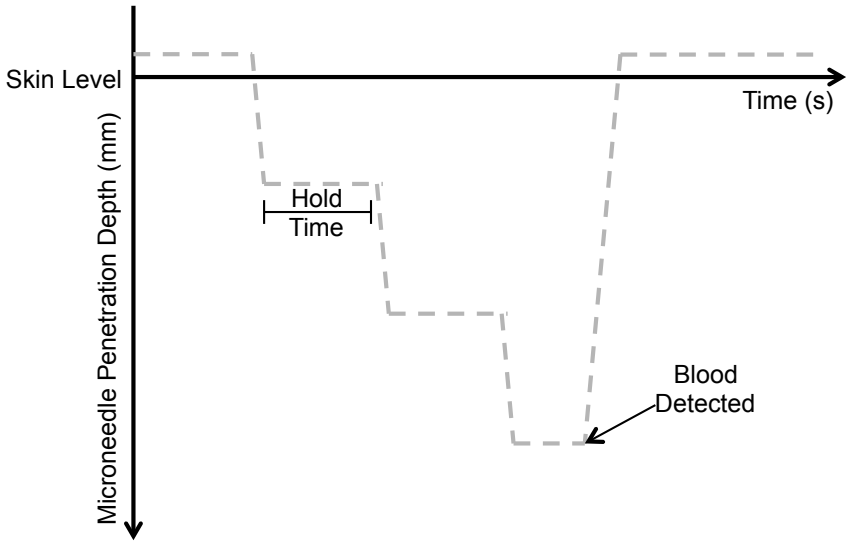

Figure 1.12: Descent profile of the feedback-controlled microneedle. The needle will be actuated downwards by a certain step depth, and then held at that level for the hold time in order to allow blood time to flow into the sampling chamber. If no blood is detected, the needle is advanced further into the skin and the process repeated. If blood is detected, the needle is immediately fully retracted.

action. This stepwise process is repeated until a 1 μL blood sample is collected, at which point the needle immediately fully retracts from the patient. A plot of the piezo-electric actuator applied voltage (representative of needle depth) and the blood-detector signal vs. time is shown in Figure 1.15. These data were collected from an actual *in vitro* test run of the prototype and demonstrates the expected functionality [85].

Successful sample collection is determined by the presence of a conducting fluid (blood) in the collecting chamber attached to the sampling needle. Geoffrey Thomas (University of Calgary) designed the detection system for the prototype, which involves two electrodes that are bridged by the blood sample (an electrically conductive solution) when the sample well is full. This signal is amplified by a simple operational amplifier in an inverting amplifier configuration, and is detected by one of the microprocessor's digital inputs [85].

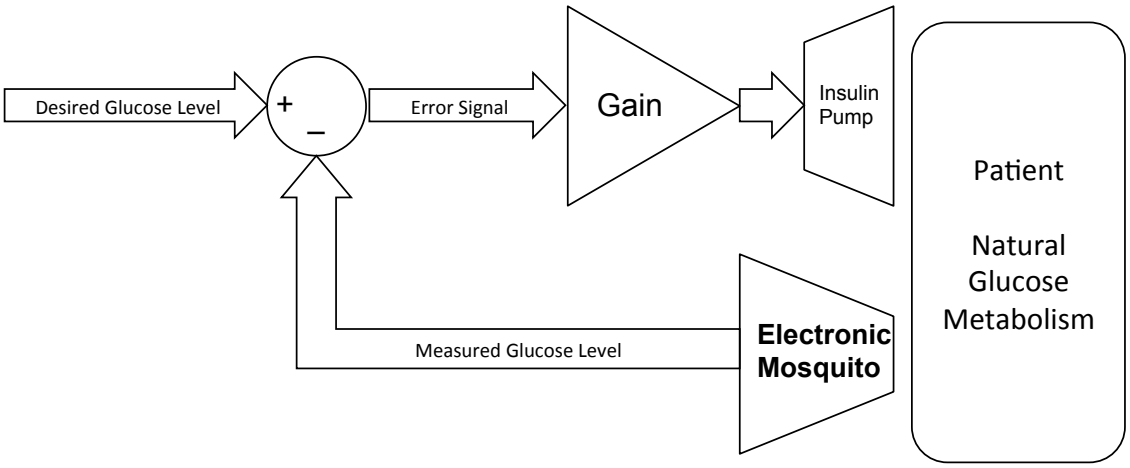

Figure 1.13: High-level overview of a closed-loop artificial pancreas. The loop provides an insulin dose that is proportional to the difference (error) between the desired blood glucose level and the measured blood glucose level. This proportionality can be a simple proportion, but is more likely to include integral and derivative terms for improved stability and performance.

1.6.3.2 Result Reporting

The e-Mosquito prototype currently implements two communication methods for device control and result reporting, direct USB tethering and wireless communication.

USB Tethering – The first and most basic method of result reporting was implemented in the original prototype by Geoffrey Thomas [85]. This method consists of a USB cable connecting the e-Mosquito to a development PC, while an integrated circuit (marketed by Future Technology Devices International – FTDI) provides a simple implementation of the USB interface protocol. The development PC then runs a custom application written in Microsoft Visual C# that uses the FTDI USB driver to control the e-Mosquito and receive data for debugging purposes. This communication modality is prototype-only and would not be useful in a consumer version of the e-Mosquito.

Wireless Control – In 2009, a wireless communication link was designed by the author that could be used directly in place of the USB communication hardware [90]. The hardware was designed around the Nordic Semiconductors IncȦNT protocol and their nRF24AP1 chip [91]. This circuit provides the same functionality as the USB link and communicates with the

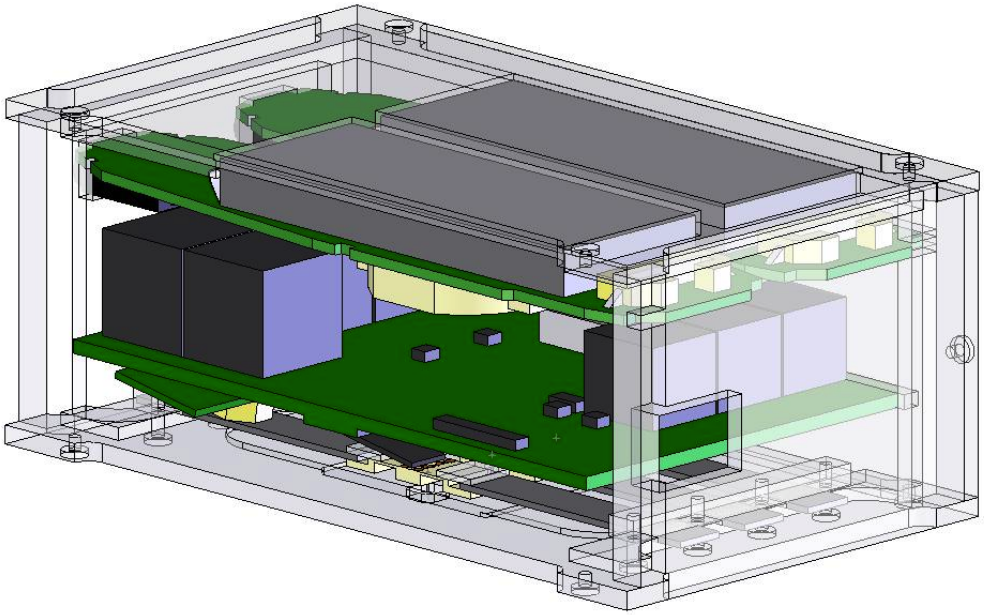

Figure 1.14: CAD rendering of the large-scale e-Mosquito prototype. The bottom PCB in green contains both the control microprocessor and the high-voltage electronics used to run the piezoelectric bending actuators. The actuators and the sampling platforms are just visible at the very bottom of the device and in the inset [85].

same control and debug program. The lack of a physical tether allows easier experimentation with the prototype device, and is easily adaptable to consumer uses, such as communicating a glucose reading to a watch or other device. A block-diagram of the various logical constituents of the communication system is found in Figure 1.16.

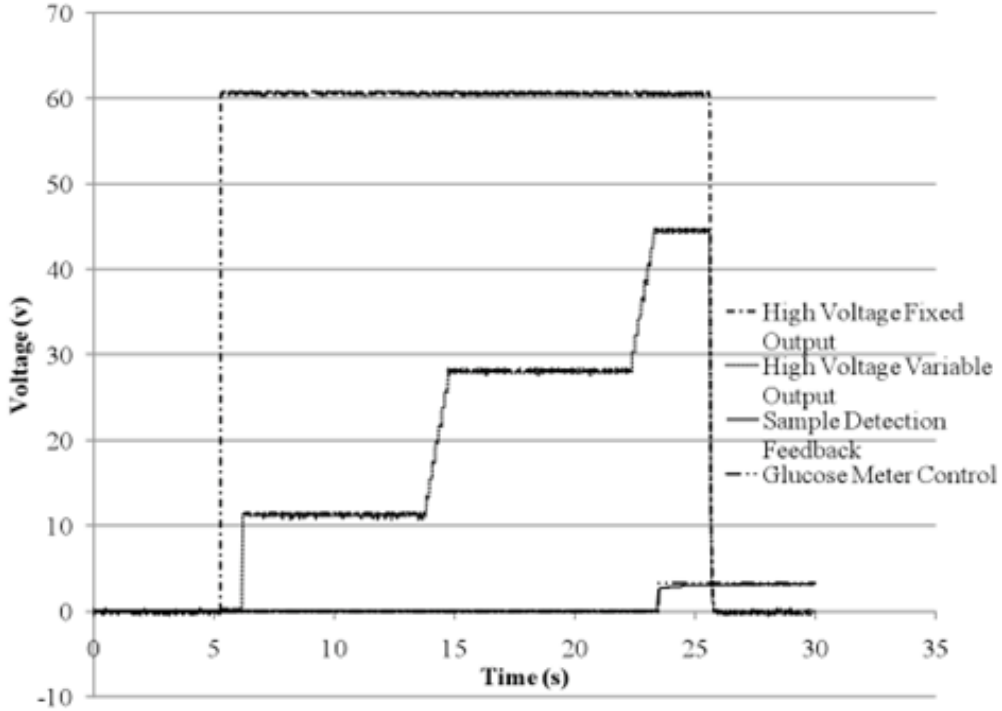

Figure 1.15: Plot of the actuator potential and the glucose-detection signal vs. time. The needle descends in small, controlled steps with an ample pause period in between. When the sample electrodes detect the presence of blood in the sample chamber, the needle and sampling platform retracts from the patient [85].

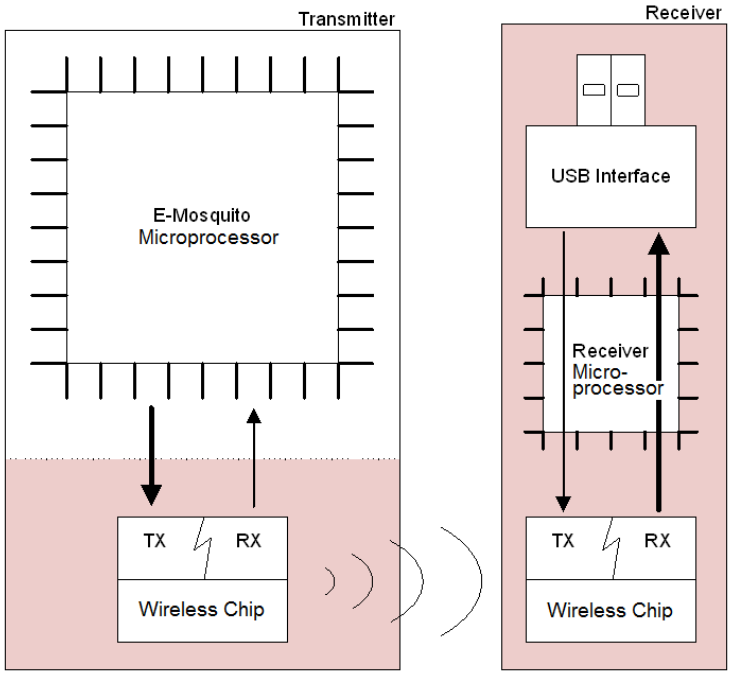

Figure 1.16: Block-diagram of the wireless control scheme. This shows both the transceiver on the e-Mosquito, and the USB-based transceiver dongle used on the PC side.

Chapter 2

Methods for Construction and Testing of Transducer Electrodes

The methods used in the fabrication and testing of transducer electrodes are detailed here. All of the methods involve combining an iridium (Ir) nanoparticle sol with glucose oxidase (GOx) and Nafion® on a sputtered gold (Au) surface. This is followed by electrochemical oxidation of the Ir metal into iridium oxide (IrOx). The GOx enzyme provides selective detection of glucose in a sample solution, while the IrOx acts to transport the liberated electrons to the Au surface and to regenerate the GOx enzyme. The Nafion® serves as a binder and a selectively-permeable membrane to reduce interference by other chemical species. This thesis tested three methods of electrode construction that differed in the order and combinations in which these components were deposited on the Au surface. This chapter describes the materials and instruments used, the methods used for construction of the electrodes, and the method for glucose testing of the constructed electrodes. Chapter 3 describes both the manner in which the results were interpreted, as well as the results themselves.

2.1 Reagents

Most stock chemicals, including ethanol (99.8% pure), iridium trichloride ($IrCl_3$), sodium ethoxide ($NaOC_2H_5$, $\geq$ 99.0 % pure), sodium phosphate monobasic (NaH_2PO_4, $\geq$ 99.0 % pure) and sodium phosphate dibasic (Na_2HPO_4 99.0 %), and D-glucose were purchased from

Sigma-Aldrich. Glucose Oxidase (G6125, Type II from *Aspergillus niger*) and Phosphate Buffered Saline tablets (#P4417) were also purchased from Sigma-Aldrich and were used as received. Nafion® was purchased as a suspension in water and isopropanol from Ion Power Inc. as LIQUION 15 wt% 950 EW. Stock concentrated sulphuric acid solution (17.8 M) and 99.5 % pure acetone were purchased from EMD Chemicals Inc. and used as received.

Distillation was used to produce high-purity distilled water (DI water). This was accomplished in-house with a Corning Mega-Pure MP-6A still, coupled with a Corning Mega-Pure D2 deionizer.

2.1.1 Ir Nanoparticle Sol

The Ir nanoparticles were formed and stored suspended in ethanol as an Ir sol using the technique developed by Irhayem et al. [42]. 0.3 g of iridium trichloride and 0.2 g of sodium ethoxide were concurrently dissolved in 10 mL of 99.8 % ethanol. The resulting solution was stirred and refluxed under argon at 75 ℃ for 2 hours in a round-bottom flask. The heat was then removed and the solution was allowed to cool to room temperature under continued Ar reflux and stirring for a further 20 hours. The cooled solution was filtered twice by vacuum filtration through fine filter paper, producing an opaque black suspension of Ir nanoparticles, with an average diameter of 2 nm [42]. The resulting filtrate was quickly sealed and stored at 4 ℃ to retard hydration of the Ir nanoparticles.

2.1.2 Glucose Oxidase Solution

A glucose oxidase (GOx) solution was prepared from lyophilized GOx powder. The powdered GOx was mixed with potassium gluconate for stability and has a listed activity of 17300 $^{\mathrm{U}}/_{\text{solid g}}$ [92] (1 U is defined as the amount of enzyme required to oxidize 1 µmol of glucose per minute).

The lyophilized powder was dissolved in DI water by gentle agitation at a ratio of 60 g of enzyme to 1 L of water. Volumes of 1 mL to 5 mL were typically prepared at one time.

The resulting solution was sealed and stored in a lab refrigerator at 4 ℃ and was used for no longer than 1 week.

2.1.3 Nafion® Solution

The Nafion® binder solution, provided by Ion Power Inc., was composed of 15.0 wt% Nafion® , 45 wt% water, and 40 wt% isopropanol. 1.0 g of this solution was diluted with 14.0 g of ethanol in order to produce 15.0 g of the final 1.0 wt% Nafion® mixture. The overall composition of the Nafion® solution was then 1.0 wt% Nafion®, 93 wt% ethanol, 3.0 wt% water, and 3.0 wt% isopropanol. Nafion® is a member of the class of synthetic polymers called an ionomers, as it is permeable to the transport of cations and water. It acts as an excellent binder to protect the transducer surface from damage, as well as to reduce interference at the electrode from other chemicals. This latter effect is accomplished as the Nafion® film is impermeable to a large number of chemical species (including anions and large organic molecules) that may otherwise become electroactive at the electrode and hence interfere with the measurement [3, 93].

2.1.4 Sulphuric Acid

The preparation of 0.5 M sulphuric acid (H_2SO_4) was accomplished by simple dilution of 17.8 M stock sulphuric acid solution. 28.1 mL of the stock sulphuric acid solution was diluted to 1.0 L with DI water.

2.1.5 Phosphate Buffer Solution

The phosphate buffer solution (PBS) was prepared by mixing 74.5 mL of 0.1 M sodium phosphate monobasic (NaH_2PO_4) with 125.5 mL of 0.1 M sodium phosphate dibasic (Na_2HPO_4) per the Henderson-Hasselbalch equation (Equation 2.1 [94]. The pH of the resulting mixture was then checked with a pH meter and adjusted to 7.0 by addition of either monobasic or dibasic sodium phosphate. Depending on the direction of correction required, either sodium

phosphate monobasic was added to lower the pH or sodium phosphate dibasic was added to raise the pH.

$$pH = pK_a + log\frac{[A^-]}{[HA]} \tag{2.1}$$

2.1.6 Phosphate Buffered Saline Solution

Human blood has a typical salinity of roughly 130 mM Na^+ [40] and PBS containing Na^+ was used to simulate this for electrode testing. This resulted in phosphate buffered saline solution (PBSS) and it was made by dissolving one Sigma-Aldrich PBSS tablet in 200 mL of DI water. This yields a solution of 10 mM phosphate buffer, 137 mM sodium chloride, and a pH of 7.40 [95]. This is a lower buffer concentration than the plain phosphate buffer, and the buffering capacity was correspondingly lower.

2.2 Working Electrode Preparation

Metallic DC sputtering deposition was accomplished using a Denton Vacuum DV-502A system configured to allow interchangeable sputtering of two metals without depressurizing the sputtering chamber. Targets were high-purity metal ($\geq 99.9\,\%$) obtained from various suppliers. Heating processes were performed using an AF Model 30 Lab Oven from Quincy Lab, Inc. Generic borosilicate glassware was used, mechanical pipets were purchased from Eppendorf, and sterile, individually wrapped 1 mL needles were obtained from the Becton, Dickinson, and Company (BD). All electrodes were single use only, and 50 electrodes were constructed and tested in total, although only 21 were used in the main experiments included here. The other 29 electrodes were used for familiarization and for feasibility studies. All electrodes in each of the three main sensor construction method groups were included (i.e., no electrodes were excluded from the results on the basis of having poor performance).

Figure C.1 (found in appendix C) shows a flowchart demonstrating the difference between the three construction methods and providing approximate build times for each technique.

2.2.1 Gold Thin Films

2.2.1.1 Sputter Deposition on Glass (Silica) Slides

Thin Au films were deposited on standard glass microscopy slides (3"x1") using sputter deposition. Slides were cleaned in a three step process to ensure no organics or other surface contaminants were present that could affect the thin film morphology or adhesion properties during sputtering. Slides were initially soaked for 10 minutes in acetone and then rinsed with DI water. Slides were then immersed in ethanol for a further ten minutes and then rinsed again with DI water. Finally, the slides were dried using a compressed air canister and were placed in the vacuum chamber of the sputter machine.

The Denton Vacuum sputterer was configured to allow sputtering of two metals consecutively without needing to break the vacuum in the sputtering chamber. The sputtering process itself occurs in a high vacuum (10 mTorr of Ar). The slides were placed on a rotating stage inside the vacuum chamber and covered by a retractable shield. The pressure in the chamber was lowered to 2 mTorr and the chamber was then flushed 3 times with Ar. After the third flush, the Ar was left on and the flow rate was adjusted to equilibrate the chamber pressure at 10 mTorr.

An initial undercoat of titanium (Ti) was sputtered by maintaining a current of 0.5 A for a period of 60 s. Without this layer, gold (Au) is unable to adhere to the glass (silica) slide. Following Ti deposition, the vacuum was maintained at 10 mTorr of Ar and Au was sputtered using a current of 0.25 A for 180 s. After the sputtering process was completed, the chamber was vented to atmospheric pressure, and the slides were removed.

The quality of film adhesion was tested using a piece of typical Scotch Tape^{TM}. The tape was adhered to the film and then removed (the "Scotch Tape Test"). Films that adhered well to the glass support did not separate from the slide.

2.2.1.2 Sputter Deposition on Poly(methyl methacrylate) (Plexiglass)

Electrodes were also formed on a Poly(methyl methacrylate) (PMMA) or Plexiglass^{TM} support platform due to ease of milling and shaping. PMMA is readily dissolved in acetone and is damaged by ethanol, so the cleaning process was altered from that used for the glass slides.

PMMA supports were 3" $\times$ 3" and were cleaned by immersion for 10 minutes in methanol to dissolve any organics from the surface of the support. After soaking, the supports were rinsed with DI water and then dried. Sputtering took place in the same manner as for the glass supports, but did not require a Ti base layer. Following sputtering with Au for 3 minutes at 0.25 A, the support was wrapped tightly in several layers of aluminum foil and baked for 10 minutes at 120 °C. The foil served to ensure an even heat distribution across the support and to prevent warping. Heating of thin gold metal films on various polymer substrates has been shown to improve the adhesion between the film and the support [96].

The PMMA-based transducers integrate blood-detection, working, and combined counter-reference electrodes on a single platform. A single homogenous film of Au thin-film is not sufficient to carry out these different functions, and hence the electrode must be patterned to provide multiple discrete electrode areas. The pattern mask used is shown in Figure 2.1. This was applied to the electrodes via subtractive photolithography, performed by the University of Calgary Department of Electrical and Computer Engineering Photolithography Lab using gold etchant GE-8148 from Transene Company, Inc.

2.2.2 Deposition of the Glucose-Active Layer

The transducing layer that responds to glucose concentration in the blood samples is referred to as the glucose-active layer and is composed of Ir oxide nanoparticles (IrOx NPs), glucose oxidase (GOx), and Nafion®. The IrOx NPs were derived from the electrochemical oxidation of Ir nanoparticles (Ir NPs, see section 2.3.2). The Ir NPs are generated as described in Section 2.1.1.

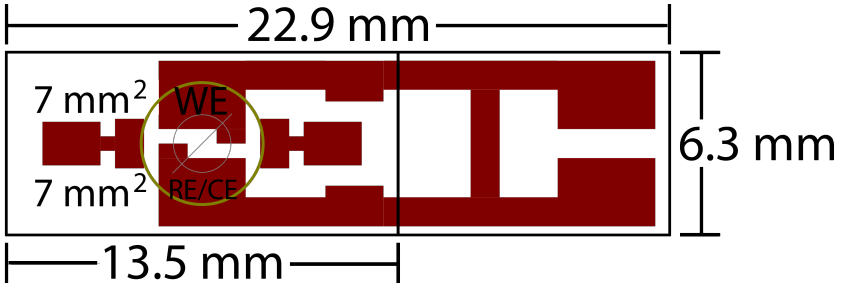

Figure 2.1: Mask pattern for PMMA/Plexiglass^{TM}-supported electrodes for use in the large-scale prototype. Red represents metallized areas, black shows the outer dimensions of the polymer support, yellow shows the predicted extent of the collected blood droplet, and gray shows the location of the hole in which the microneedle is mounted. The right-hand area (right of the black centre line) was removed after cleaning of gold and oxidation of iridium, and was included in order to allow both the working electrode and the reference electrode/counter electrode to be electrochemically prepared at the same time. The dimensions of the left-hand area are 6.3 mm × 13.5 mm and the dimensions of the complete mask (both halves) are 6.3 mm × 22.9 mm.

The glucose-active layer is located on top of the Au thin film and the support (Figure 2.2). Deposition of the active layer can be accomplished by several techniques, as described here.

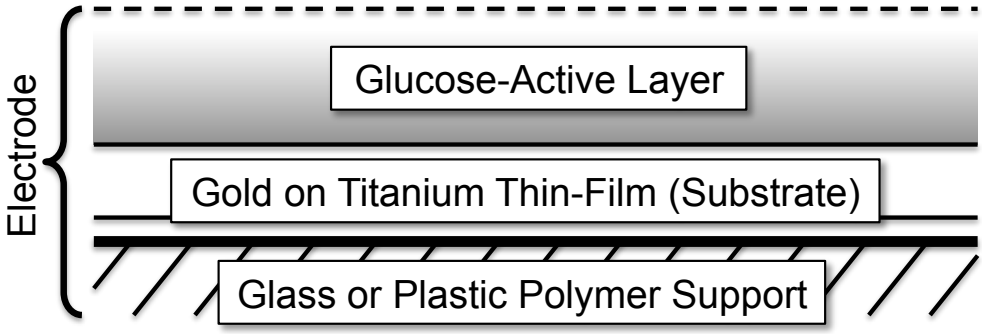

Figure 2.2: Simplified cross-sectional view of the layers forming a complete glucose electrode. The glucose-active layer can be deposited on the gold film in a variety of ways.

2.2.2.1 Electrophoretic Deposition of Glucose Oxidase

The first technique used to deposit the glucose-active layer of the transducer electrode onto the Au thin-film was the electrophoretic deposition process. Ir sol was deposited alone onto the substrate in a volume of 1 µL and allowed to dry. Given the surface area of 0.1 cm^2, the film thickness was thus expected to be approximately 100 μm while hydrated, although this would decrease over the course of the 24-hour drying process. Calculation based on the dry density of the constituents resulted in a dry film thickness of approximately 1 μm.

Ammam and Fransauer provided the method of GOx electrophoretic deposition that was used here [97]. The Ir-coated Au electrode was connected as the working electrode (WE) and immersed in a solution of GOx which was prepared as described in Section 2.1.2, but at a concentration of 10 $^{mg}/_{mL}$. A second electrode, made of platinum, was also immersed in the solution to serve as the counter electrode (CE) and an Ag/AgCl wire was used as the reference electrode (RE). An electrical potential of 4.0 V vs. Ag/AgCl was applied to the WE for a period of 30 s, followed by a potential of 0.5 V vs. Ag/AgCl for a period of 10 s. This process was repeated 6 times, and the resulting electrode was allowed to dry under ambient conditions before coating with Nafion® (2 µL) and subsequent use.

2.2.2.2 Aliquot Deposition Technique

The aliquot deposition technique involves premixing all three ingredients of the active layer (Ir NPs, GOx, and Nafion®) and then immediately placing an aliquot on the electrode surface. The aliquoting solution consisted of 4 parts Ir sol, 1 part GOx solution, and 1 part Nafion® solution. This was accomplished by mixing 8 µL of the Ir sol, 2 µL of the GOx solution, and 2 µL of the Nafion® solution.

A small amount of the resulting solution was then deposited onto the Au thin-film and allowed to dry in ambient conditions beneath a glass cover (used to shield the electrode from dust contamination). The amount of this solution pipetted was 1 µL. The tip of a mechanical pipette was used to spread the aliquot and ensure that it covered the entire desired surface

area of 0.1 cm^2. This again resulted in a wet film thickness of 100 μm and a dry film thickness of approximately 1 μm.

2.2.2.3 Sequential Aliquot Deposition Technique

The sequential aliquot deposition technique consisted of depositing a layer of Ir sol on the Au thin-film substrate, electrochemically oxidizing the Ir to IrOx, and then adding GOx and Nafion® on top. A small aliquot of Ir sol of volume 2 µL was placed on the Au and mechanically spread with a pipet tip to cover the desired geometric surface area. The Ir on the electrode was then oxidized using the procedure described in Section 2.3.2. The electrode was then gently rinsed with DI water and allowed to dry. Next, a mixture of 1:1 GOx solution:Nafion® solution was prepared, and an aliquot of this solution having a volume of 1 µL was deposited and spread on top of the IrOx layer. This ensured a ratio of 4:1:1 Ir:GOx:Nafion® by volume. The resulting layer of enzyme or enzyme and Nafion® was allowed to dry before being used. The film thickness is more difficult to estimate in this case due to the sequential deposition and drying steps. The upper range wet-film thickness by geometric calculation in this case was 300 μm, and the dry film thickness is approximately 1.5 μm.

2.3 Electrochemical Methods

All electrochemical experiments were performed in a glass cell constructed in-house (Figure 2.3). This cell was highly flexible and allowed a variety of solutions and electrodes to be used. For example, the entire regular hydrogen electrode (RHE) RE could be replaced with an IrOx RE or a combined RE/CE.

2.3.1 Electrode Cleaning

Au electrodes were cleaned by repeated three-electrode cyclic voltammetry (CV) in 0.5 M H_2SO_4 under room air until a typical (standard) Au CV was obtained (Figure 2.4). The CVs

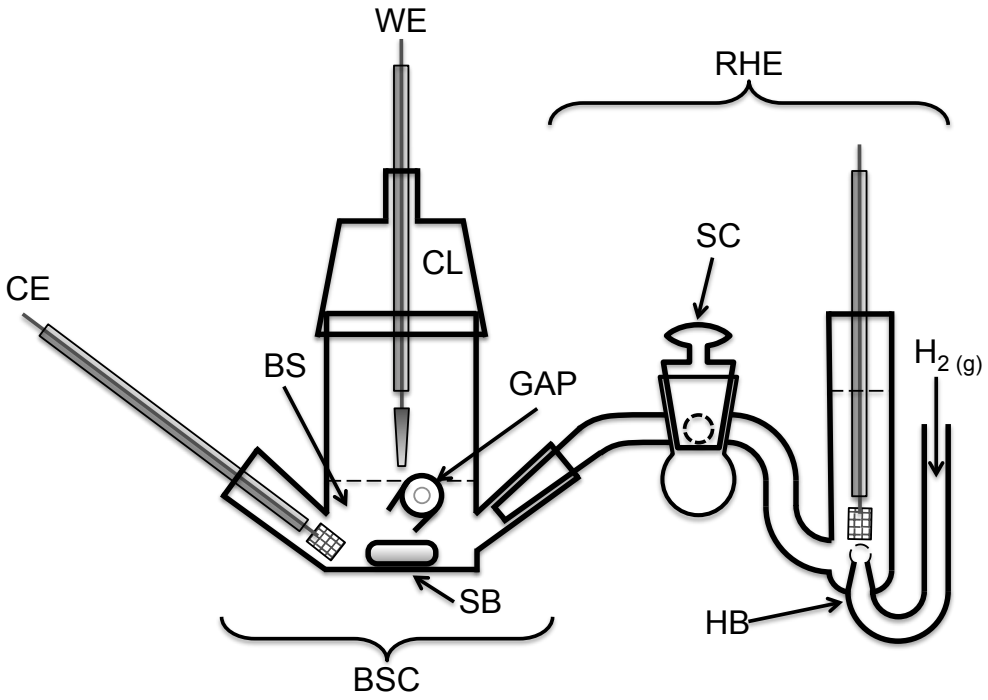

Figure 2.3: Diagrammatic view of the electrochemical cell used for the experiments in this project. BSC = Bulk Solution Cell; BS = Bulk Solution; CL = Cell Lid; WE = Working Electrode (shown with flat-nose clip); CE = Counter Electrode (platinum gauze); GAP = Glucose Addition Port; RHE = Reversible Hydrogen Electrode (the Reference Electrode); SC = Stopcock; HB = Hydrogen Bubbler; SB = Stir Bar

were performed against a reversible hydrogen electrode (RHE) reference and the potential range was from 0.0 V to 2.0 V vs. RHE at a rate of 100 $^{\mathrm{mV}}/_{\mathrm{s}}$. Sixty-five CV cycles were generally performed in order to ensure that the Au was fully cleaned, but only samples that showed a consistent and repeatable reduction peak (Figure 2.4 peak 'B') across multiple CV cycles were deemed clean and ready for use.

2.3.2 Iridium Oxidation

The Ir NPs were oxidized to Ir (III/IV) oxide by CV cycling. The CV oxidation was performed with the Ir-coated electrode immersed in 0.100 M phosphate buffer solution. The CV cycling was performed in two steps (all voltages are relative to RHE):

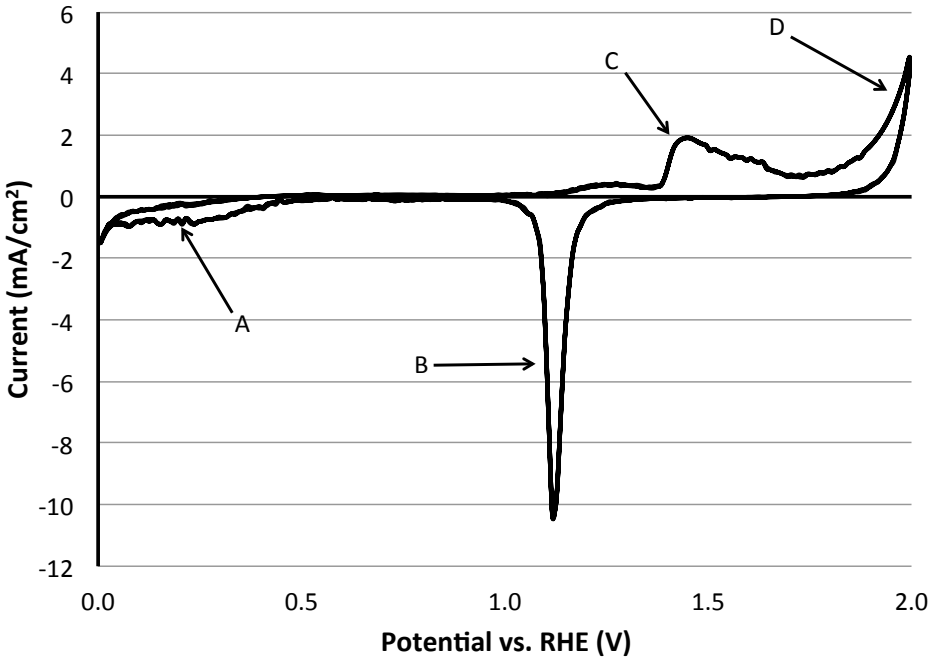

Figure 2.4: The distinctive shape of a gold CV when immersed in 0.5 M H_2SO_4. Peak 'A': Reduction of oxygen. Peak 'B': Au reduction. Peak 'C': Au oxidation. Peak 'D': Oxygen evolution.

1. 3 cycles with a range of 0.0 V to x V, where x ranged from 0.25 V up to 1.15 V in 0.01 V/set increments.
2. 65 cycles with a range of 0.0 V to 1.24 V.

These CVs were performed sequentially in an automatic manner by the potentiostat, using a consistent scan rate of 100 $^{\text{mv}}/_{\text{s}}$. The final 65-cycle program allowed the Ir to be fully oxidized. There was minimal change in the CV shape cycle-to-cycle by the end of this process, indicating that no additional IrOx is being generated. Furthermore, disappearance or reduction of the hydrogen adsorption (H_{UPD}) peak indicated that the metallic Ir had been almost entirely oxidized. The H_{UPD} peak results from underpotential adsorption of hydrogen on to metallic Ir.

2.3.3 Glucose Response Characterization

Following the preparation of the transducer electrodes, their response to varying concentrations of β-D-glucopyranose (glucose) was tested in order to characterize the transducer performance. This was done using a three-electrode cell containing either PBS or PBSS (Sections 2.1.5 and 2.1.6). The transducer was used as the WE, and in most cases, an RHE was used as the RE. Metallic platinum (Pt) was used as the CE. In some experiments (noted in the relevant sections), an IrOx electrode was used as both the RE and CE.

The cell was filled with 20 mL of either PBS or PBSS and the RHE was filled with the same solution as the cell. H_2 gas was bubbled through the RHE for at least 20 minutes prior to testing of a sample. After the transducer WE was immersed in the solution, three cycles of a 0.0 V to 1.25 V vs. RHE CV were performed in order to verify that the electrode was properly oxidized. The WE was then held potentiostatically at 1.2 V vs. RHE and allowed to equilibrate for a period of 5 minutes. Following this equilibration period, the electrode was again held at 1.2 V vs. RHE (Jhas et al., 2010 [2]) while glucose was added to the cell solution.

The concentration of glucose in the electrochemical cell was raised by 2 mM per addition (unless otherwise noted). The initial addition involved 40 µL of 1.0 M stock glucose solution to 20 mL of the cell solution. One effect of making these small additions of glucose to the cell solution was an increase in the volume of solution in the cell itself. As a result, larger volumes of 1.0 M glucose solution were added to the cell solution for subsequent additions in order to provide the same 2 mM increase in glucose concentration in the cell. The volume of 1.0 M glucose solution to be added to the electrochemical cell at each step are given in Table 2.1.

Under this protocol, 10 glucose additions span the clinically-relevant range of glucose concentrations (0-20 mM) [66]. Glucose was added to the solution using a mechanical pipet at an interval of 50 seconds, in order to allow time for the solution to equilibrate after each

Table 2.1: Volume of 1.0 M glucose solution added to the 20 mL cell solution per addition. **N.B. this is a theoretical calculation only and its accuracy exceeds the accuracy available from the syringe used to measure and deliver the glucose solution into the cell solution. These values were used as a guide while drawing up the volume of glucose solution to deliver in the physical experiment.**

Step #	**Starting volume of cell solution**	**Volume of glucose added**	**Resulting glucose concentration**
1	20.0 mL	40.0 µL	2 mM
2	20.0 mL	40.2 µL	4 mM
3	20.1 mL	40.3 µL	6 mM
4	20.1 mL	40.5 µL	8 mM
5	20.2 mL	40.6 µL	10 mM
6	20.2 mL	40.8 µL	12 mM
7	20.2 mL	41.0 µL	14 mM
8	20.3 mL	41.1 µL	16 mM
9	20.3 mL	41.3 µL	18 mM
10	20.4 mL	41.5 µL	20 mM

addition. The solution was stirred with a magnetic stirrer in order to avoid the development of a concentration gradient.

Chapter 3

Characterization of Transducer Glucose Response

Experiments to validate and characterize the transducer construction method were undertaken using the methods outlined in Chapter 2. The construction methods were tested in a sequential fashion, and included: electrophoretic deposition of glucose oxidase (GOx), combined aliquot deposition, and sequential aliquot deposition. All of these terms are explained in their respective sections. The results attained by testing of the transducer with the custom sensor electronics are deferred to Chapter 4, as this was performed using the complete integrated e-Mosquito prototype.

The transducer characterization work carried out in this section used three-electrode electrochemical techniques. This provided a high-accuracy, reproducible setup, where results could be compared with previous work done on the Birss glucose biosensor. Some two-electrode experiments were performed early on in the experimental process and showed results that were similar to those presented in the three-electrode experiments shown below. However, it was decided to continue with a three-electrode method for the above mentioned reasons, and to provide a more flexible and extendable sensor, i.e., a three-electrode potentiostat can be converted to a two-electrode potentiostat, but the inverse is not true.

3.1 Electrophoretically Deposited GOx Electrodes

The first method used to form reproducible electrodes involved cleaning of the Au, followed by aliquot deposition of the Ir sol (nanoparticles, NPs) on an electrode. The Ir NPs were then electrochemically oxidized to IrOx, followed by electrophoretic deposition of the GOx enzyme on the surface by the application of a positive electric potential to the working electrode.

3.1.1 Au Cleaning

Cleaning of the sputtered Au thin films on glass was accomplished by electrochemical cycling in 0.5 M H_2SO_4, according to the method outlined in Chapter 2. Figure 3.1 shows the final cleaning cycle of all 4 electrodes that were used for this experiment, and demonstrates the high degree of similarity between the traces. Some error is expected due to small mismatches between the measured area of the electrode immersed in solution and the actual area of the electrode in conductive contact with the solution. In addition, variability in the conductivity of the system (e.g., the film thickness, or the quality of the connection between the alligator clip on the potentiostat-side and the electrode) led to some variability in magnitude of the traces. It was felt that the variability shown here was within acceptable limits for the electrodes.

3.1.2 Ir Oxidation

Once the Ir sol was deposited on the electrode surface and allowed to dry, it was oxidized to IrOx using electrochemical cycling methods, as described in Chapter 2. Figure 3.2 shows the difference between the trace of the first CV cycle and the trace of the 65^{th} (and final) CV cycle of electrode 'B'. This demonstrates a reduction in the amount of metallic Ir present (as evidenced by the decreasing H_{UPD} peak at point 'A' – see Section 2.3.2) and an increase in oxidized Ir (the increase of the charge transferred at point 'B').

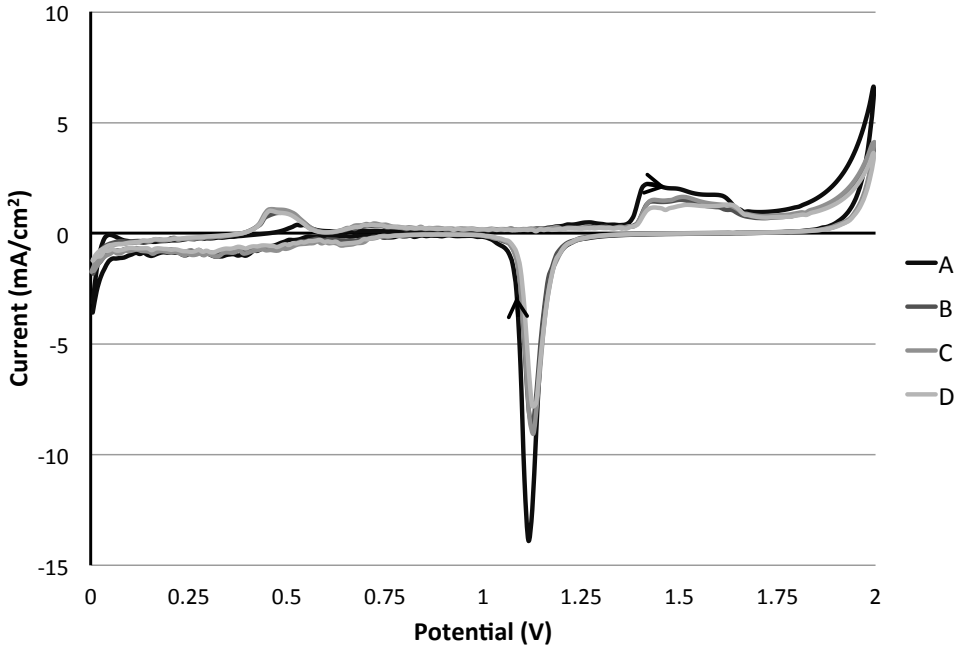

Figure 3.1: Plot of final Au cleaning CVs for the electrophoretically deposited electrodes. This experiment was performed in 0.5 M H_2SO_4 with a sweep rate of 100 mV/s. The arrows indicate the direction of the voltage sweep, and is the same for all of the CVs performed and shown in this thesis. The solution was stirred and deaerated using argon bubbled through the cell solution.

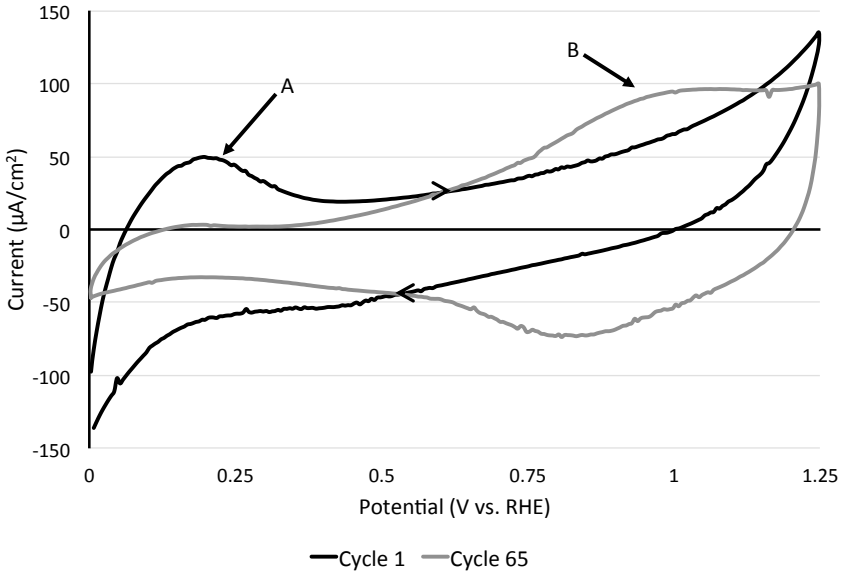

Figure 3.2: Sample CV showing the conversion of Ir to IrOx over the course of 65 CV cycles for the electrophoretically deposited electrodes. Point 'A' shows the decrease in metallic Ir available for hydrogen adsorption (H_{UPD} peak in Cycle 1), while point 'B' shows the increase in IrOx quantity. This experiment was performed in PBS under argon and the solution was stirred throughout the experiment. Sweep rate of the potential was 100 mV/s.

A superimposed plot of all of the final cycles of Ir oxidation for the electrophoretically-deposited electrodes is shown in Figure 3.3. The resulting traces are very similar in morphology but have some subtle variability in magnitude. Analysis of the correlation between the variability in this plot and the resulting variability in the Michaelis-Menten parameters is undertaken in Section 3.5.3.1.

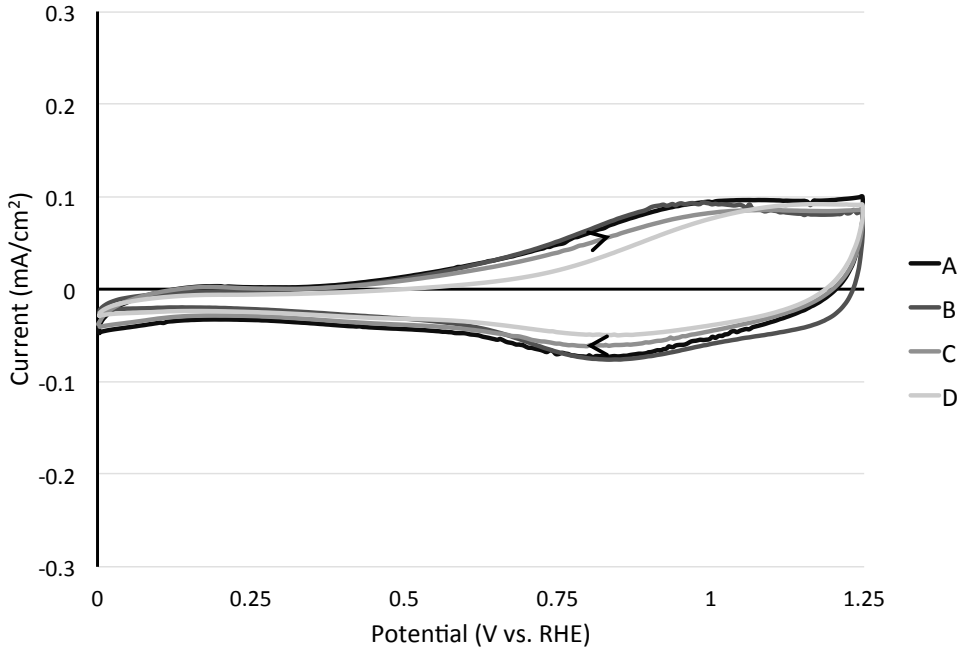

Figure 3.3: Superimposed plots of the final (65^{th}) Ir oxidation cycle for all electrophoretically deposited GOx electrodes. This was performed under argon in a stirred PBS cell solution, with an electrical potential sweep rate of 100 mV/s.

3.1.3 Electrophoretic Deposition of GOx

GOx was electrophoretically deposited on the electrodes as per the protocol laid out in Chapter 2. Following the deposition, Nafion® was deposited on top of the electrode to act as a selective-barrier and to maintain the surface integrity of the electrode. The protocol used for electrophoretic deposition is detailed in Section 2.2.2.1. During the electrophoretic deposition process, no physical changes were noted to the electrode itself, and there were no changes to the GOx solution in which it was placed for deposition. Verification of successful enzyme deposition was deferred to be confirmed by the presence of a Michaelis-Menten response to the addition of glucose to the cell solution (glucose response testing).

3.1.4 Glucose Response Testing

Glucose testing was performed according to the protocol in Chapter 2, resulting in a plot of output currents corresponding to glucose concentrations ranging from 0 mM to 18 mM. Each glucose concentration in the PBSS cell solution was maintained for a period of 50 seconds, and a 30 second window was extracted from the middle of this 50 second period. The average output current of the 30 second window was used as the measured output current for the corresponding glucose concentration (Figure 3.4a, raw data from the experiment only). The stability of the current after each glucose addition over a long period of time (at least 50 s in this experiment) indicated that the solution was well-stirred (no glucose-depleted region forms at the electrode interface as glucose is converted by GOx), and that the amount of glucose in the solution far exceeded the amount of enzyme on the surface. In addition there was noise with an amplitude of approximately 1.5 % of i_{max} in all traces, but this noise had frequencies greater than 5 Hz and hence was easily eliminated by the low-pass effect of the averaging performed on the trace.

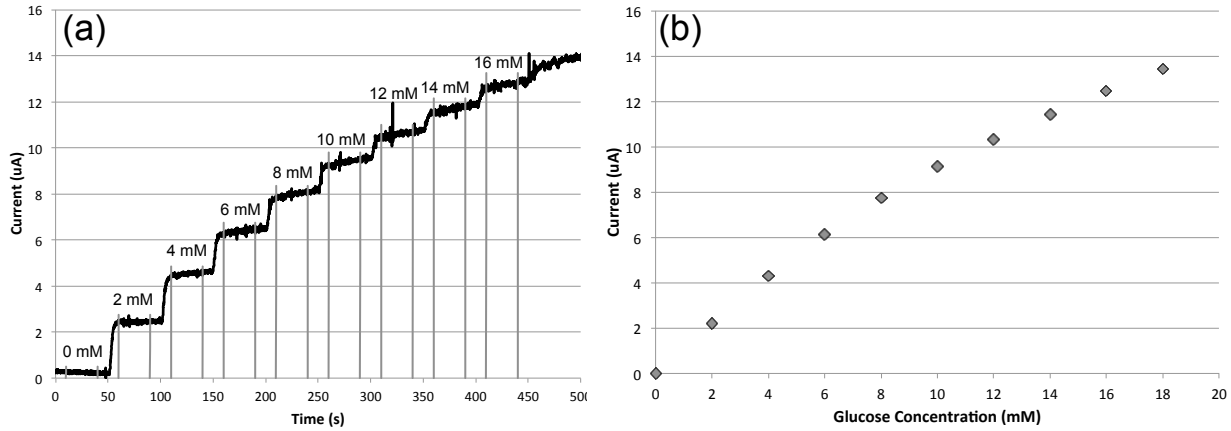

Figure 3.4: An example of the manner in which a time-based glucose addition (a) is converted to a standard Michaelis-Menten plot (b). The gray vertical lines in (a) indicate the averaging windows used to determine the single average current value for each glucose concentration, which corresponds to the plotted currents in (b). This plot shows representative sample data only, and does not show data from any transducer that was used for the research presented in this thesis.

A non-linear regression fit to the sample points for each electrode was computed with MATLAB® using the Michaelis-Menten model (Section 1.3), resulting in a set of Michaelis-Menten plots (Figure 3.5).

The variability in the glucose response between electrodes is clearly quite large and likely to exceed the 20 % clinically-acceptable percent error (Figure 3.5). This variability is quantified in Table 3.1 using the percent-error quantification method described in Section 3.5.1. These numerical results confirmed that the percent error resulting from the electrophoretic deposition of GOx method exceeded the desired maximum of 20 %, in some cases quite significantly. Furthermore, this method produced quite small output currents ($<60\,\mu A/cm^2$), which is undesirable for a miniaturized sensor.

From a practical perspective, the electrophoretic deposition of GOx for transducer construction made poor use of the stock-purchased GOx enzyme, due to the protocol being followed (Section 2.2.2.1). Approximately 20 mL of GOx solution were required to immerse the transducer being coated, and the protocol called for a solution GOx concentration of

Figure 3.5: Resulting Michaelis-Menten plots for four different electrophoretically deposited electrodes (labeled A-D). The measured data are represented by the points and the black lines show the resulting fitted Michaelis-Menten model for each electrode. This experiment was performed in a stirred PBSS solution that was not deoxygenated. The cell potential was held at 1.2 V vs. RHE. Each measurement has a maximum calculated percent error of $\pm$ 8 % on the x-axis, resulting largely from the syringes that were used to add glucose. The y-axis maximum error is $\pm$ 0.2 % and stems from the error in the potentiostat ammeter and digitizer. Despite the relatively large potential x-axis error, the closeness of fit of the Michaelis-Menten model to the measured data suggests that the percent error in practice is much smaller.

$10\,{}^{\mathrm{mg}}/_{\mathrm{mL}}$. This resulted in 200 mg of lyophilized GOx enzyme being required for each electrophoretic deposition solution. The large amount of GOx required to form a small number of sensors, along with the poor reproducibility and small output current, resulted in the decision to attempt aliquot deposition of the Ir sol and GOx, the method described in the next section.

Table 3.1: Calculated i_{max} and K_m parameters for electrophoretically deposited test electrodes from Figure 3.5. The percent error is the error in the reported glucose concentration vs. the true glucose concentration when using the batch mean values for i'_{max} and K'_m (see Section 3.5.1).

Electrode Sample #	$\boldsymbol{i_{max}}$ **(µA/cm²)**	$\boldsymbol{K_m}$ **(mM)**	**Percent Error**
A	26	28.0	-72 %
B	43	14.9	-26 %
C	33	13.0	-21 %
D	57	6.00	very large
Mean	40	15.5	-22 %
Std. Dev.	14	9.20	49 %

3.1.5 Validation of Michaelis-Menten Model

Section 3.1.4 shows the results of the glucose response testing, and the fitted Michaelis-Menten plots. However, the reaction kinetics of the full system, including the iridium oxide nanoparticles and the gold electrode, only obey Michaelis-Menten kinetics if the enzymatic reaction is the rate-limiting step of the overall reaction.

In order to determine the appropriateness of Michaelis-Menten kinetics as a model for the transducer response, the normalized root-mean-squared error (NRMSE) was calculated for a series of sample electrodes (electrodes A – J) using the non-linear regression fit residuals for each electrode (R_i), as per Equation 3.1.

N.B.: $I_{maximum}$ represents the largest electrical current measured during the electrode test, and is distinct from the Michaelis-Menten parameter, I_{max}.

$$NRMSE = \frac{\sqrt{\frac{\sum R_i^2}{i}}}{I_{maximum}} \times 100\,\% \tag{3.1}$$

The results of the model fitting process are summarized in Table 3.2. The errors of the Michaelis-Menten fit were all less than 5 %, which indicated that Michaelis-Menten enzyme kinetics were an excellent model for the behaviour of the glucose transducers studied in this project. This model was used as the *de facto* behaviour model in the remainder of this chapter. Tabulated results showing the calculated $NRMSE$ values for the other transducers

will be provided in the relevant sections.

Table 3.2: Summary of calculated NRMSEs for the electrophoretically deposited GOx electrodes.

Electrode Sample #	**Model NRMSE**
A	0.39 %
B	1.28 %
C	1.09 %
D	1.59 %
Mean	1.09 %
Std. Dev.	0.51 %

3.2 Aliquot Deposited GOx Electrodes

The second method used for glucose transducer construction involved Au surface cleaning, followed by aliquot deposition of a mixture of the Ir sol, GOx solution, and Nafion® simultaneously on the Au surface (Section 2.2.2.2), followed by 24-hours of air-drying. Aliquot deposition involved mixing the constituent chemicals together, removing a small and precisely measured volume of the resulting solution, and mechanically spreading the solution on the electrode surface before allowing it to dry. Following deposition, the Ir was again electrochemically oxidized to IrOx (described in Section 2.3.2) in order to produce the aliquoted final transducer electrode.

3.2.1 Au Cleaning

Cleaning of the sputtered Au thin-film was again accomplished by electrochemical cycling in 0.5 M H_2SO_4 according to the method outlined in Chapter 2. Figure 3.6 shows the final cleaning cycle of all 10 electrodes constructed by the aliquot deposition method, again demonstrating a high degree of similarity between the traces, similar to Figure 3.1. Sources of error for the small amount of variability observed were the same as those identified in

Section 3.1 for Au cleaning during the electrophoretic deposition experiments.

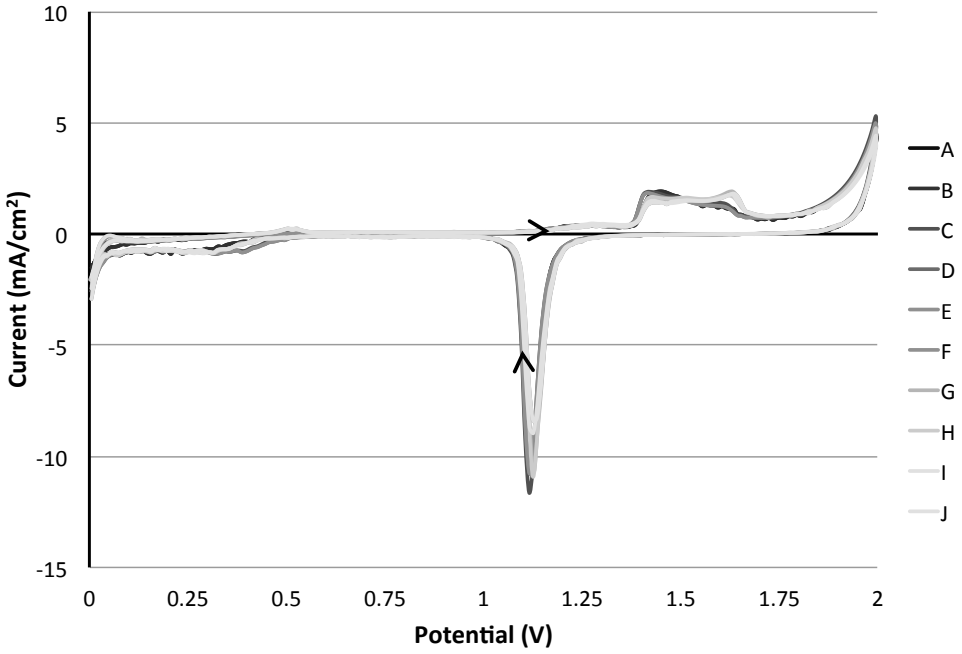

Figure 3.6: Plot of final Au CVs for the aliquot deposition electrodes. This experiment was performed in 0.5 M H_2SO_4, with stirring, and under deaerated conditions (with argon bubbled through the cell solution). The sweep rate of the electrical potential was 100 mV/s.

3.2.2 Ir sol, GOx, and Nafion® Deposition

A mixture of Ir sol, GOx, and Nafion® was prepared in a 4:1:1, ratio as described in Section 2.2.2.2. A volume of 1 µL of this solution was then deposited on the cleaned Au surface and was mechanically spread on the electrode to cover an area of 0.1 cm^2. The aliquoted solution was visible on the electrode due to the dark colour of the Ir, but the deposited droplet rapidly became heterogenous, with aggregation seen randomly across the electrode. The finished electrodes were allowed to dry for a period of 24 hours before use.

3.2.3 Ir Oxidation

Once the Ir sol, GOx, and Nafion® were deposited together on the electrode surface and allowed to dry, the Ir metal was oxidized to IrOx using potential cycling methods in the same manner as for the electrophoretically deposited electrodes (Section 3.1.2), and as described in Chapter 2. Figure 3.7 shows a plot of the first and final (65^{th}) CV cycles of an electrode, demonstrating a decrease in the amount of metallic Ir present (The magnitude of the H_{UPD} peak at point 'A' decreased, Section 2.3.2) and an increase in oxidized Ir (the magnitude of the current at point 'B' increased).

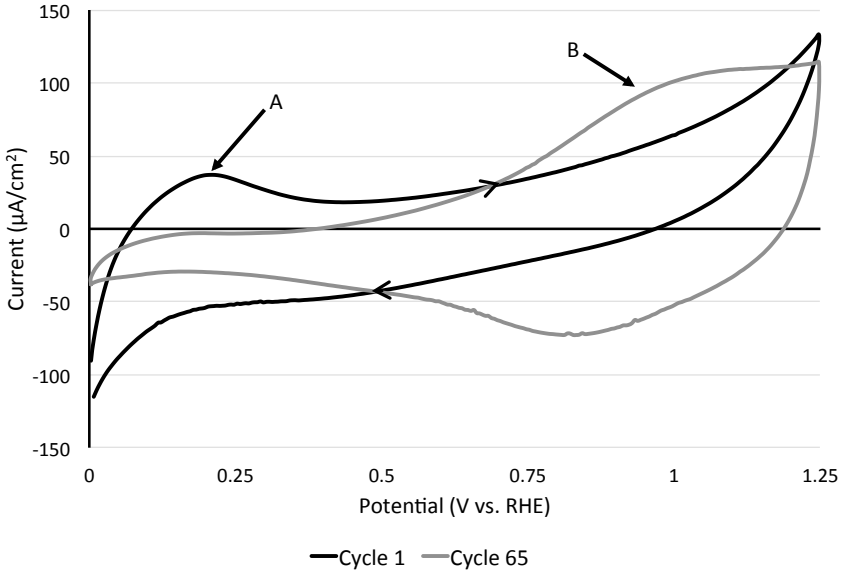

Figure 3.7: Sample CVs showing the conversion of Ir to IrOx over the course of 65 CV cycles for the aliquot deposited electrodes. Point 'A' shows the decrease in metallic Ir available for hydrogen adsorption, while point 'B' shows the increase in IrOx quantity. This experiment was performed in PBS under argon, and the cell solution was stirred throughout the experiment. The sweep rate of the potential applied to the cell was 100 mV/s.

The final CVs of the Ir oxidation process for each aliquoted electrodes are shown in Figure 3.8. This demonstrates the similar CV morphology and magnitude seen previously for the electrophoretically deposited electrodes. Some small variability in the magnitude of

the traces is again observed, and the correlation between this variability and the resulting Michaelis-Menten parameters of the transducer is analyzed in Section 3.5.3.2.

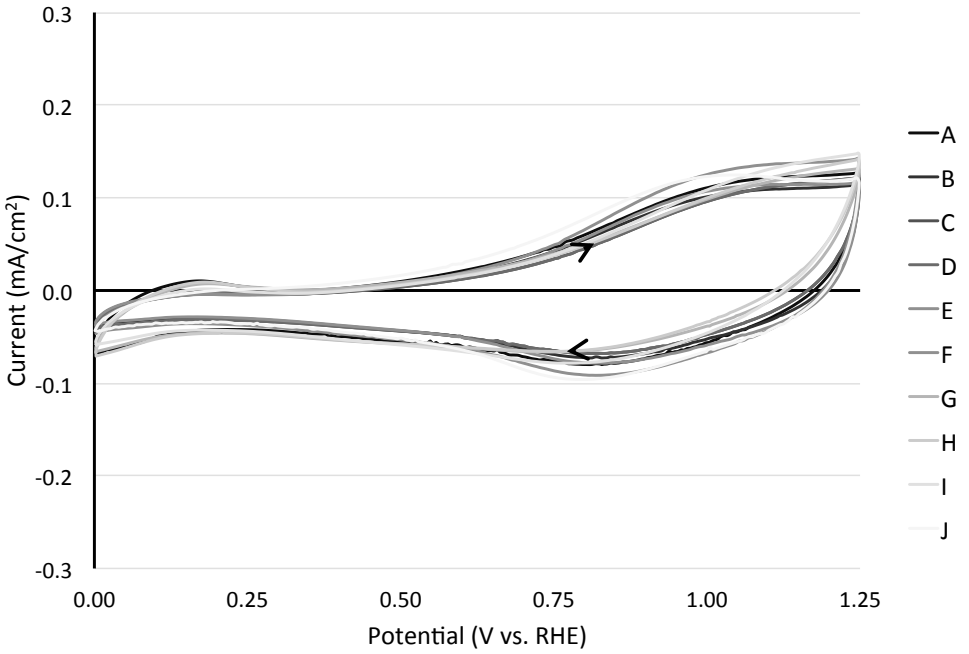

Figure 3.8: Superimposed plots of the final (65^{th}) Ir oxidation cycle for all aliquot depositted electrodes. CVs were performed under argon in a stirred PBS cell solution with a sweep rate of 100 mV/s.

3.2.4 Glucose Response Testing

Glucose testing was performed in the same manner as for the electrophoertically deposited GOx electrodes (Section 3.1) and according to the protocol in Chapter 2. This resulted in a plot of measured currents associated with cell solution glucose concentrations ranging from 0 mM to 18 mM. Figure3.4a shows the method of current sampling and averaging that was used to arrive at these individual measured currents. The same non-linear regression fit to the measured current points for each electrode was computed with MATLAB® to fit the Michaelis-Menten model. This resulted in the set of fitted Michaelis-Menten plots shown in Figure 3.9.

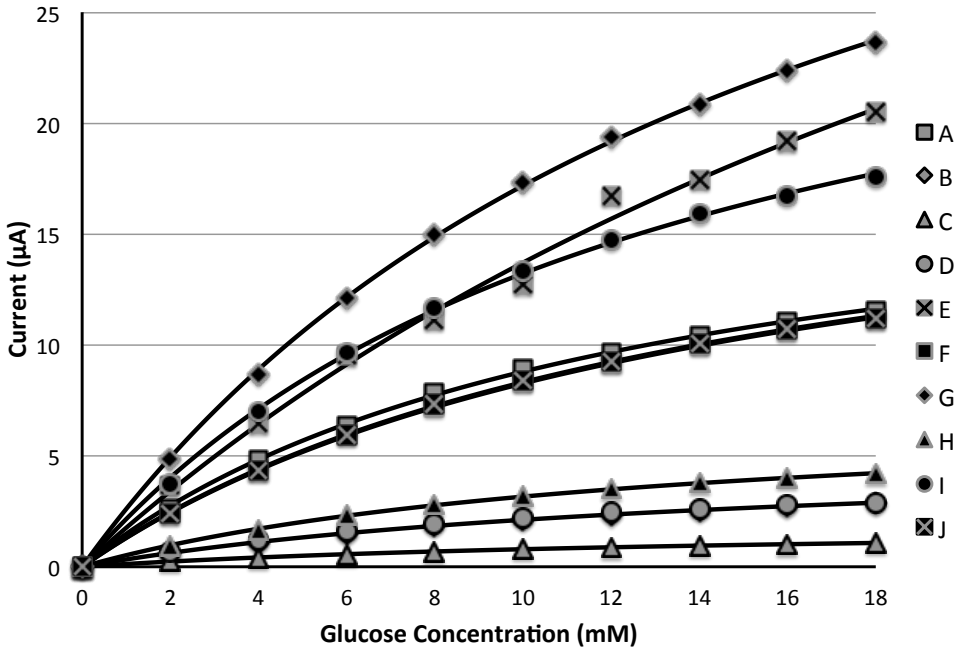

Figure 3.9: Michaelis-Menten plots for the aliquot deposited electrodes (labeled A-J). Each electrode's measured response is represented by the points, and the black lines show the resulting fitted Michaelis-Menten model for each electrode. This experiment was performed in a stirred PBSS solution that was not deoxygenated. The cell potential was held at 1.2 V vs. RHE. Each measurement has a maximum calculated percent error of $\pm$ 8 % on the x-axis, and $\pm$ 0.2 % on the y-axis. Again, the excellent fit of the Michaelis-Menten model to the measured data indicates that the actual percent error of the measurements was much lower.

The variability between electrodes is again quite large (similar to the electrophoretic deposition method, Section 3.1) and likely to exceed the 20 % clinically-acceptable percent error. This variability is quantified in Table 3.3 using the percent-error quantification method, described in Section 3.5.1.

The variation in performance of the electrodes (Figure 3.9, Table 3.3) exceeded the desired maximum of 20 %, in some cases quite significantly. It is also immediately apparent from the i_{max} values that the electrodes vary widely in performance, and the percent error column shows this in a clearer manner. The actual variation is massive, with the first standard deviation of the percent error being 150 percentage-points wide. From a practical perspective,

only 2 of the 10 (20 %) electrodes in the experimental batch would produce clinically safe and useful results.

Table 3.3: List of calculated I_{max} and K_m parameters for aliquot deposited electrodes. The percent error is the error in the reported glucose concentration vs. the true glucose concentration when using the batch mean values for i'_{max} and K'_m (see Section 3.5.1).

Electrode Sample #	$\boldsymbol{i_{max}}$ **(μA/cm²)**	$\boldsymbol{K_m}$ **(mM)**	**Percent Error**
A	190	12.1	11 %
B	52	15.0	-87 %
C	32	14.5	-93 %
D	83	12.6	-76 %
E	560	30.9	very large
F	200	14.8	-6.6 %
G	450	16.4	very large
H	72	12.9	-80 %
I	310	13.3	360 %
J	210	14.6	-5.5 %
Mean	220	15.7	3.0 %
Std. Dev.	180	5.49	150 %

Interestingly, the K_m values (Table 3.3) are far more repeatable than the i_{max} values. i_{max} is generally perceived in non-rigorous terms as a measure of the number of accessible enzyme sites and the reaction rate constant of the product-forming reaction, while K_m is interpreted as a measure of the enzyme's affinity for glucose molecules, which would be expected to be relatively constant. Visual inspection of the aliquot-deposited electrode surfaces showed macroscopic aggregation of the Ir on the electrode surface almost immediately after the aliquot was placed on the Au electrode surface (Figure 3.10). It was hypothesized that the variable aggregation resulted in blocking of GOx active sites by nearby Ir NPs, preventing glucose from accessing and binding to the active site on the enzyme. Prevention of electrical connection between GOx and IrOx NPs by IrOx aggregations is also proposed as a contributing factor that would reduce the ability for electrons to be conducted into the electrode and hence detected by the sensor electronics. Since the aggregation appeared to be

a stochastic process, the value of i_{max} would be expected to vary randomly. This may have resulted from the mixing of the ethanol-suspended Ir NPs with the water-suspended GOx prior to deposition on Au. Thus, the decision was made to separate the deposition of Ir sol on the electrode from the deposition of GOx, resulting in the 'Sequential Aliquot Deposition Electrodes', studied in Section 3.3.

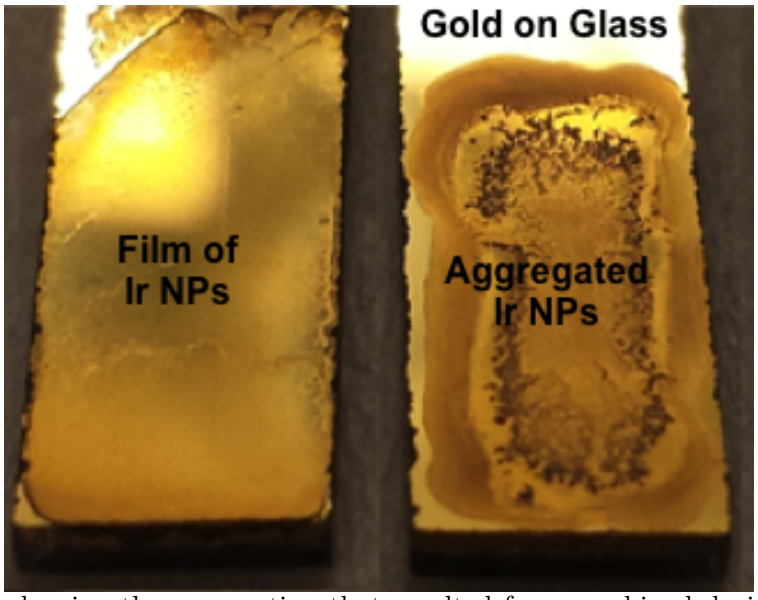

Figure 3.10: Photo showing the aggregation that resulted from combined drying of ethanolic and aqueous solutions. The electrode on the left consisted of only the Ir nanoparticles suspended in ethanol, and shows a macroscopically homogenous surface. The electrode on the right consisted of the same Ir nanoparticle ethanol sol, but with DI water added in a ratio of 4:1 by volume. The right hand electrode clearly shows stochastic aggregation of the Ir nanoparticles on the gold surface.

3.2.5 Validation of Michaelis-Menten Model

The Michaelis-Menten model for enzyme kinetics (Section 1.3) was again used to describe the transfer function of the aliquot deposited glucose transducers. Determination of the appropriateness of the Michaelis-Menten model for this electrode construction method was assessed using the same NRMSE method as was used for the electrophoretically deposited

electrodes (Section 3.1.5).

Table 3.4 enumerates the NRMSE for the fitted Michaelis-Menten models of all 10 electrodes in this experimental batch. The errors are again all less than 5 %, and all but one are less than 1 %. As a result, Michaelis-Menten enzyme kinetics were considered to be an excellent model to represent the electrodes produced by the aliquot deposition method.

Table 3.4: Summary of calculated NRMSEs for the aliquot deposited GOx electrodes.

Electrode Sample #	**Model NRMSE**
A	0.86 %
B	0.48 %
C	0.37 %
D	0.33 %
E	2.70 %
F	0.37 %
G	0.52 %
H	0.50 %
I	0.89 %
J	0.59 %
Mean	0.76 %
Std. Dev.	0.71 %

3.3 Sequential Aliquot Deposited Electrodes

The third method of electrode construction used the 'sequential aliquoting' technique. The ethanol-based Ir sol was deposited on the Au electrode surface first and allowed to dry, followed by aliquot deposition of the aqueous GOx enzyme and Nafion® together and further drying. Finally, electrochemical oxidation was performed in the same manner as for the electrodes in Sections 3.1 and 3.2 in order to convert the metallic Ir to IrOx. This was followed by the standard glucose response testing.

3.3.1 Au Cleaning

As in Sections 3.2 and 3.1, cleaning of the Au electrude surface was accomplished by electrochemical CV cycling in 0.5 M H_2SO_4, and the specific procedure is provided in Chapter 2. Figure 3.11 shows an overlay of the final CV cycle of all 7 electrodes that were used for this experiment. The CVs are very similar to one another, both in terms of peak potentials and current magnitudes.

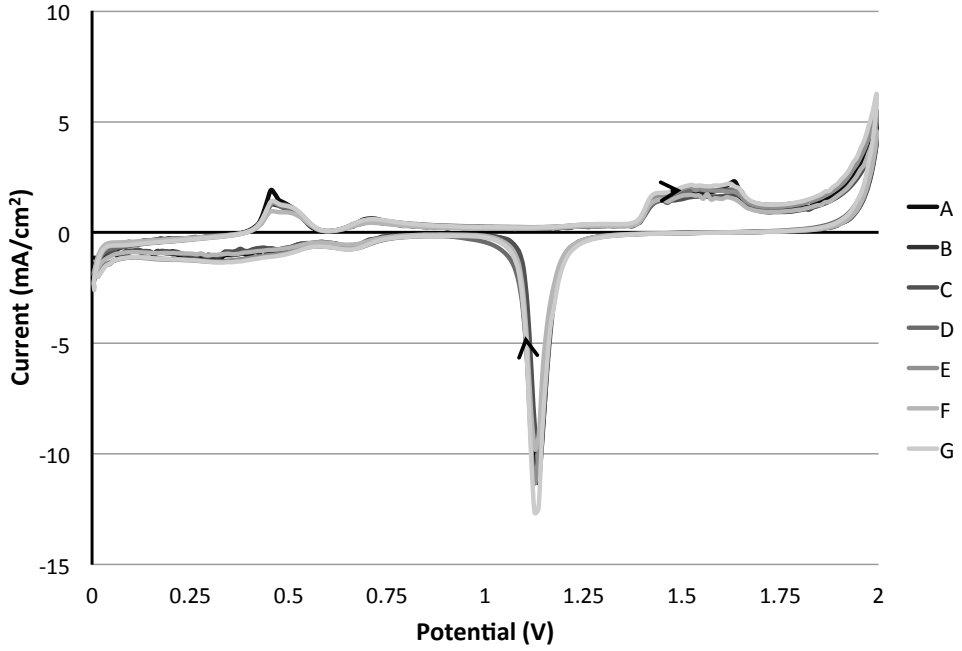

Figure 3.11: Plot of final Au cleaning CVs for the sequentially aliquoted electrodes. This experiment was performed in 0.5 M H_2SO_4, with stirring, and under deaerated conditions (with argon bubbled through the cell solution). The sweep rate of the potential was 100 mV/s.

3.3.2 Ir sol, GOx, and Nafion® Sequential Aliquot Deposition

As per the procedure in Section 2.2.2.3, 2 µL of the ethanol-based Ir sol was aliquoted onto the bare Au electrode first and allowed to dry over a period of 24 hours. Subsequently, 1 µL of aqueous 1:1 GOx solution:Nafion® solution was layered on top in a second aliquot

deposition step, and the electrode allowed to dry completely, again over 24 hours. The aliquoted Ir solution was visible on the electrode due to the dark colour of the metal, and the film remained macroscopically homogenous, with no obvious aggregation seen on any of the electrodes. The GOx:Nafion® solution was colourless and thus was not visible on the surface following drying, and it did not seem to disturb the Ir distribution.

3.3.3 Ir Oxidation

Once the Ir sol, and then the GOx/Nafion® mixture was deposited on the electrode surface in separate steps, the Ir metal was oxidized to IrOx using the same electrochemical cycling method as used for the electrophoretically deposited and aliquot deposited electrodes (Sections 3.1.2 and 3.2.3), and as detailed in Chapter 2. Figure 3.12 shows the difference between the trace of the first CV cycle and the trace of the 65th (and final) CV cycle. The decrease in the H_{UPD} peak at point 'A' in the figure indicates a decrease in the amount of metallic Ir available (Section 2.3.2), while the increase in the current magnitude at point 'B' indicates the increased amount of IrOx present in the surface film.

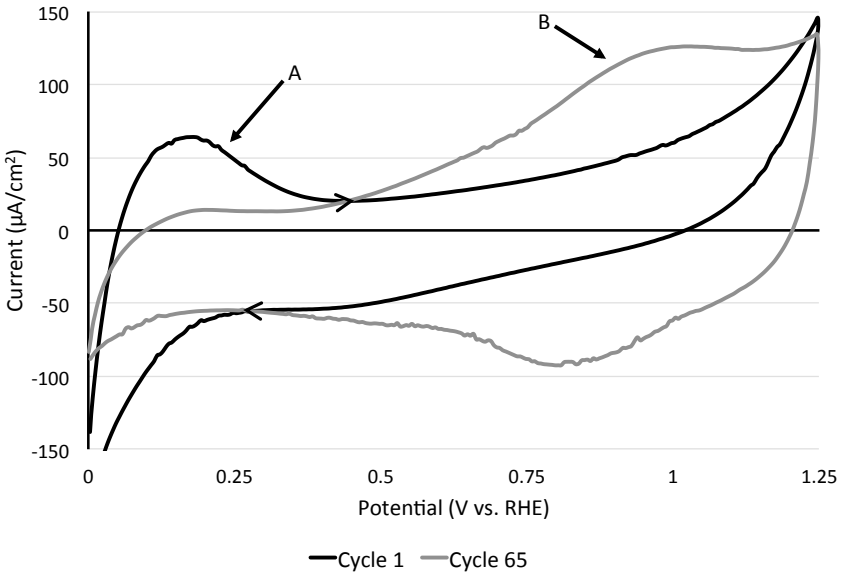

Figure 3.12: Sample CV showing the conversion of Ir to IrOx over the course of 65 CV cycles for the sequential aliquot deposited electrodes. Point 'A' shows the decrease in metallic Ir available for hydrogen adsorption, while point 'B' shows the increase in IrOx quantity. This experiment was performed in PBS under argon and the was stirred throughout the experiment. The sweep rate of the electrical potential was 100 mV/s.

Figure 3.13 overlays all of the final (65^{th}) CV cycles for the sequential aliquot deposited electrodes. The result is very similar to the previous electrodes in terms of morphology and the small but noticeable variability, though the peak currents are approximately 30 % larger. This may have resulted as a slightly larger amount of Ir was deposited on these electrodes. As in previous electrode construction methods, the correlation between the variability in this plot and the resulting variability in the Michaelis-Menten parameters is analyzed in Section 3.5.3.3.

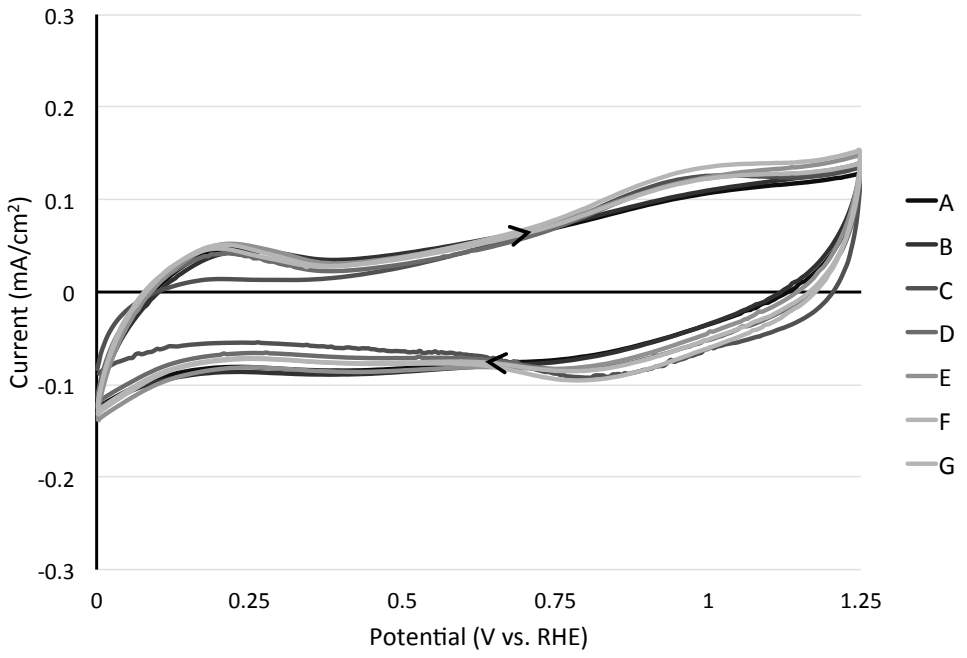

Figure 3.13: Superimposed plots of the final (65^{th}) Ir oxidation cycle for all sequential aliquot deposited electrodes. The CVs were collected under argon in a stirred PBS cell solution, with a potential sweep rate of 100 mV/s.

3.3.4 Glucose Response Testing

The glucose testing experiment was again performed according to the protocol given in Section 2.3.3, and the resulting plot of the fitted Michaelis-Menten curves to the measured data points is provided in Figure 3.14. The measured currents were once again derived as the mean of the middle 30 seconds of current samples for each 50 second period that the cell was maintained at a particular glucose concentration.

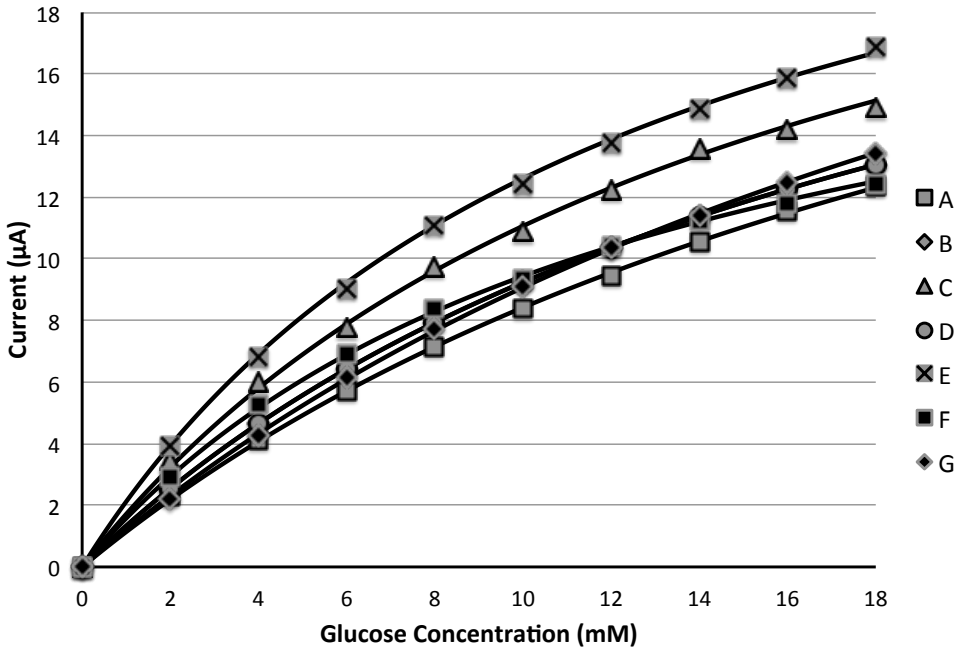

Figure 3.14: Resulting Michaelis-Menten plots for the sequentially aliquoted electrodes (labeled A-G). Each electrode's measured response is represented by the points, and the black lines show the resulting fitted Michaelis-Menten model for each electrode. This experiment was performed in a stirred PBSS solution that was not deoxygenated, and the cell potential was held at 1.2 V vs. RHE. Each measurement has a maximum calculated percent error of ± 8 % on the x-axis and ± 0.2 % on the y-axis. As in the previous two experimental groups, the excellent model fit to the measured data indicates that the percent error was in practice much smaller.

Some variability between electrodes is still present, but it is markedly reduced as compared to the electrophoretically deposited (Figure 3.5) and aliquot deposited (Figure 3.9)

transducer electrodes. The variability for the separately-aliquotted transducers is quantified in Table 3.5 using the percent-error quantification method described in Section 3.5.1.

Table 3.5: List of calculated i_{max} and K_m parameters for sequentially aliquoted test electrodes (Figure 3.14. The percent error is the error in the reported glucose concentration vs. the true glucose concentration when using the batch mean values for i'_{max} and K'_m. See section 3.5.1.

Electrode Sample #	$\boldsymbol{i_{max}}$ **(µA/cm²)**	$\boldsymbol{K_m}$ **(mM)**	**Percent Error**
4.A	290	24.6	-21 %
4.B	270	19.2	-12 %
4.C	280	15.3	25 %
4.D	280	18.1	4 %
4.E	280	12.2	55 %
4.F	210	12.4	-22 %
4.G	340	27.2	-15 %
Mean	280	18.4	-2.5 %
Std. Dev.	39	5.79	6.6 %

These results demonstrate a far more repeatable transducer electrode as compared to both the electrophoretic deposition electrodes (Table 3.1) and the aliquot deposition electrodes (Table 3.3). The standard deviation of the percent error was 6.6 % (as compared to 49 % for the electrophoretically deposited electrodes and 150 % for the aliquot deposited electrodes), meaning that approximately 99.6 % of the electrodes should lie within the desired 25 % error band, assuming a normal distribution and a sufficient number of samples. In this particular sample set, 1 out of 7 electrodes lies significantly outside this range, which, while not ideal, is acceptable in a prototype. Due to these quite favourable results, development of the embedded potentiostat circuit for the e-Mosquito prototype was undertaken to match the electrical characteristics of the sequential aliquot deposited transducers.

3.3.5 Validation of Michaelis-Menten Model

The Michaelis-Menten model for enzyme kinetics (Section 1.3) was once again validated, against the measured data for the electrodes in this experiment, for use as a model describing

the behaviour of sequentially aliquoted electrodes. The NRMSE was again calculated (using the method in Section 3.1.5) for all of the test electrodes (electrodes A – J), and the results are given in Table 3.6. The errors of the Michaelis-Menten fit are all less than 5 %, indicating that Michaelis-Menten enzyme kinetics are an excellent model for the behaviour of the sequentially aliquoted glucose transducers.

Table 3.6: Summary of calculated NRMSEs for the sequential aliquot deposited GOx electrodes.

Electrode Sample #	**Model NRMSE**
A	0.55 %
B	1.08 %
C	1.15 %
D	1.57 %
E	1.13 %
F	1.00 %
G	0.81 %
Mean	1.04 %
Std. Dev.	0.32 %

3.4 Nanoparticulate Nature of Iridium Sol

While it has been shown previously in transmission electron microscopy (TEM) imaging performed by Irhayem [42] that the Ir sol method used here produces a suspension of nanoparticles, it is difficult to image these nanoparticles via TEM with GOx and Nafion® present. As a result, a simpler method to verify the presence of nanometer-sized nanoparticles was used to verify this fact. The electrochemically active surface area of the films was measured, and this information was used to calculate the mean nanoparticle diameter. The H_{UPD} peak is generated by the underpotential adsorption and desorption of a monolayer of hydrogen on the Ir surface with a predictable surface charge density of 1.37 C/m^2 [98]. The area under the H_{UPD} peak (shown in Figure 3.15) is by definition the total amount of charge transferred

by the deposition of hydrogen on the Ir surface. This area was calculated for electrode 'A' of the electrophoretic deposition experiment, and was found to be $q_{H_{UPD}} = 726.0\,\mu$C. Equation 3.2 shows that the electrochemically-active surface area ($5.30\,\text{cm}^2$) is much larger than the geometric surface area of the electrode ($0.1\,\text{cm}^2$).

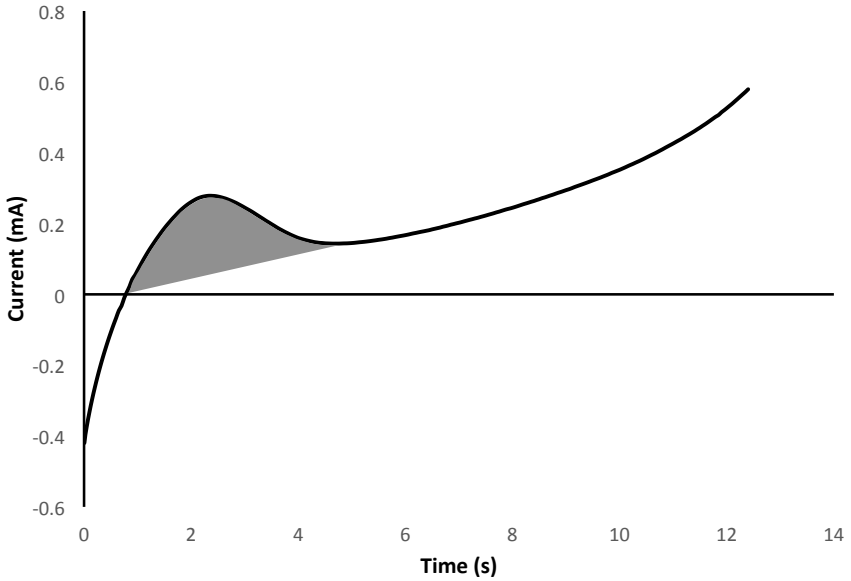

Figure 3.15: Region of the CV that was integrated to determine the amount of charge transferred by underpotential adsorption of hydrogen. The charge transferred was used in conjunction with the surface charge density of hydrogen on Ir to calculate the true surface area of Ir.

$$A_{Ir} = 726 \times 10^{-6}\,\text{C} \times \frac{1\,\text{m}^2}{1.4\,\text{C}} = 5.3 \times 10^{-4}\,\text{m}^2 = 5.3\,\text{cm}^2 \tag{3.2}$$

Following determination of the total surface area available for electrochemical interactions on the transducer, several key assumptions were made:

- The nanoparticles are perfectly spherical. Previous TEM imaging is supportive of this assumption [42].
- The full surface area of each nanoparticle is electrochemically available.

- Au does not exhibit H_{UPD} peaks, and hence does not confound this analysis. This can be seen in Figures 3.2, 3.7, and 3.12, where there is no reversible peak present in the $0.0 - 0.5\,\mathrm{V}$ vs. RHE range of the Au CV.

This resulted in two equations that related the total volume of Ir present (V_{Ir}), the total surface area of the Ir NPs (A_{Ir}), the number of Ir NPs (n), and the mean radius of the NPs (r) (Equations 3.3 and 3.4).

$$V_{Ir} = n \cdot V_{NP} = n \cdot \frac{4}{3}\pi r^3 \tag{3.3}$$

$$A_{Ir} = n \cdot A_{NP} = n \cdot 4\pi r^2 \tag{3.4}$$

These equations can then be rearranged in order to give an expression for the radius in terms of the total volume and surface area of all of the Ir NPs on the electrode (Equation 3.5).

$$\begin{aligned} n = \frac{V_{Ir}}{V_{NP}} &= \frac{3 \cdot V_{Ir}}{4 \cdot \pi r^3} \\ n = \frac{A_{Ir}}{A_{NP}} &= \frac{A_{Ir}}{4 \cdot \pi r^2} \\ \frac{3 \cdot V_{Ir}}{4 \cdot \pi r^3} &= \frac{A_{Ir}}{4 \cdot \pi r^2} \\ 3 \cdot V_{Ir} r^2 &= A_{Ir} r^3 \\ r &= \frac{3 \cdot V_{Ir}}{A_{Ir}} \end{aligned} \tag{3.5}$$

Calculating the total volume of Ir on the transducer following a $1\,\mu$L aliquot deposition of the Ir sol was a simple process. Using the room temperature density for Ir of $2.3 \times 10^7\,\mathrm{g/m^2}$ [94] resulted in $V_{Ir} = 8.5 \times 10^{-13}\,\mathrm{m^3}$. These values were applied to Equation 3.5, giving the result shown in Equation 3.6.

$$
\begin{aligned}
r &= \frac{3 \cdot V_{Ir}}{A_{Ir}} \\
&= \frac{3 \cdot (8.5 \times 10^{-13}\,\mathrm{m}^3)}{5.3 \times 10^{-}4\,\mathrm{m}^2} \\
&= 4.8 \times 10^{-9}\,\mathrm{m}
\end{aligned} \tag{3.6}
$$

This result of a mean nanoparticle radius of 4.8 nm showed that the Ir NPs had sizes on the expected nanometer scale, and is well within the same order of magnitude as the previously determined result of $1 - 3$ nm [42]. The H_{UPD} peaks for all transducers were similar, indicating that all films were nanparticulate with mean nanoparticle radius of roughly 4.5 nm.

3.5 Error Analysis

The results presented in Sections 3.1, 3.2, and 3.3 show significant variability in the glucose response between individual transducers. While it is likely that a large amount of this variability can be attributed to transducer construction methods, this section shows the methods used to quantify this variability.

3.5.1 Transducer Percent Error Quantification

This section describes the manner in which the percent errors presented in the above three sections were derived. Modelling of the complete system that transforms a glucose concentration in a sample into the glucose concentration reading obtained is a process that actually involves two applications of the Michaelis-Menten equation (Section 1.3, Figure 3.16). The value of interest is the percent error of the displayed glucose concentration vs. the true glucose concentration, and hence this model is used in calculating the accuracy of the transducers.

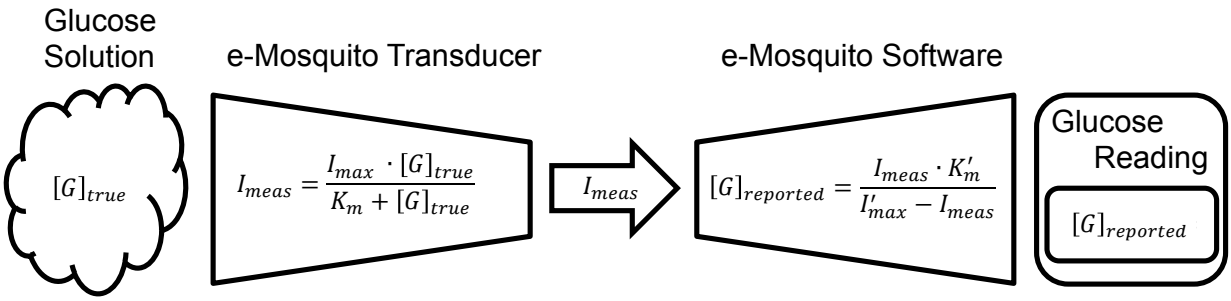

Figure 3.16: The error model used in assessing sensor performance results. The glucose concentration ($[G]_{true}$) is initially transformed into a proportional electrical current (I_{meas}), which is then measured by the e-Mosquito processor. The processor then uses a set of internally programmed calibration parameters (K'_m and I'_{max}) to convert this back into a reported glucose concentration ($[G]_{reported}$).

In the first, or forward, application of the Michaelis-Menten equation, the actual K_m and I_{max} parameters for the particular, individual transducer combine mathematically with the true concentration of glucose in the sample to produce the current measured by the transducer element. In the second, or backwards application of the equation, the software in the device uses the programmed calibration K'_m and I'_{max} values (derived as the mean K_m and I_{max} of all the transducers in the experimental group), along with the measured current from the transducer, to produce a glucose concentration measurement (Equation 3.7 shows the Michaelis-Menten equation re-arranged in terms of I_{meas} to yield the reported glucose concentration, $[G]_{reported}$. I'_{max} is the calibration value of I_{max} for the sensor batch and K'_m is the calibration value of K_m for the particular sensor batch). The second application of the equation is the process that is performed mathematically by the e-Mosquito microprocesor in the real prototype in order to arrive at the reported glucose concentration. The error value of interest is the percentage error between the true glucose concentration in the sample and

the glucose concentration reported by the sensor device (Equation 3.8).

$$\begin{aligned} I_{meas} &= \frac{I'_{max} \cdot [G]_{reported}}{K'_m + [G]_{reported}} \\ [G]_{reported} \cdot (I'_{max} - I_{meas}) &= I_{meas} \cdot K'_m \\ [G]_{reported} &= \frac{I_{meas} \cdot K'_m}{I'_{max} - I_{meas}} \end{aligned} \tag{3.7}$$

$$PE = \frac{[G]_{reported} - [G]_{true}}{[G]_{true}} \times 100\,\% \tag{3.8}$$

As mentioned previously, the average of all of the K_m and I_{max} parameters measured for the individual transducer electrodes in a single experimental batch (i.e., those made by the same construction method) was used as the calibration reference (the parameter values that would be programmed into the e-Mosquito microprocessor) to simulate a production environment. In a real production environment where all of the transducers could not be used to arrive at the calibration values (as some need to be left-over for use by patients), random electrodes, constituting a representative sample of the particular transducer population, would be characterized in order to arrive at calibration values for the remaining electrodes in the batch.

Figure 3.17 (using sample data only) details the error characteristics of a single transducer relative to the programmed calibration values. This type of plot is a simplified version of the Clarke Grid [66], and shows the measured (reported) glucose concentration vs. the true glucose concentration in solution. The response of a perfect sensor would lie exactly along the unit-slope line, representing a 1:1 equivalency between the reported and true glucose concentrations. Any deviation from this line (dotted line in Figure 3.17) indicates an error on the part of the sensor. Typically, an error of up to 20 % from the reference glucose concentration is considered 'clinically accurate', and a small amount ($< 5\,\%$, region B of

the Clarke Error Grid) of additional error is generally considered to 'not affect treatment decisions' [66]. This seems like a large range of error. However, the devices that the Clarke Error Grid (Figure 1.6) is used to characterize are for ongoing monitoring, and are never used in a diagnostic capacity. Therefore the only item of concern is whether the sensor inaccuracy would result in incorrect treatment decisions.

In order to simplify this complete (and complex) picture of the transducer error and its dependence on the true glucose concentration, the percent error (accuracy) of a particular transducer in this thesis is reported as a single number to ease comparison. This number is the maximum magnitude of the percent error within the clinically-relevant range of 0 mM to 20 mM.

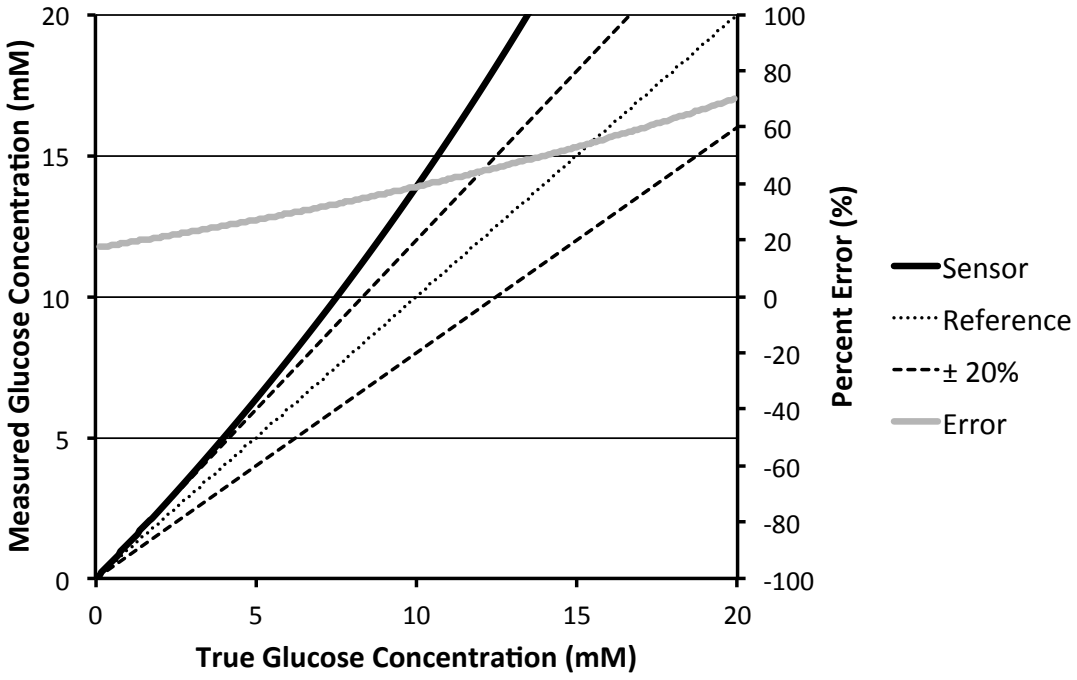

Figure 3.17: This plot shows the relation between a particular true glucose concentration and the concentration measured by a physical sensor. The central dotted line shows the ideal relation (a perfectly accurate transducer), while the two other dashed lines show the "clinically accurate" 20 % boundaries. The solid black line is the response of the transducer (left-hand axis) and the gray line shows the percent error of the transducer at all relevant glucose concentrations (right-hand axis). As can be seen, the error of the transducer is not always a constant percentage in cases where the I_{max} value of the transducer is not the same as the calibration I'_{max} value programmed into the device. This is the error plot for sensor 'E' from the electrophoretic deposition experiment. These plots were generated for every transducer that was tested, but not all plots were included in this document due to space concerns. Instead, the most important metric (maximum percent error across the clinically significant range of glucose concentrations) was included as a primary result for each transducer.

3.5.2 Sources of Error

Several sources of error were present in the testing of the electrodes, the most significant being the various noise sources. Electrical interference was frequently observed, particularly when the stopcock in the regular hydrogen electrode (RHE) was extremely tight, causing the RHE to act as an antenna. There were also observed instances of the magnetic stir-plate causing electrical artifacts in the measured electrical current. The noise was of sufficiently high frequency such that its effect was mitigated by the 30 second averaging window used in sampling the time-plot (which acts as a low-pass filter).

Chapter 2 notes that the first glucose addition (from 0 mM to 2 mM) was smaller than the next (from 2 mM to 4 mM) due to the cell solution volume being increased by the volume of the first glucose addition. While this difference was taken into account in the volumetric calculations (Table 2.1 in Section 2.3.3), the actual syringe used to deliver glucose additions did not have sufficient accuracy for these very small deviations and, as such, they were only roughly approximated in practice. This may have resulted in a small amount of error (calculated below) in the results arising from slightly inaccurate glucose concentrations, although these errors should be the same for all tests and would not have an effect on the variability of the sensor.

The potentiostat itself is unlikely to have generated noticeable error via measurement inaccuracies, as the listed current error is ±0.2 % for the range of currents measured in this experiment [99]. All reagents were (as listed in Chapter 2) of 99-98 % purity, while the balances used have an accuracy of ±50 µg, which yields a percent error of between 0.1 % and 0.25 %. Finally, the syringes used were accurate to approximately 2.5 µL, which results in a percent error for the glucose delivered by syringe of approximately 5 %. There is also error resulting from inaccuracies in the cell volume that was measured using a graduated cylinder. The cylinder used was accurate to a volume of 50 µL, resulting in a percent error of 2.5 %. All of these error result in an estimated maximum attributable error of approximately 8 %.

3.5.3 Ir Oxidation Variability and i_{max} and K_m Interaction

The variability in the magnitude of the currents in the final Ir oxide CVs (Figures 3.3, 3.8, and 3.13) is relatively small, but is concerning for its potential import on the resulting i_{max} and K_m values. Correlation plots were thus generated, comparing the peak anodic (i_a) and peak cathodic (i_c) CV currents observed for the IrOx in each transducer during the final Ir oxidation CV (Figure 3.18) with the values of i_{max} and K_m that were calculated for that transducer. This section is divided by the sensor construction methods used to make the transducers.

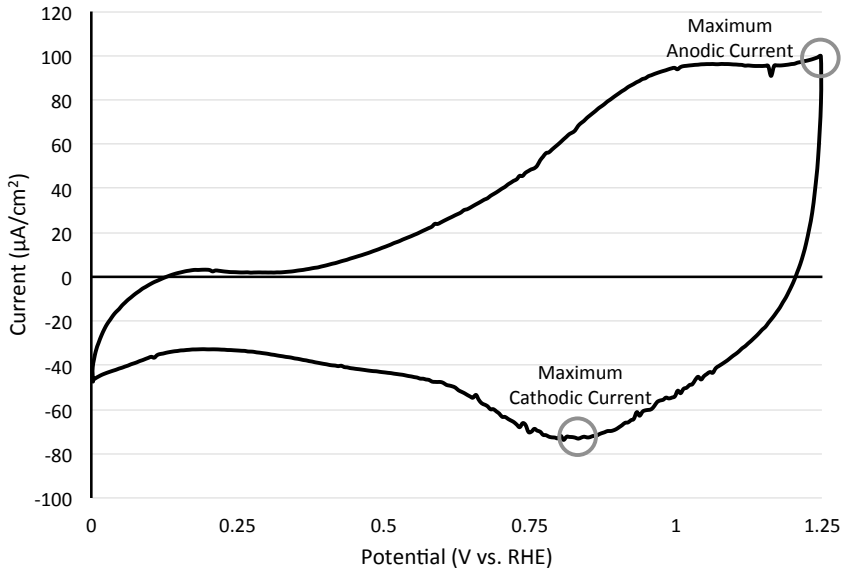

Figure 3.18: Example of the maximum anodic and cathodic currents on a sample Ir oxidation CV.

The Pearson's product-moment correlation (r, often called the correlation coefficient) is a measure of the correlation of two variables, and its magnitude is equal to the square-root of the coefficient of determination (R^2) for the linear regression fit between the two variables. This value was calculated, and then the Student's t-test was used to determine whether the strength of the correlation was statistically significant to a level of $\alpha = 0.05$.

3.5.3.1 Electrophoretically Deposited Electrodes

Correlation plots for the electrophoretically deposited electrodes are shown in Figure 3.19. The maximum anodic current correlation with i_{max} gave a Pearson's correlation coefficient of $r = 0.26$, while the maximum cathodic current correlation with i_{max} gave $r = 0.66$. Application of the t-test to these correlation coefficients yielded non-significant p-values in both cases ($p = 0.74$ and $p = 0.34$, respectively). In terms of K_m, the maximum anodic current correlation had a Pearson's correlation coefficient of $r = 0.64$, while the maximum cathodic current correlation gave $r = 0.68$. Using the Student's t-test resulted in non-significant p-values in both cases ($p = 0.36$ and $p = 0.32$, respectively). These p-values are

given in Table 3.7.

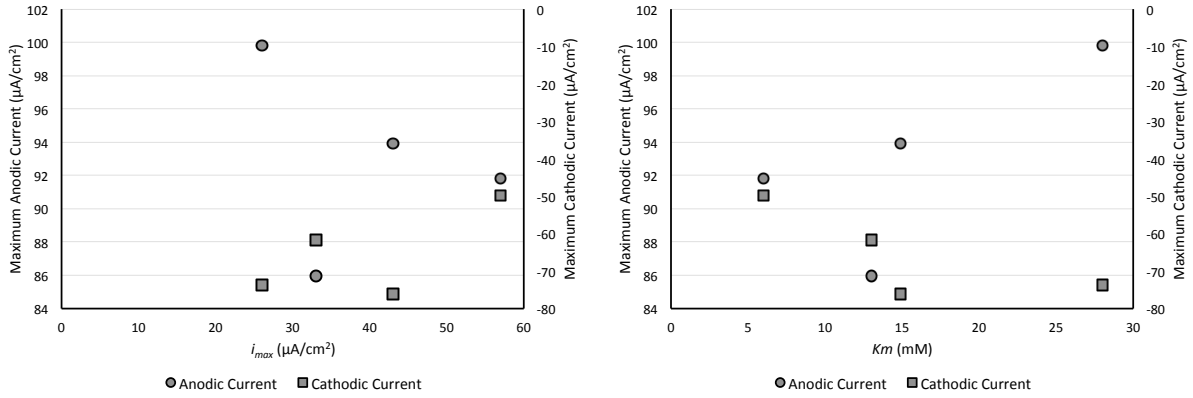

Figure 3.19: Correlation plot of i_{max} (left) and K_m (right) with the anodic (left-hand axis) and cathodic (right-hand axis) currents for the electrophoretically deposited electrodes. Data for this plot were derived from Section 3.1. The i_{max} correlation R^2 value for the anodic peak is 0.07, and for the cathodic peak is 0.43. The K_m correlation R^2 value for the anodic peak is 0.41, and for the cathodic peak is 0.48.

Table 3.7: Summary of p-values for the correlation between the maximum anodic and cathodic IrOx CV currents (i_a and i_c), and the Michaelis-Menten values i_{max} and K_m for the electrophoretically-deposited electrodes.

IrOx CV Parameter	**M-M Parameter**	**Correlation *P*-value**
i_a	i_{max}	0.74
i_a	K_m	0.36
i_c	i_{max}	0.34
i_c	K_m	0.32

The conclusion drawn from these results is that there is no significant correlation between the variability in the Ir oxidation CVs and the variability in the transducer performance. Hence, the variable performance of the electrophoretically-deposited electrodes must be arising from another source, such as the Ir and GOx phase distribution on the surface as noted earlier.

3.5.3.2 Aliquot Deposited Electrodes

Correlation plots for the aliquot deposited electrodes were also generated and are shown below in Figure 3.20. The correlation of i_{max} with i_a gave a correlation coefficient of $r = 0.56$, while the correlation of i_{max} and i_c gave $r = 0.37$. Applying the t-test to these values gave non-significant p-values ($p = 0.09$ and $p = 0.29$, respectively). In terms of K_m, the i_a correlation had a correlation coefficient of $r = 0.35$, while the i_c correlation gave $r = 0.45$. T-tests in this case gave non-significant p-values as well ($p = 0.33$ and $p = 0.20$ respectively). These p-values are given in tabular form in Table 3.9.

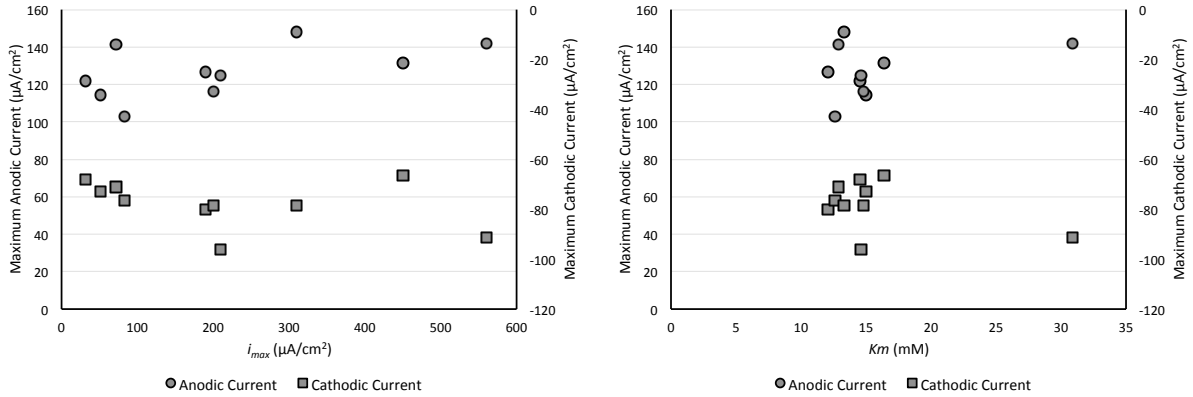

Figure 3.20: Correlation plot of i_{max} (left) and K_m (right) with the anodic (left-hand axis) and cathodic (right-hand axis) currents for the aliquot deposited electrodes. Data for this plot were derived from Section 3.2. The i_{max} correlation R^2 value for the anodic peak is 0.31, and for the cathodic peak is 0.14. The K_m correlation R^2 value for the anodic peak is 0.12, and for the cathodic peak is 0.20.

Table 3.8: Summary of p-values for the correlation between the maximum anodic and cathodic IrOx CV currents (i_a and i_c), and the Michaelis-Menten values i_{max} and K_m for the aliquot deposited electrodes.

IrOx CV Parameter	**M-M Parameter**	**Correlation *P*-value**
i_a	i_{max}	0.09
i_a	K_m	0.33
i_c	i_{max}	0.29
i_c	K_m	0.20

This analysis showed similar results to the electrophoretic method in that there were no significant correlations between the values. While the correlation between i_a and i_{max} approaches significance, it does not attain the level of 0.05 required.

3.5.3.3 Sequential Aliquot Deposited Electrodes

As in Sections 3.5.3.1 and 3.5.3.2, correlation plots for sequential aliquot deposited electrodes were created and are shown in Figure 3.21. The correlation of i_a with i_{max} gave $r = 0.56$, while the correlation of i_c with I_{max} gave $r = 0.1$. T-test analysis of these values yielded non-significant results in both cases ($p = 0.19$ and $p = 0.83$ respectively). In terms of K_m, the correlation of i_a gave $r = 0.68$, while the i_c correlation gave $r = 0.00$. Appying the t-test resulted in non-significance in both cases ($p = 0.09$ and $p = 1$ respectively). These data are given in Table 3.9.

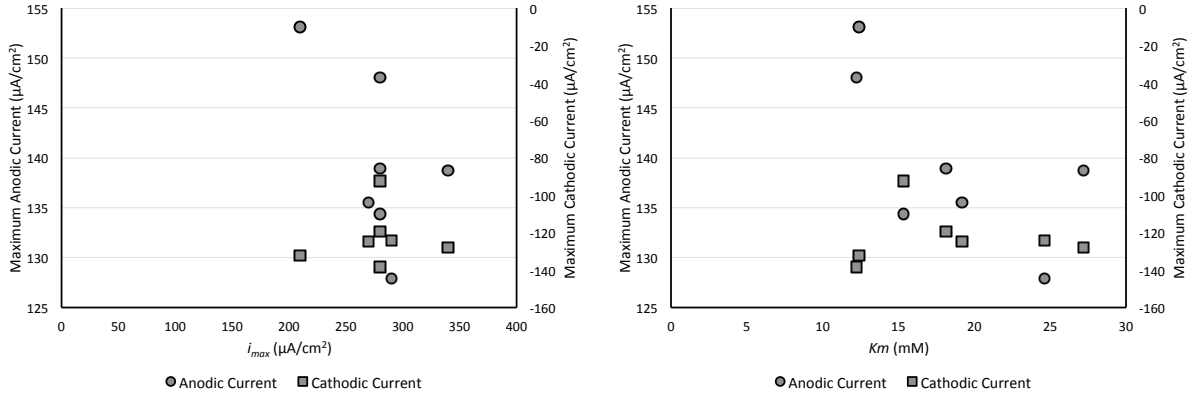

Figure 3.21: Correlation plot of i_{max} (left) and K_m (right) with the anodic (left-hand axis) and cathodic (right-hand axis) currents for the sequentially aliquoted electrodes. Data for this plot were derived from Section 3.3. The i_{max} correlation R^2 value for the anodic peak is 0.31, and for the cathodic peak is 0.01. The K_m correlation R^2 value for the anodic peak is 0.46, and for the cathodic peak is 0.00.

These results once again indicate (in keeping with the correlation results for electrophoretically deposited electrodes in Section 3.5.3.1 and aliquot deposited electrodes in Section 3.5.3.2) that there was no statistically significant correlation between the Michaelis-Menten

Table 3.9: Summary of p-values for the correlation between the maximum anodic and cathodic IrOx CV currents (i_a and i_c), and the Michaelis-Menten values i_{max} and K_m for the aliquot deposited electrodes.

IrOx CV Parameter	**M-M Parameter**	**Correlation *P*-value**
i_a	i_{max}	0.19
i_a	K_m	0.09
i_c	i_{max}	0.83
i_c	K_m	1.00

parameters and the Ir oxidation CV for any of the transducers. This once again indicates that the obseved variability (albeit reduced in the case of the sequentially-aliquoted electrodes) must be caused by other processes, such as the Ir and GOx morphology resulting from the electrode construction techniques used.

3.5.4 i_{max} and K_m Interaction

Substantial variability also existed in the i_{max} and K_m parameters. It is less clear whether there is an interaction between the value of the i_{max} parameter and the K_m parameter. Such an interaction would be useful as it might allow prediction of one of the transducer parameters from the other, and may suggest potential mechanisms for the inter-transducer variation that was observed. One way of visually identifying such an inter-dependence is with an interaction, or cross, plot. This is shown in Figure 3.22, plotting one variable against the other, allowing patterns in the data to be observed.

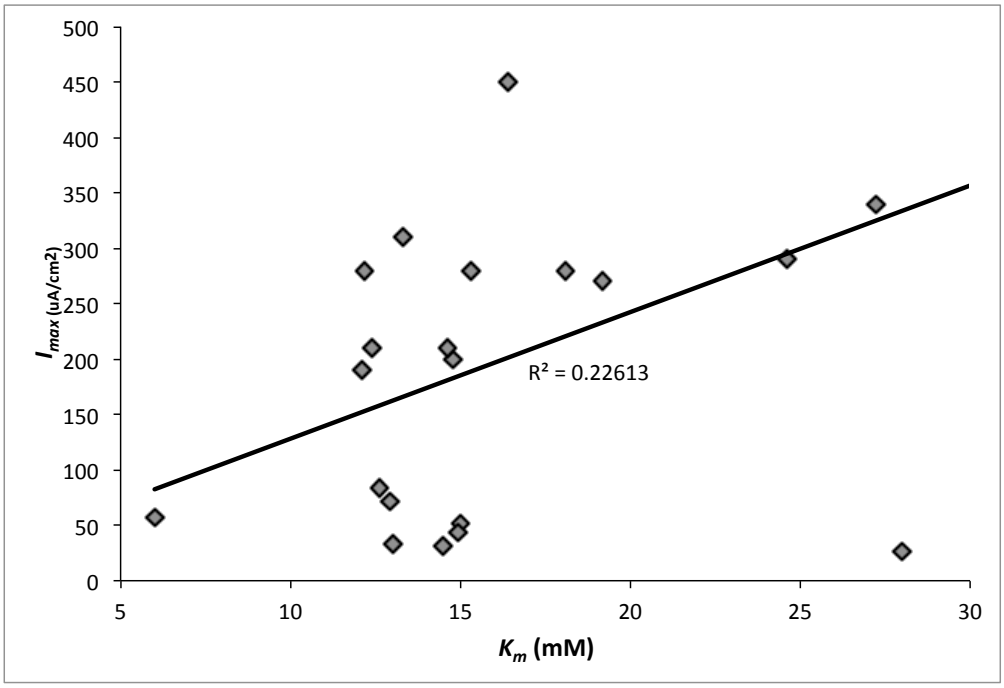

Figure 3.22: Interaction plot of K_m (x-axis) vs. i_{max} (y-axis). The distribution of the points, as well as the very poor best fit line, indicates that there is no interaction between the parameters.

This plot demonstrates no evidence for interaction between the two variables. There does not visually appear to be any correlation between i_{max} and K_m, which is further evidenced by the R^2 value of only 0.23, indicating a very poor linear fit. This does not notably improve using a 2$^{\text{nd}}$ or 3$^{\text{rd}}$ order polynomial fit (R^2 of 0.23 and 0.26, respectively). The decision was made not to fit with high-order polynomials, as any data can be fit to arbitrary precision by an arbitrarily high-order polynomial, and there are very few natural phenomena that are described by polynomials of order > 3. In addition, it is unclear what the utility of such a high-order interaction would be if it did exist.

3.6 Summary

In this chapter, three approaches were used to construct IrOx-based glucose transducers. These transducers were shown to be well-represented by the Michaelis-Menten model of

enzyme kinetics, by virtue of having normalized root mean squared errors of $< 2\,\%$ in all cases.

Electrophoretic deposition of GOx (Section 3.1) was the first construction method used. It showed relatively small current densities (i_{max} of $20\,\mu A/cm^2$ to $60\,\mu A/cm^2$), and large variability between individual transducers (standard deviation of the percent error of $45\,\%$). The process also required large and wasteful amounts of GOx enzyme, and so was abandoned early on.

The aliquot deposition technique was the next approach tested (Section 3.2), where the Ir sol, GOx, and Nafion® were physically deposited on the Au thin-film in a single solution aliquot, and were allowed to dry for 24 hours prior to testing. These electrodes resulted in much larger signals (mean i_{max} of $220\,\mu A/cm^2$) but demonstrated the largest variability between transducers of any method tested (the standard deviation of the percent error was $150\,\%$) and hence was essentially unusable in any clinical situation. It was theorized that this was a result of stochastic drying processes resulting from the mixing of an ethanol-based Ir sol with a water-based GOx and Nafion® solution.

The drying issue led to the use of the sequential aliquot deposition technique, where the ethanol-based Ir sol was placed first, followed by the aqueous GOx and Nafion® solution (Section 3.3). These electrodes gave large currents (mean i_{max} of $280\,\mu A/cm^2$) and substantially improved accuracy and precision (mean percent error of $-2.5\,\%$ and standard deviation of percent error of $6.6\,\%$). This method was selected as the most efficacious, although there was still pronounced variability (and hence error).

Finally, an analysis was undertaken in order to attempt to explain some of the demonstrated variability. The magnitude of the maximum cathodic and maximum anodic currents in the Ir oxide CVs was tested for correlation with the calculated values of i_{max} and K_m for each electrode in all three experimental groups. Furthermore, i_{max} was itself tested for correlation against K_m for all sensors. Each correlation was analyzed using Student's t-test, but no statistically significant correlation was found.

Chapter 4

Potentiostat Design and Testing

The electrochemical work described in previous chapters forms the transducer portion of the e-Mosquito glucose sensor. However, the complete e-Mosquito glucose sensor consists of both the transducer (to convert glucose concentration into an electrical signal) and the associated control and measurement electronics. This chapter describes three main areas of the project: design and implementation of the sensor electronics, testing and validation of the electronics, and integration of the sensor electronics into the existing e-Mosquito prototype.

4.1 Existing Systems

Several articles and books over the last several decades have described the design of small-scale, integrated chip electrochemical potentiostats [100, 101, 102]. There have been a variety of VLSI integrated potentiostat designs, many of them for recording neural electrical potentials [103, 104]. These potentiostats are generally based around a set of operational amplifiers that are constructed in a VLSI (Very Large Scale Integration) chip. These typically use Complementary Metal-Oxide Semiconductor (CMOS) chips due to their established nature, as well as their reputation for low noise and low power consumption.

One method of further reducing noise and power draw has been to reduce the number of operational amplifiers in the design. Several VLSI potentiostats were designed using a single operational amplifier to control the cell potential, and a simple current mirror for CE and WE control [105, 106]. While a current mirror forms a core part of an operational amplifier, the removal of the rest of the operational amplifier architecture results in a lower power

consumption and fewer transistors to add noise to the output.

Steinberg and Lowe published a design for an amperometric potentiostat for use in electrochemical biosensors, very similar to the requirements of the e-Mosquito [101]. This design was an effort to improve the output current measurement by directly converting the output current to a digital signal, rather than converting it to a voltage for measurement with a traditional analog-to-digital converter. The work by Narula and Harris takes this a step further, by converting the output current into a pulse-coded output signal, thus avoiding any analog to digital conversion at all [107].

Following review of the existing VLSI designs, it was decided that the complexity of designing and constructing such a device exceeded the scope of this project. Designing and building a discrete-component prototype potentiostat, or use of a commercial integrated circuit potentiostat were the two remaining options.

4.2 Design and Implementation

The glucose sensor uses an enzyme-coated electrode in order to achieve high specificity for glucose as opposed to other chemical species present in blood, as described in Chapter 3. This constitutes an amperometric transducer, a device that produces a current response proportional to the concentration of glucose. Furthermore, the electrode needs to be maintained at a specific voltage with relation to the reference electrode (and hence the sample solution), which requires a "potentiostat" circuit. A potentiostat was designed to strictly maintain a voltage difference between the working electrode (WE) and the reference electrode (RE). While potentiostats are common devices, commercial models are bulky, require mains power, and have a large variety of different functions. For instance, the PARSTAT 4000 from Princeton Applied Research [99] can provide currents up to 4 A, has a bandwidth of 5 MHz, can perform 53 different electrochemical techniques, and connects to a computer via a USB cable for control and results reporting. Conversely, the e-Mosquito is an inte-

grated, embedded system and its potentiostat is required to deal with currents up to 200 μA, have a maximum bandwidth in the region of 1-10 Hz, perform precisely one electrochemical technique, and report its result via an I^2C bus to a microprocessor.

A product search for an integrated system-on-a-chip (SoC) potentiostat meeting or adaptable to these requirements yielded no results. The search included major IC manufacturer websites and phone contact (Texas Instruments, Nordic Semiconductor, Analog Devices, and Agilent Technologies), as well as large-scale suppliers (DigiKey and MRO Electronic Supply Ltd.) and generic Google searches (search terms were combinations of 'Potentiostat', 'IC', 'chip', and 'electrochemistry'). This led to the decision to create a new micropotentiostat design for the e-Mosquito. Design work was undertaken to develop a simple potentiostat that fulfilled the requirements of the e-Mosquito glucose sensor.

4.2.1 Design Specification

The design requirements for the e-Mosquito potentiostat were determined to be:

- Form factor not exceeding 1.5 cm $\times$ 2.0 cm
- Potentiostatic function at a single fixed voltage that may be specified in hardware
- Bandwidth of 1-10 Hz
- Current capability of 50 μA (this sampling rate allows the mean or median of many data points to be used for a single measurement every 7-9 minutes, reducing the impact of noise on the result)
- Onboard 8-bit analog-to-digital converter
- I^2C interface

These parameters (particularly the bandwidth, current capability, and ADC resolution) were determined from the results of Chapter 3. The sequential aliquot deposition electrodes were found to give a maximum current density in the range of 250 µA/cm^2 to 400 µA/cm^2. Using an electrode surface area of 7 mm^2 (Figure 2.1) yields a maximum possible current of 28 µA from the prototype transducer. 50 µA was chosen simply to provide some margin for

error and headroom for testing purposes that may result in abnormally high currents.

4.2.2 Micropotentiostat Design

4.2.2.1 The Ideal Operational Amplifier

The majority of the circuit analyses demonstrated in this section can be most easily understood by application of the ideal operational amplifier model (Figure 4.1). An operational amplifier (opamp) is a standard piece of electronic equipment that amplifies a voltage difference: $V_{out} = A \times (V_+ - V_-)$. In order to simplify analysis of circuits containing opamps, certain assumptions about their operation are made, which lead to the 'ideal' opamp model. This is the model used for circuit analysis unless otherwise noted.

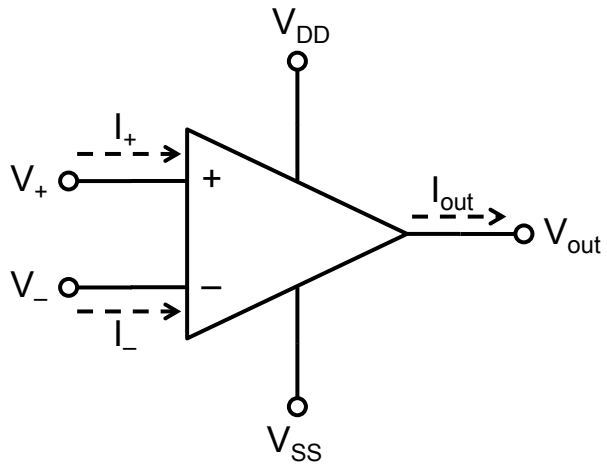

Figure 4.1: Schematic representation of an operational amplifier and the various connections and signals associated with it.

The series of assumptions underlying what constitutes an 'ideal' opamp model are:

- Infinite open-loop gain
- Infinite input impedance
- Zero output impedance
- Infinite bandwidth

Gain – The open-loop gain (A) in a real opamp is finite but very large. However, opamps are typically used in a feedback configuration where some fraction of the output (β) is subtracted from the input:

$$\begin{aligned} V_{out} &= A \cdot (V_{in} - \beta \cdot V_{out}) \\ V_{out} \cdot (1 + \beta \cdot A) &= V_{in} \cdot A \\ \frac{V_{out}}{V_{in}} &= \frac{A}{1 + \beta \cdot A} \end{aligned} \tag{4.1}$$

Equation 4.1 demonstrates that, where the open-loop gain A is much larger than 1, the closed-loop gain of the feedback loop approaches $^1/_\beta$, which is entirely dependent on the feedback gain and not on the open-loop gain at all. While real opamp gains have magnitudes in the millions or even larger, they do not have infinite gains. However, the very large value of these numbers means that the error introduced from this assumption is very small [108].

Input Impedance – Infinite input impedance implies that no current flows through either input of the opamp (denoted as $I_+ = I_- = 0$). This, in turn, means that there can be no potential difference between the two electrodes. A truly infinite input impedance is impossible in practice, but real opamps have input impedances on the order of $10^6\,\Omega$ to $10^{12}\,\Omega$. This results in extremely small input currents to the point where, in most situations, they can be discounted.

Output Impedance – An output impedance of zero means that there will be no voltage drop through the output of the opamp, which would otherwise cause significant error in the output potential. If a non-zero output impedance exists (as in real opamps), a voltage divider is formed between the output impedance and the load impedance, and some voltage drop occurs over the output impedance (Figure 4.2). This is primarily a problem with small loads, where the finite output impedance is comparatively large. The voltage supplied to the load in this situation is given below (Equation 4.2) and demonstrates that, as the load becomes much larger than the output impedance, the effect of the output impedance approaches zero.

Therefore, the zero output impedance assumption for the ideal opamp model is reasonable in cases where the load impedance is large.

$$V'_{out} = \frac{R_{load}}{R_{out} + R_{load}} \times V_{out} \tag{4.2}$$

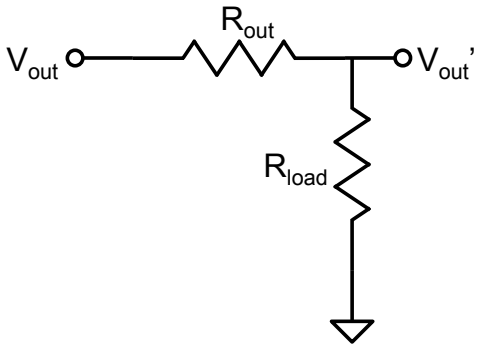

Figure 4.2: Schematic of the relationship between the output and load impedances of an opamp. As can be seen, this is essentially a simple voltage divider.

Bandwidth – By convention, bandwidth refers to the span of frequencies over which the output signal is not attenuated beyond some arbitrary level. By convention, this level is -3 dB. An ideal opamp would have an infinite bandwidth; its output would not be at all attenuated, even at infinitely high frequencies. Real opamps typically have bandwidths on the order of megahertz ($\times 10^6$) or, in high-frequency applications, up to gigahertz ($\times 10^9$). The e-Mosquito requires a bandwidth of only 1-10 Hz as the electrochemical processes underlying the sensor change relatively slowly. This bandwidth is easily attained by any common opamp and hence making this assumption is entirely reasonable for the e-Mosquito application.

4.2.2.2 Basic Design

The first electrochemical experiments involved simple two-electrode cells (Figure 4.3) that measured the current (I_{meas}) resulting from an externally applied and manually-varied voltage (V_{in}). This approach resulted in a variety of problems, including that the current was

forced to flow through the reference electrode (RE) by the electron transferring reaction at the working electrode (WE), which caused the potential between the RE and the solution (the interfacial potential) to change. This effect was called RE polarization, and it forces the interfacial potential of the WE to shift as well in order to preserve the overall potential difference between the RE and the WE (as enforced by the external circuit). Since the potential at the WE/solution interface controls the nature and rate of the reactions occurring there, these systems are inherently uncontrollable for anything but the simplest experiments.

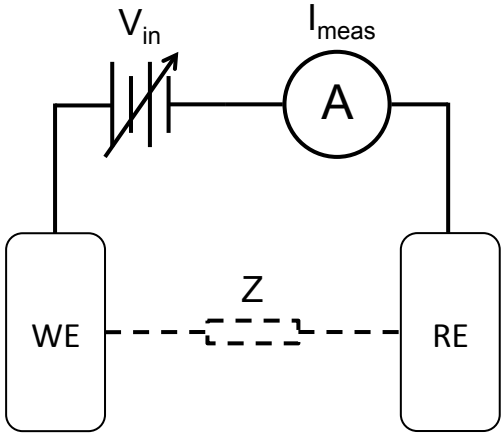

Figure 4.3: Simple representation of a two-electrode electrochemical experiment. The voltage, V_{in}, maintains the working electrode (WE) at a particular potential relative to the reference electrode (RE) and is quite commonly varied in time. The resulting current is measured (I_{meas}) and plotted against the potential. The electrochemical solution in which the electrodes are immersed can be conceptualized as a non-linear complex impedance.

The shortcomings of the two-electrode system can be largely corrected by using a three-electrode potentiostat system, first invented in 1942 by Hickling [109]. The potential-holding and current-delivering duties that were both performed by the RE in the two-electrode configuration were now split into a separate RE and a counter (or auxiliary) electrode (CE). The RE now delivers ideally no current (though, in reality, there must be a very small current in order to measure and control the WE potential). The CE is responsible for supplying current into the cell to allow the voltage conditions of the RE and WE to be maintained.

Bard and Faulkner provide an excellent reference for potentiostat design in "Electrochemical Methods: Fundamentals and Applications" and their basic adder potentiostat design is reproduced in Figure 4.4. This formed the basis of the potentiostat design used in the e-Mosquito [110].

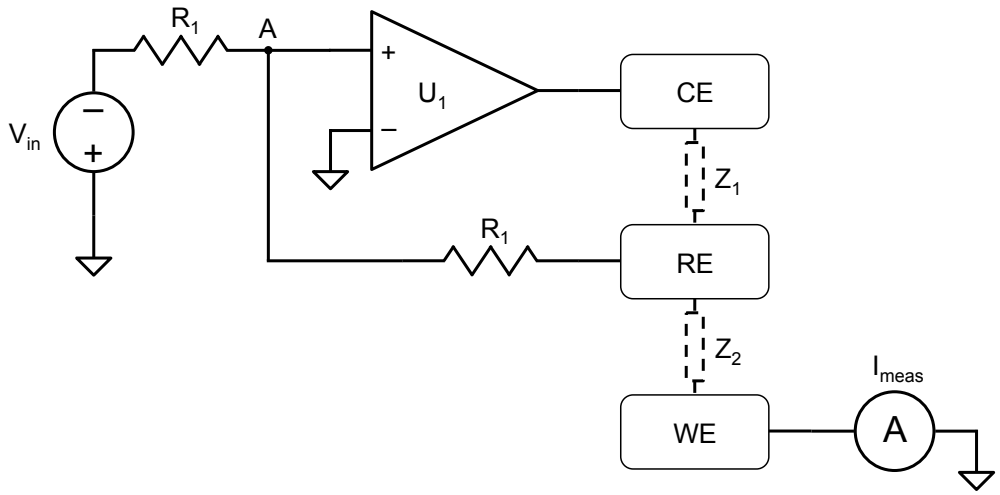

Figure 4.4: Simple scheme of a three-electrode potentiostat. The operational amplifer causes a current to flow out of the counter electrode (CE) that maintains the specific potential V_{in} between the reference electrode (RE) and the working electrode (WE) at ground. The impedance of the interfaces and the bulk solution under test are represented by Z1 and Z2.

The potentiostat design shown in Figure 4.4 acts as a simple feedback control loop. Kirchoff's current law, applied at the point labeled 'A', shows that the current through the reference electrode must have the same magnitude as the current through the voltage source: $-I_{RE} = I_{in}$. Since A is at virtual ground (per the ideal opamp model), application of Ohm's Law allowed determination of the reference electode potential, as shown in Equation 4.4.

$$I_{RE} = \frac{V_{RE}}{R_1}$$
$$I_{in} = \frac{V_{in}}{R_1}$$

$$-I_{RE} = I_{in} \tag{4.3}$$
$$-\frac{V_{RE}}{R_1} = \frac{I_{in}}{R_1}$$
$$V_{RE} = -V_{in} \tag{4.4}$$

This result indicates that the cell potential can be easily chosen, as the RE will be held at $-V_{in}$ relative to circuit ground. Since the working electrode is at circuit ground (assuming an ideal ammeter), the potential of the working electrode relative to the reference electrode is $+V_{in}$.

Unfortunately, this initial design had a fundamental flaw, which was that a non-insignificant current is permitted to flow through the reference electrode via the voltage source, which, as noted above, caused polarization of the RE. Polarization of the RE would result in an unknown interface potential of the working electrode. This flaw was remedied in a straightforward fashion with the addition of a buffer in line with the RE (Figure 4.5) so that the current is supplied from the power supply via the buffer opamp (U2) instead of through the RE. With the opamp (U2) configured as a simple passthrough buffer with a gain of 1, there was no impact on the voltages at the reference electrode or at point A (Figure 4.4).

This configuration was the nearly-final design for the potentiostat, but was missing a key component. At this point, the circuit required an 'ideal' ammeter that would be capable of measuring the WE current without incurring any voltage drop. The simple, classical manner of measuring current in a microprocessor circuit is by running the current through a known resistance and measuring the resulting voltage. If the resistance is known, the current can

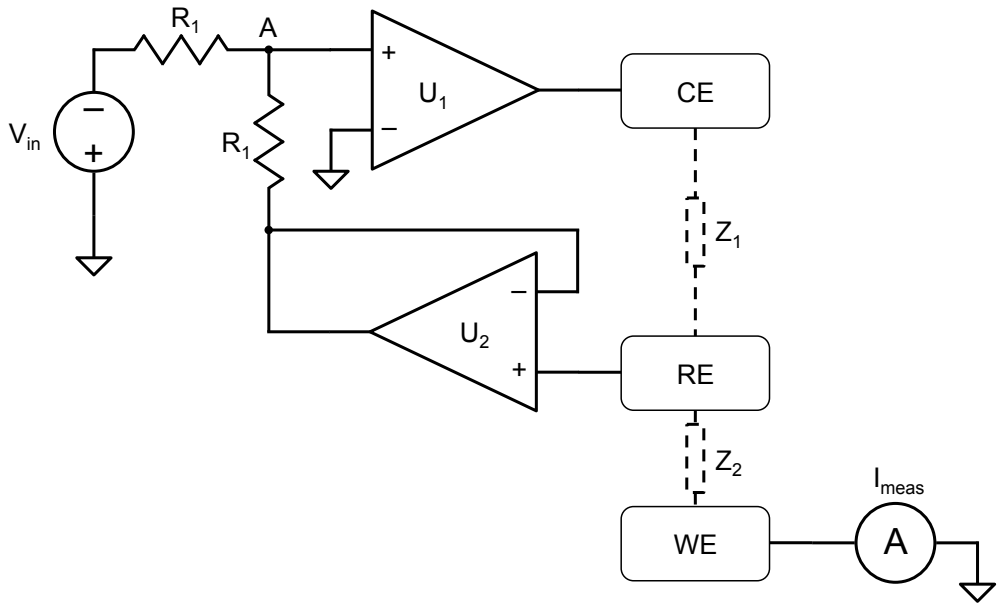

Figure 4.5: Buffered version of Figure 4.4. The feedback buffer is important to ensure that the current flow out of node RE is effectively zero.

easily be calculated from the voltage drop by using Ohm's law ($V = I \cdot R$). This is a simple and easily understood method, but, unfortunately, was unusable in this situation due to the placement of the measuring resistor. This resistor would need to be between the WE and circuit ground, and as a result of the voltage drop across this resistor, the voltage of the WE relative to the RE would have been biased. This is, as has been mentioned before, suboptimal, as the interfacial potential of the WE influences the electrochemical reactions that occur there and must be exactly controlled and reproducible.

The solution to this problem lies in a small circuit called a transimpedance amplifier. This circuit converts a current into a voltage, much like a pure resistance, but it does so in a manner that allows the WE to stay at (virtual) ground potential, i.e., it does not bias the WE. Details of the circuit are elucidated in Appendix B, and Figure 4.6 shows the completed potentiostat circuit with the transimpedance amplifier in place to measure the output current from the WE. This was the final circuit design used in the e-Mosquito prototype. The output of interest is V_{meas}, which is proportional to the current conducted

through the WE, as shown by Equation 4.5.

$$V_{meas} = -I_{WE} \cdot R \tag{4.5}$$

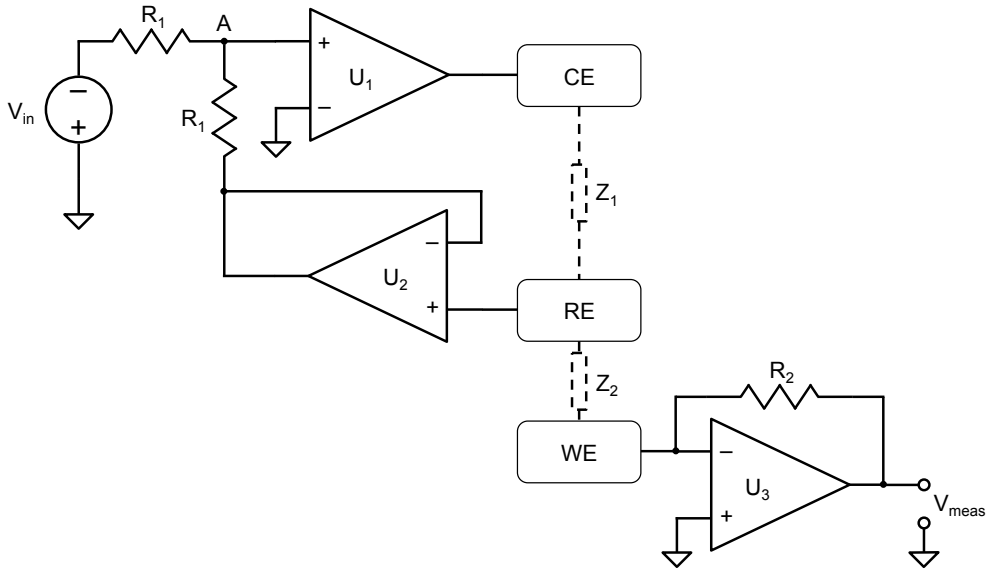

Figure 4.6: Final circuit design for the e-Mosquito potentiostat. A transimpedance amplifier is used as a nearly-ideal ammeter attached to the working electrode.

4.2.2.3 Power Supply

Equation 4.5 shows that, for a positive conventional current flowing from the working electrode, the resulting voltage is negative with respect to ground. Furthermore, the opamps that are used in the design of this circuit also require a bipolar power supply. Unfortunately, the prototype e-Mosquito currently only supplies a monopolar +3 V supply. Therefore, design was undertaken on a small-scale bipolar power supply that would supply ± 2.5 V and a virtual ground (VGND).

The first step in designing the power supply was to convert the +3 V DC input power supplied by the e-Mosquito's watch batteries to a +5 V DC output that could provide the

full 5 V range needed to supply a range of -2.5 V to +2.5 V. While voltage conversion is typically done on a large scale with AC power and transformers, small scale integrated chip (IC) solutions are available to perform DC-to-DC voltage step-up operations. One such IC is the MAX856 by Maxim Integrated [111]. This IC provides an output voltage of either +3 V DC or +5 V DC (selectable by the supporting circuitry) from an input voltage of between +0.8 V DC to +6.0 V DC with a current efficiency of 85 % [111]. The maximum current provided while maintaining approximately 85 % efficiency is 100 mA. Hence, this IC met the requirements for this low-current application. The datasheet also provided a 'typical application circuit' for ideal operation. The MAX856 was used in the e-Mosquito power supply design, as seen in Figure 4.7

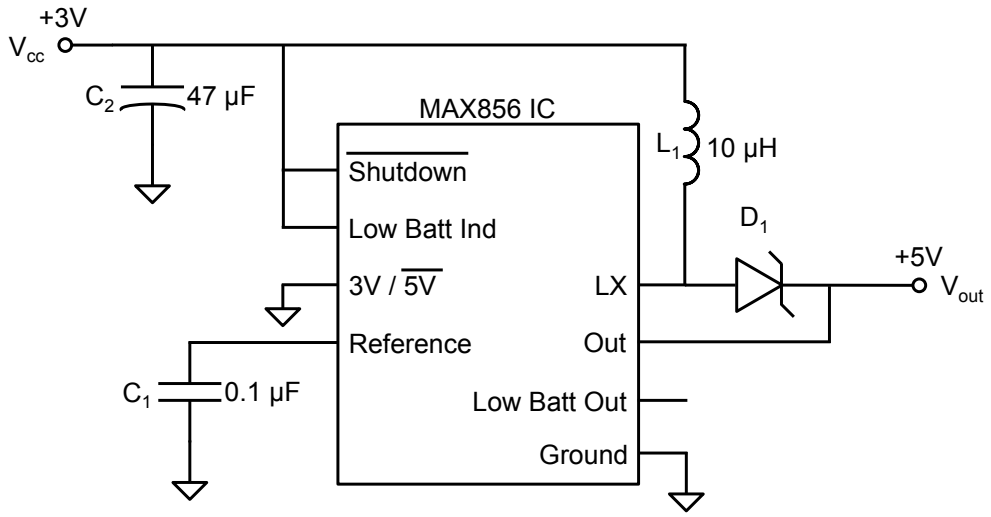

Figure 4.7: Application/implementation circuit for DC-to-DC voltage step up used to convert +3V DC to +5V DC using the MAX856 IC for high-frequency voltage conversion.

The second design challenge was to convert a unipolar +5 V DC supply into the bipolar ±2.5 V and VGND supply required. The simplest approach to this would be to use a simple resistive voltage divider to produce a potential of +2.5 V DC and use this as the VGND (Figure 4.8). This would have resulted in the original GND potential becoming -2.5 V relative

to the new VGND, and the original +5 V becoming +2.5 V relative to the new VGND. In practice, however, a problem occured when the load impedance was not very large relative to the resistances in the voltage divider, as the load was (by necessity) connected in parallel with the second dividing resistor. This resulted in alteration of the equivalent resistance of the bottom half of the voltage divider, which, in turn, led to a change in the VGND potential that was provided by the voltage divider.

The solution was to use an active voltage regulator to provide the VGND. These circuits exist as commercial ICs, called "rail-splitters", that can actively maintain a constant potential halfway between the positive and ground rails of a unipolar power supply. In the case of the e-Mosquito, the IC selected was the TLE2426 'rail splitter precision virtual ground', produced by Texas Instruments [112]. This IC guarantees an output potential equal to half of the input potential over a very wide range of load impedances, thus providing a nearly perfect VGND potential. The maximum current that can be sourced/sunk by the IC is 20 mA, which was again in excess of the low current requirements of the potentiostat circuit (which operates on the order of μA).

The complete potentiostat power supply appears in Figure 4.9. The two capacitors, the inductor, and the diode function to provide power conditioning, smoothing, and load matching to the DC-to-DC step-up transformer MAX856.

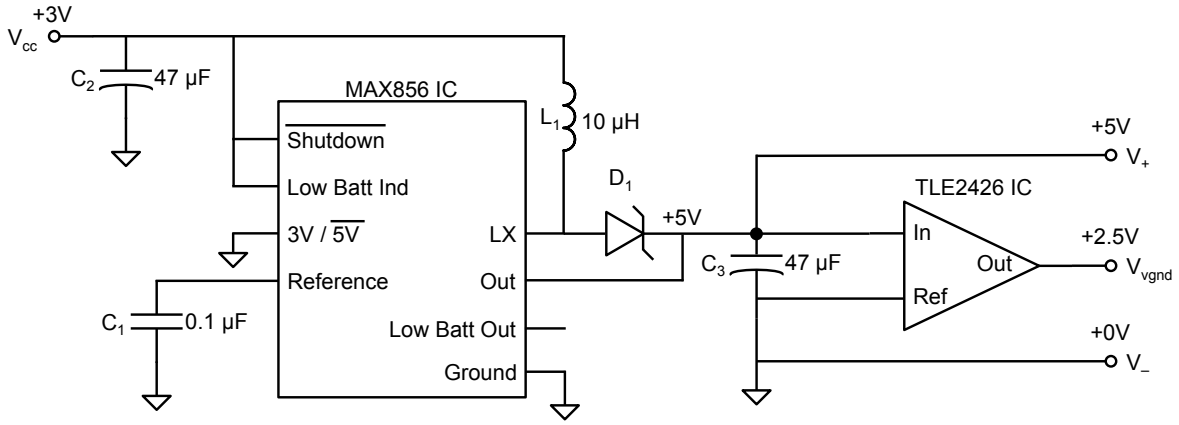

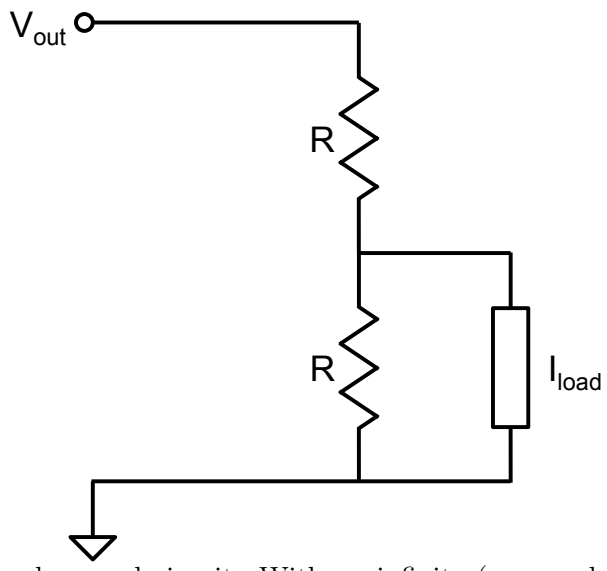

Figure 4.8: Resistive virtual ground circuit. With an infinite (or very large) load impedance, the virtual ground is approximately centred between the two rails. However, with a non-infinite load, the virtual ground will deviate from its correct value.

Figure 4.9: Final circuit design of the e-Mosquito potentiostat's power supply, including the TLE2426 railsplitter.

4.2.2.4 Analog-to-Digital Conversion and I^2C Interface

The e-Mosquito measures the current that passes through the working electrode (WE). As detailed in the previous section, this is converted into a proportional voltage with a transimpedance amplifier. This voltage must then be converted into a digital code that can be processed by the microprocessor and its associated software.

Analog-to-digital conversion (ADC) is built into many microprocessors, including the Texas Instruments MSP430F5438, which was used in the existing e-Mosquito prototype. This processor provides 14 analog-to-digital inputs built-in, each of which features 12 bits of digital resolution. However, an external ADC was used as opposed to the built-in ADCs in order to maintain the modularity of the prototype. The entire sensor system could be swapped out at a later date, or attached to a different processor/prototype. The ADC

chip, potentiostat, and potentiostat power supply all share a single PCB, and the ADC communicates with the prototype main processor via the industry I^{2}C standard (Figure 4.10).

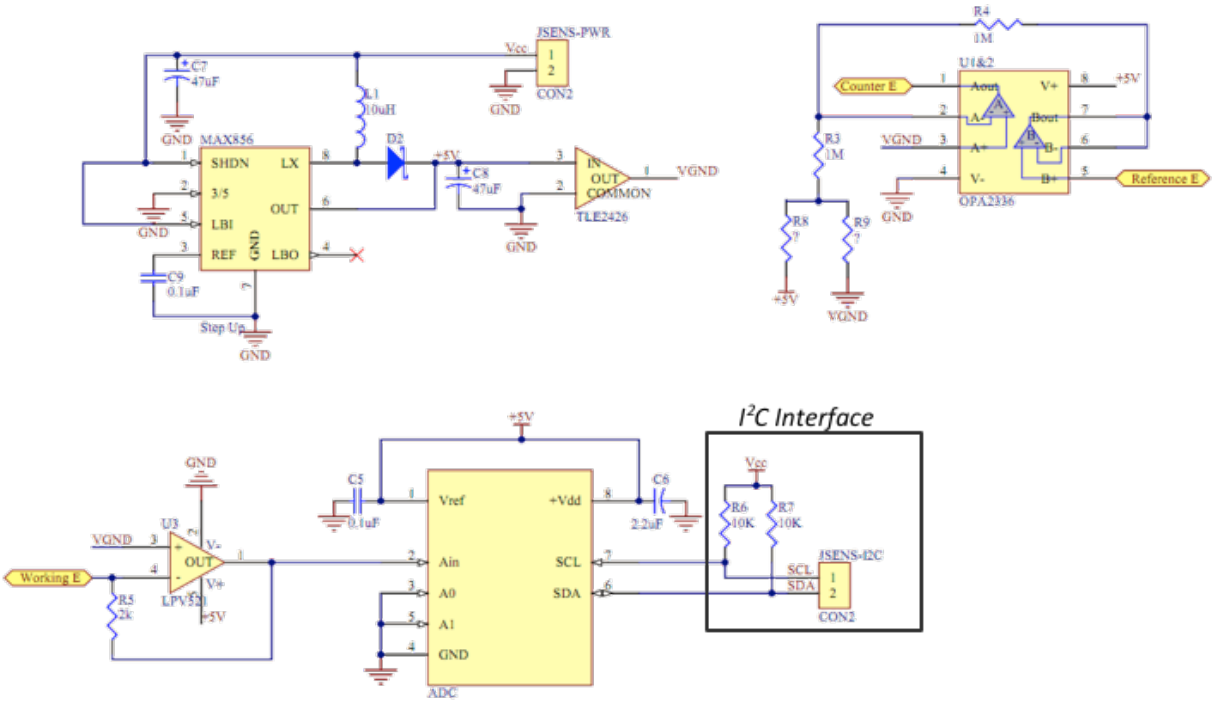

Figure 4.10: Final circuit design for the e-Mosquito potentiostat. A transimpedance amplifier was used as a nearly-ideal ammeter attached to the working electrode.

The ADC is required to be capable of only 10 samples per second by the prototype software, and this could likely be lowered in future iterations. As such, most ADC integrated circuits with sufficient bit-resolution and an I^{2}C interface may be used.

Bit resolution was the other parameter of interest in selecting an ADC and was a more involved process, as it directly impacts the error and precision of the attainable glucose measurement. The range of blood glucose levels that are considered 'physiologic' in a healthy individual are approximately 3.0 mM to 9.0 mM [113], but the decision was made to design the sensor to operate over the range of 0.0 mM to 20.0 mM, as this is the "clinically-relevant

range" of blood glucose concentrations [66]. For values above this range, the precise value is likely less important, as medical attention should be sought anyway.

Quantization Error – Quantization error is the error that results from discretization of the input signal. Analog signals, such as the current produced at the WE, are continuous and can assume an infinite number of different values. Conversely, digital data are discrete and limited to particular 'levels'. For instance, an 8-bit digital number can assume $2^8 = 256$ different values, or measured levels. Since the sensor was limited to the clinically-relevant range of glucose (Chapter 3), there must be an adequate number of distinct digital levels available to provide a sufficiently precise representation of the reported result.

In our centre, blood glucose is typically reported in units of $^{\text{mmol}}/_{\text{L}}$ to a precision of one decimal place (i.e., $5.8\,^{\text{mmol}}/_{\text{L}}$). This precision requirement was therefore adopted for the e-Mosquito. This results in a requirement for at least 200 possible digital levels in the output, which is adequately represented by an 8-bit number. This is the simplest estimation of the precision required of the ADC and is a reasonable method of determining quantization resolution in a prototype setting.

The magnitude of the quantization error is approximately $\frac{1}{2} \cdot LSB$, where LSB is the magnitude of the least-significant bit. In the case of an 8-bit ADC spanning a range of 0.0 mM to 20.0 mM, this works out to $0.08\,^{\text{mM}}/_{\text{LSB}}$. Hence, the maximum error arising from the quantization of the signal is $\frac{1}{2} \times 0.08\text{mM} = 0.04$ mM. While this level of error is below our desired accuracy of 0.1 mM, it is large enough such that the cumulative error of the sensor system may exceed the desired accuracy. In order to provide a margin of error and to provide future-proofing, a 12-bit ADC was used.

I²C Standard – This is an industry standard two-wire communication protocol that is supported by a wide variety of electronic digital devices. Among these are a large number of ADCs and the TI MSP430F5438 used in the existing e-Mosquito prototype. As a result of the simplicity of connection (requiring only two pullup resistors, one on each of the two communication lines SCL and SDA), and the fact that it is already provided by the existing

prototype, I^2C was selected for communication between the glucose sensor ADC and the e-Mosquito. The I^2C bus carries commands to the ADC to cause it to sample output voltage of the potentiostat (proportional to the output current of the working electrode), and the ADC returns the result as a standard binary number to the microprocessor on the e-Mosquito prototype.

4.2.3 Component Selection

Component selection for the e-Mosquito device consisted of a multifactorial approach that had to balance several separate sets of requirements for each part. The most obvious of these is the performance requirements for the application at hand. Earlier discussion elucidated why the requirements for the device are, in general, fairly low: the application is relatively low-frequency, low-voltage, and tolerant of error. As a portable application, power-management is a very important consideration, and power consumption of all components was an important factor in their selection. Finally, decisions were made based on what was both easily available and what had an easy-to-use form factor (i.e., dual inline package/through-hole parts were preferred to surface-mount chips, which were preferred to pin grid array chips).

Selection of integrated chip components was a far more involved process, but some consideration of the passive components was required as well. The main passive component issue concerns the tolerances of key resistors in the design. Resistors typically have a tolerance of 5 %, which is quite sufficient for many applications. However, resistors in critical areas of the potentiostat require higher tolerances. Specifically, the resistor in the feedback component of the transimpedance amplifier will introduce inter-device error if its tolerance is not tightly controlled. The other part of the potentiostat that is highly sensitive to error is the input voltage biasing circuit. Since the electrochemical reaction kinetics are very sensitive to the electrical potential of the electrodes, strict control of this parameter is essential. The bias potential of the system is set by a simple two-resistor voltage divider and hence the accuracy

of these two resistors is paramount to having predictable reaction kinetics, and hence predictable transducer output. These high-stakes components were sourced to have a tolerance of 1 %. All other passive components had standard 5 % tolerances. A full list of components is available in Appendix D.

Component selection allowed the design of a physical printed circuit board (PCB). This involved placement of the various electrical components and routing of electrical connections between them. The resulting board design was exported in the industry-standard Gerber® digital file format and manufactured by AP Circuits® in Calgary, AB. The general layout of the PCB is shown in Figure 4.11.

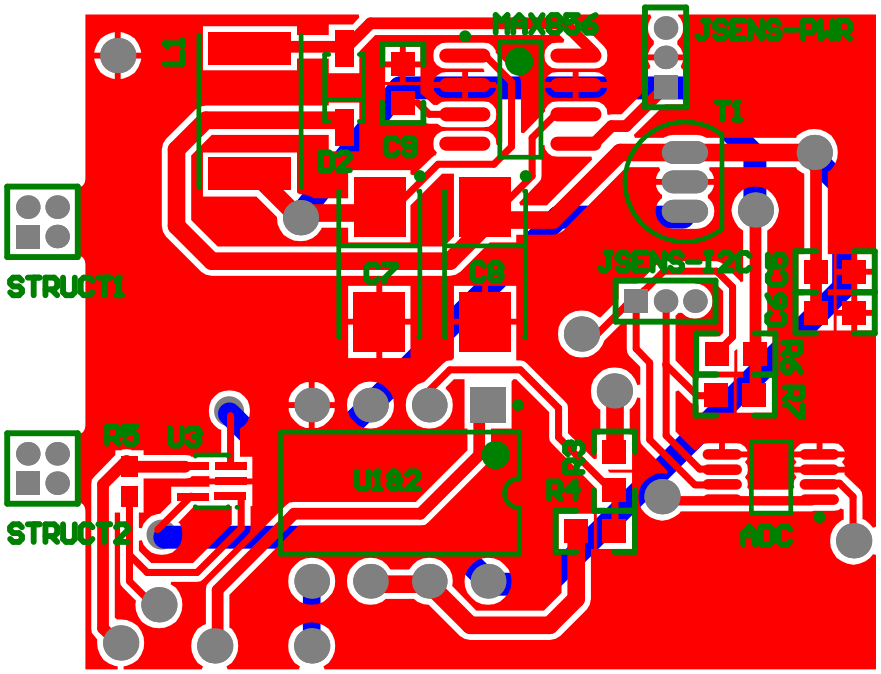

Figure 4.11: CAD layout of the e-Mosquito potentiostat PCB. Red indicates areas of the top layer where the copper remains, while Blue indicates areas of the bottom layer that are covered in copper.

4.2.4 Concentration Calculation

The final step in measuring the glucose concentration of a blood sample was to convert the measured voltage into a glucose concentration that can be displayed on the device or transmitted to another device. The first step of this process was to convert the measured voltage back into its corresponding electrical current (the current passing through the WE/solution interface). As outlined in Appendix B, the transimpedance amplifier used to convert the current into a voltage (to be measured by the ADC) simply performs the transformation: $V_{meas} = I_{WE} \cdot R$, where R is the feedback resistor around the operational amplifier. Therefore, the first step to retrieve the electrical current through the working electrode consisted of calculating the result of the inverse formula in the microprocessor: $I_{meas} = \frac{V_{out}}{R}$.[1]

The next step in calculating a final measured glucose concentration involved applying the *inverse* Michaelis-Menten equation. Since the reaction is well-modelled by Michaelis-Menten kinetics (Sections 3.1.5, 3.2.5, and 3.3.5), the output current for a given glucose concentration was modelled as (Equation 4.6):

$$I_{meas} = \frac{I_{max} \cdot [Glucose]}{K_m + [Glucose]} \tag{4.6}$$

It was then trivial to recover $[Glucose]$ from I_{meas} by applying the inverse form of the model (Equation 4.7):

$$[Glucose] = \frac{Imeas \cdot K_m}{I_{max} - I_{meas}} \tag{4.7}$$

I_{max} and K_m are, as mentioned in Section 1.3, properties of the physical sensor itself. Individual sensors will have variation in their individual parameters, but a single use sensor cannot be calibrated on a per-sensor basis. Therefore, calibration parameters were derived

[1] As the TI MSP430F5438 microprocessor does not have a hardware floating-point unit, this calculation is emulated in software using the IEEE 754 standard. While slower, only a small number of calculations need to be performed and the performance penalty is acceptable for any user applications.

as the mean or median values of I_{max} and K_m for the current batch of sensors. If the programmed calibration parameters are termed I'_{max} and K'_m, then the actual equation implemented by the prototype software is (Equation 4.8):

$$[Glucose] = \frac{Imeas \cdot K'_m}{I'_{max} - I_{meas}} \tag{4.8}$$

Thus the differences $(I'_{max} - I_{max})$ and $(K'_m - K_m)$ (the calibration errors) results in errors of the final output glucose measurements. Large amounts of the output error noted in Chapter 3 were attributed to the lack of a reproducible transducer manufacturing processes. More details of calibration error and its relationship to the final transducer error are found in Appendix A.

4.3 Testing and Validation

4.3.1 Potentiostat

The potentiostat was originally tested in software by using a SPICE simulation of the design connected to a standardized test cell, as shown in Figure 4.12. The potential input to the potentiostat (this is the electrical potential that is then maintained between the reference and working electrodes) was connected to a simulated triangular wave. This caused the potentiostat to function as a swept-potential potentiostat. The expected output for this test cell was then calculated according to the ideal constraints expected of a potentiostat in operation (Figure 4.13).

Following verification of the simulated potentiostat, the physical potentiostat was tested using a physical-PCB version of the simplified Randles' test cell. The simulated process was then repeated in hardware, and the potentiostat input voltage was connected to a waveform generator that was producing a triangular wave. The resulting cyclic voltammetry (CV) plot was then compared to the simulated output and found to match to within the tolerances

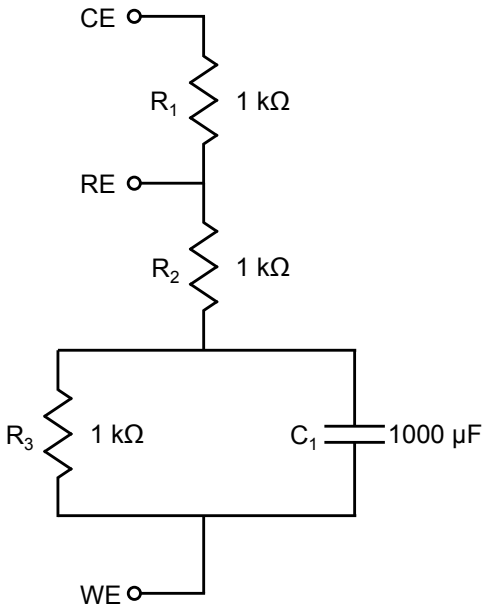

Figure 4.12: The simulated test cell used to validate the potentiostat design. This test cell is known as the "simplified Randles' cell" and has a known and characteristic electrochemical response.

of the components used in the test cell (Figure 4.14). On the basis of these results it was decided that the potentiostat functioned adequately for this application.

Testing and validation of the I^2C communication system was implicit in the ability to read results from the test cell. Since the I^2C standard is well known and uses standard third-party libraries for communication, the only testing performed on it was to debug the client-side software until communication was established.

4.3.2 Combined Counter and Reference Electrode

Many groups [114, 93, 69, 1] have used iridium oxide (IrOx) as a pseudo-reference electrode, especially in pH sensing and biological applications. This is due to its reference potential stability and resistance to polarization [114, 93]. It is also considered to be a biocompatible material [69, 1] which makes it desirable for use in the e-Mosquito, as the blood sample is briefly in contiguous contact with both the sensor electrodes and the patient's circulating blood. IrOx is also non-soluble, as long as it is properly bound to the electrode substrate so

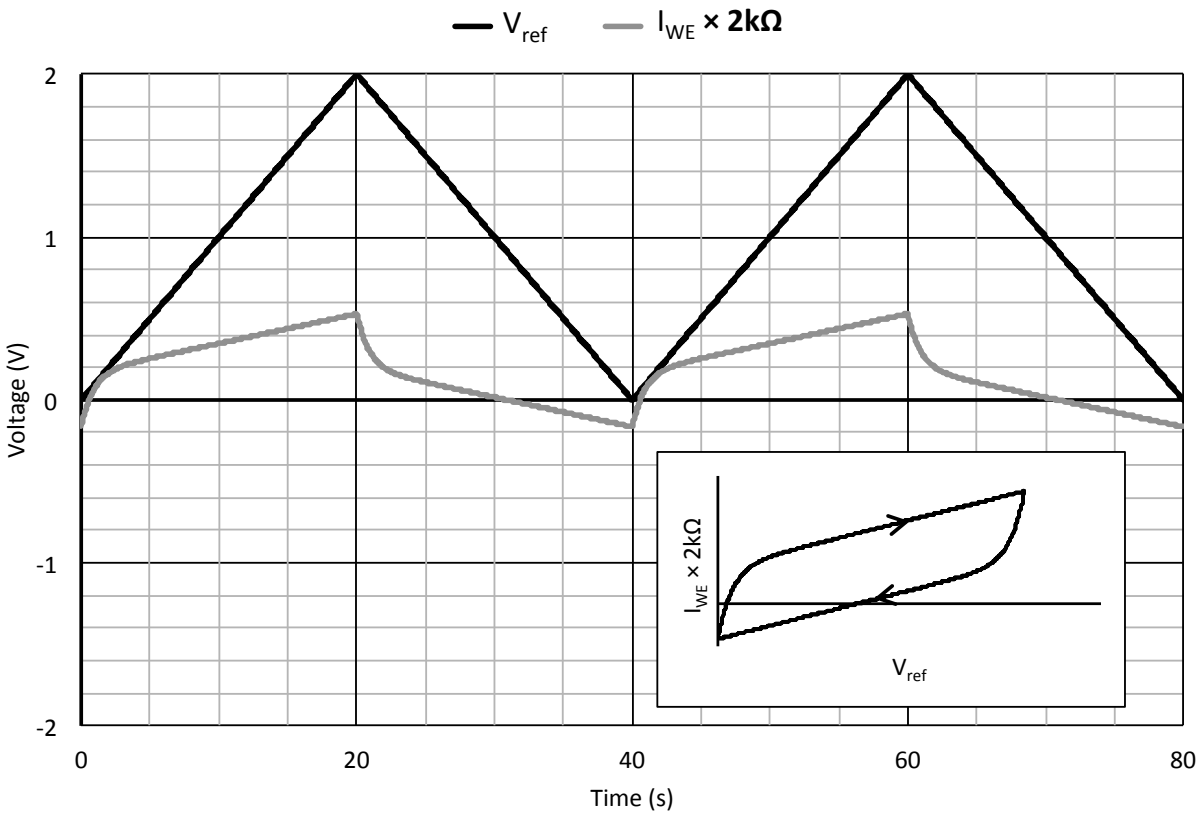

Figure 4.13: Expected result of a cyclic voltammetry experiment performed on the simplified Randles' cell (Figure 4.12). This was calculated from the known constraints imposed on a cell by an ideal potentiostat. The inset shows the same data formatted in the classical cyclic voltammagram format.

that it will not dissolve and diffuse into the patient's systemic circulation.

Current-generation glucose sensors use both three-electrode and two-electrode configurations in the test strips [115]. For example, the Accu-Chek® system by Roche Diagnostics uses a two-electrode system in their commercial sensor system [116]. It is clearly feasible to use such a system and attain sufficient accuracy and precision, and this approach was used for testing of the integrated system. Due to the existing use of IrOx in the working electrode, use of a combined counter/reference electrode made of this material has the potential to simplify the design of the sensor. This technique was used in order to simplify

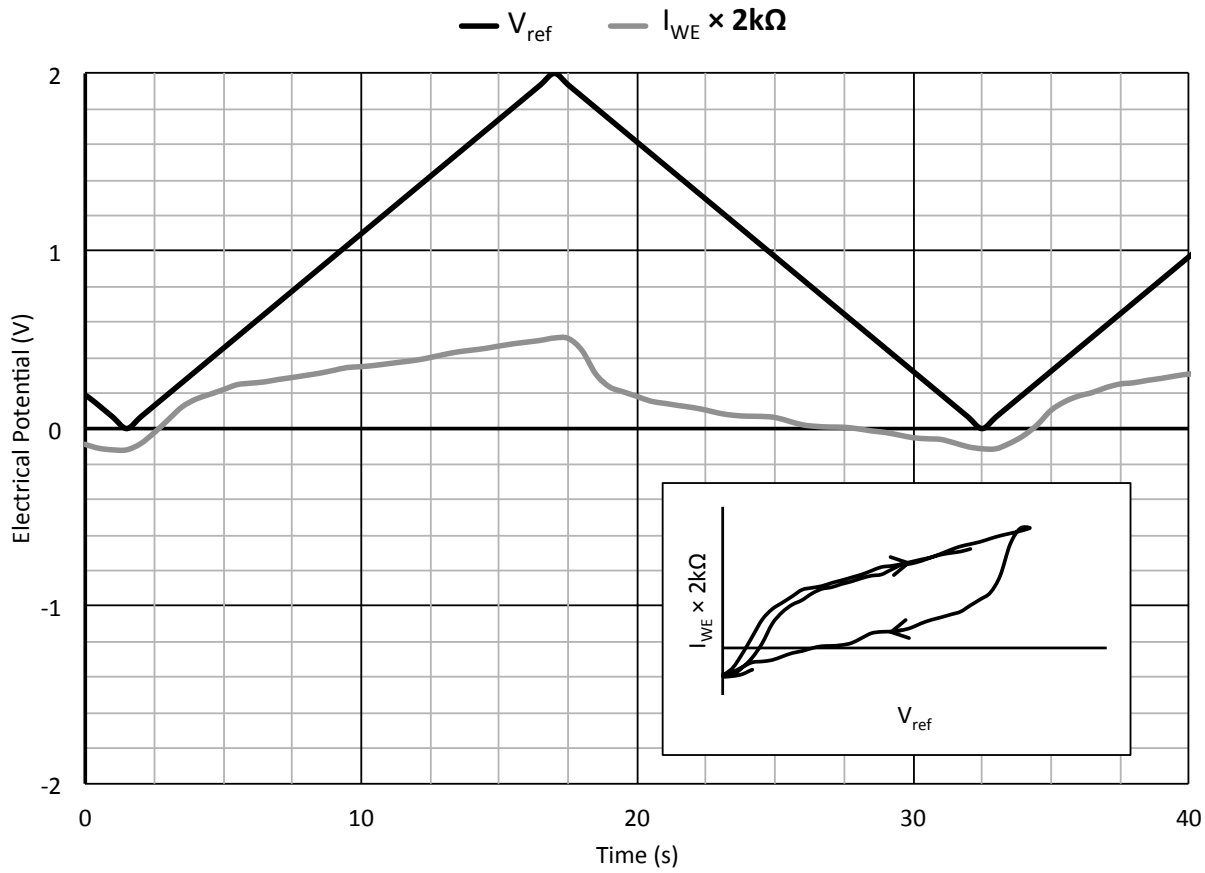

Figure 4.14: Recorded trace of the physical prototype potentiostat as connected to a physical simplified Randles' cell. The inset shows the data formatted as a cyclic voltammagram (CV) demonstrating the repeatability of the response. This figure shows that the physical potentiostat behaves in the expected manner.

testing of the sensor electronics, as it resulted in easier-to-manufacture electrodes for this testing. Furthermore, implementing two electrodes instead of three in a constrained surface area resulted in larger electrodes with theoretically larger output currents.

Electrodes were prepared according to the procedure for sequentially aliquoted transducers in Chapter 2, but were not coated with the active GOx solution or the Nafion® . This resulted in bare IrOx on a gold substrate which was stable when immersed in aqueous solutions for the typical duration of measurements made using the electrode (50 s).

In order to test the integrated system, small-scale 2-electrode transducers (Section 4.3.2) were manufactured on poly(methyl-methacrylate) (PMMA) by photolithography at the university lab, following the design schematic in Figure 2.1. The oxidation of the combined RE/CE was accomplished in the same manner as the working electrode: by electrochemical oxidation of the aliquotted Ir sol. In order to expedite this step of the manufacturing process, the far right-hand side of the electrode mask contains an electrical connection between the working electrode and the combined RE/CE. This allowed the electrochemical oxidation of the Ir metal to proceed for both the WE and combined RE/CE in a single step. Following manufacture, the right-hand side of the electrode platform was detached, obliterating the direct electrical connection between the two electrodes. This electrode is shown in Figure 4.15 prior to use (i.e., prior to the cleaning and deposition of Ir, GOx, and Nafion® .

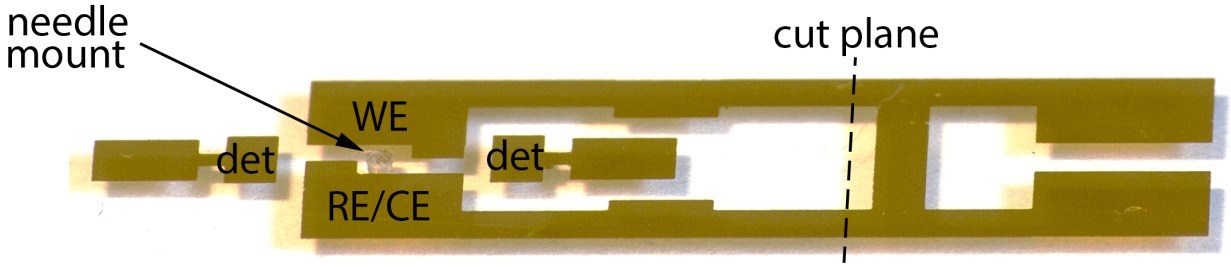

Figure 4.15: Photo of an unused micro-transducer. The image includes markup indicating the working electrode (WE), the combined reference and counter electrode (RE/CE), the sample detection electrodes (det), the mounting hole for the microneedle, and the cut plane where the actual transducer (left of dashed line) is separated from the support portion following electrochemical oxidation of the iridium.

4.3.3 Integrated System

Following validation of the potentiostat circuit itself, the entire integrated sensor system required testing and validation. For the purposes of the prototype, it was decided that demonstrating a measurable response to the glucose concentration present at the electrodes

was sufficient to prove that the sensor electronics function (essentially demonstrating a dose-response relationship). This response curve should match the predicted and previously observed Michaelis-Menten model (Chapter 3). Inter-electrode variability and response reproducibility was also of interest, but is a transducer manufacturing problem that does not impact the feasibility or design of the sensor electronics.

The test itself was performed in the same manner as the bench-top transducer tests in Chapter 3. The electrodes were immersed in a PBSS and known aliquots of glucose were added. The resulting current output of the sensor system was measured by the micropotentiostat and plotted against the calculated glucose concentration of the test solution. The readout provided by the sensor system was also plotted. The results of this test for 3 electrodes (A-C) are shown in Figure 4.16.

Given the close adherence of the sample points to a Michaelis-Menten model, the potentiostat is considered validated in terms of performance. There is noted variability reappearing in the resulting transducers despite use of the sequential aliquot deposition technique that performed best in Chapter 3 (Section 3.3.4). This could be a result of a number of factors, including the use of the plastic polymer platform for the transducer, unexpected instability of the two-electrode system, or unanticipated variability of the performance of IrOx combined RE/CEs. These errors do not invalidate the fact that the potentiostat is demonstrated to work as expected, and mitigation of this variability is beyond the scope of this project.

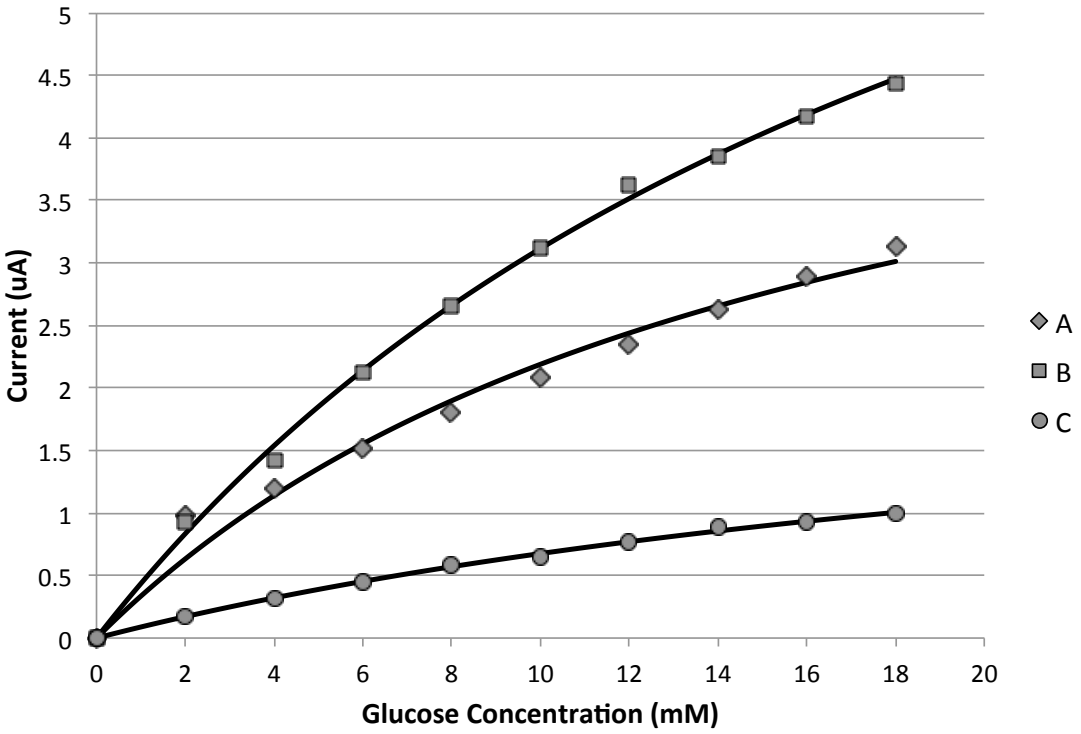

Figure 4.16: The results from three tests of the complete system. This was performed using the 2-electrode micro-transducer design in conjunction with the micropotentiostat described in this chapter. The test was performed in PBSS under air (no argon was used to deoxygenate the test solution) and without stirring of the test cell solution. The average measured current for each step was computed by the e-Mosquito microprocessor and communicated to the control PC via the wireless communication system onboard the prototype.

4.4 Summary

In this chapter, the design process and resulting micropotentiostat was described. The supporting electronics, such as the bipolar power supply, ADC, and I^2C communications bus, were also designed and implemented. The resulting electronic package was manufactured on a custom printed circuit board using through-hold components, and was demonstrated to function as expected for a potentiostat.

Three 2-electrode transducers were constructed on PMMA using the sequential aliquot deposition method described in Section 3.3, and three of these electrodes were tested us-

ing the prototype micropotentiostat. The results showed the expected Michaelis-Menten behaviour and had output currents in the expected range, demonstrating the feasibility of the micropotentiostat. Unfortunately, extreme variability between the tested electrodes was observed. Since multiple factors had changed between the formal testing of sequentially aliquotted electrodes and the micropotentiostat testing experiment, it was impossible to determine exactly what caused this large variability. However the fact that all measured points were very accurately fitted by the non-linear Michaelis-Menten regression fit indicates that the micropotentiostat is functioning and measuring as expected.

Chapter 5

Conclusion

This thesis presents the complete development, design, implementation, and testing of a proof-of-concept prototype glucose sensor system. This sensor is novel in terms of its chemical functioning, and was successfully integrated with the existing e-Mosquito prototype.

The first section of the project consisted of testing and characterizing the response of the transducer element and its associated nanoparticle and enzyme films. Three distinct methods of transducer construction were attempted. The first was named 'electrophoretic deposition' (Section 3.1) and involved using electrophoretic techniques to electrically deposit glucose oxidase (GOx) enzyme on to the electrode surface, which had been previously prepared with an iridium oxide (IrOx) nanoparticle film. The second was termed 'aliquot deposition' (Section 3.2) and involved mechanical deposition of a solution containing iridium (Ir), GOx, and Nafion® on to a gold (Au) surface in a single step. This was followed by a period of ambient drying, and subsequent electrochemical oxidation of the Ir to IrOx. The final method was 'sequential aliquot deposition' (Section 3.3), and was designed to address concerns with the random aggregation of Ir on the Au surface that was seen with the aliquot deposition method. The ethanolic Ir sol was deposited first and allowed to dry, followed by electrochemical oxidation of the Ir to IrOx. The aqueous GOx and Nafion® solution was then mechanically applied in a separate step and allowed to dry as well.

The electrophoretic deposition technique showed relatively small current densities, with i_{max} <60 µA/cm^2, and large variability between individual transducers. The mean percent error for these electrodes was only -22 %, but the standard deviation of the percent error was

49 %. The values of K_m were relatively consistent, though this is expected as it represents more of an intrinsic property of the enzyme itself (the 'affinity' of the enzyme for substrate) rather than an extrinsic property of the transducer as in the case of i_{max}. The process also required large quantities of GOx enzyme, and so was abandoned early on in favour of aliquot deposition techniques.

The aliquot deposition technique resulted in larger currents than the electrophoretic method (mean i_{max} of 220 µA/cm^2) but the largest variability between transducers of any method tested. The mean percent error was 3.0 %, but the standard deviation of the percent error was 150 %. This made the aliquot deposition technique clearly unacceptable for clinical use.

The sequential aliquot deposition technique resulted in transducers that produced large currents (mean i_{max} of 280 µA/cm^2) and low inter-electrode variability that is within the clinically-acceptable range per the Clarke error grid (Section 3.5.1). These electrodes had a mean percent error of −2.5 % and standard deviation of percent error of 6.6 %. As a result of these very favourable results, this method was selected for the e-Mosquito prototype glucose sensor, and the subsequent micropotentiostat design was based around the requirements and electrical characteristics of this form of sensor.

Proving the validity of Michaelis-Menten enzyme kinetics as a model that could be fitted to the measured electrode glucose response data was also undertaken. From a qualitative perspective, the glucose response curves that were generated closely resembled Michaelis-Menten plots, and appeared to fit the measured data points extremely closely. Quantitative verification of this fact involved calculation of the normalized RMS error (NRMSE) for each electrode. All electrodes had NRMSEs that were remarkably low, with an average normalized RMS error of 0.92 % and a standard deviation of error of 0.56 %. This demonstrates a remarkably good fit, especially considering that the signal amplitude is on the order of microamperes. The conclusion drawn was that the Michaelis-Menten model is an accurate estimator for the physical enzyme system in all three construction techniques.

Some variation was noted in the magnitude of the cyclic voltammetry (CV) currents measured during the electrochemical oxidation of Ir. In order to ensure that this was not causing any of the variability and error in the results, interactions were assessed using the Pearson's correlation coefficient and the Student's t-test between the maximum anodic and maximum cathodic currents with the Michaelis-Menten parameters i_{max} and K_m. No statistically significant correlations or interactions were detected with a significance threshold of $\alpha = 0.05$.

Following characterization of the sensor chemistry, efforts were undertaken to miniaturize the system of three discreet, large-scale electrodes into an integrated 2- or 3-electrode sampling platforms. These platforms integrated the blood detection electrodes, glucose measurement electrodes, microneedle, sample well, and structural support onto a single unit.

The design and testing of a small-scale prototype potentiostat was performed for particular application in the e-Mosquito. The circuit was initially simulated using the PSPICE software suite, and was then built using discreet components on a PCB. Testing demonstrated that the performance of the physical prototype matched the performance of an ideal potentiostat, and the device was integrated with the existing e-Mosquito prototype. Communication with the existing e-prototype was successfully implemented and tested using the standardized I^2C protocol.

A series of three integrated sampling platforms were constructed on a poly(methylmethacrylate) support using the sequential aliquot deposition technique, and were then glucose-tested using the integrated micropotentiostat. This resulted in a response to glucose concentration that was again well-modeled by the Michaelis-Menten equation, but which unfortunately exhibited large degrees of variability. This may have resulted from several changes in the construction process used for this electrode type. Despite the variability, this result demonstrated the functioning of the complete integrated system and its ability to respond proportionally to glucose concentration, albeit on a varying transducer-to-transducer scale.

The most important goals of this project were met: a high-current, novel glucose transducer was successfully miniaturized and integrated with the existing e-Mosquito prototype and demonstrated a successful response to glucose concentrations during *in vitro* testing. The requisite supporting electronics to operate the transducer were also designed, built, and succesfully tested. The e-Mosquito concept is now a step closer to its envisioned final manifestation, and significantly closer to being amenable to partnership with private companies for marketing and manufacture. The principal patient-centred goals of the e-Mosquito, such as painless sampling, pseudo-continuous blood glucose level monitoring, and portability, are all shown to be practical and implementable by the current prototype. These goals are centred around improving patient compliance with blood glucose monitoring and improving data capture to improve insulin regimes. Tightened glycemic control, while concurrently reducing the risk of harmful hypoglycemic episodes, has been shown to improve mortality outcomes and reduce the absolutely debilitating and all-too-common complications of insulin-dependent diabetes.

Chapter 6

Future Work

This project was largely successful, and, as a result, bred certain other possible directions for future research pertaining to the e-Mosquito. In addition, some shortcomings were noted during this research that will require future investigation and refinement. The principal areas for future work are the manufacturing of the transducer electrodes, actuation methods for the microneedles, and improved body-area network (BAN) communication modalities.

As noted several times previously in this thesis, the response characteristics of the glucose transducers varied widely between individual units, though the sequential aliquot deposited electrodes were able to provide reasonably low levels of inter-electrode variability. The parameters that define the transfer function are I_{max} and K_m, and it was found that the variation in these parameters, coupled with the single-use (and hence uncalibratable) nature of the sensors, made the current incarnation of the sensor difficult to use in *in vivo* testing, though it functions well as a prototype. I_{max} is largely determined by the amount of enzyme that is accessible to the glucose in the solution to bind with, and K_m represents the affinity of the enzyme for the glucose in solution. Hence, it is felt that the variation in performance of the sensor stems largely from variations in the structure of the active film overlying the gold substrate, e.g., differences in the extent of aggregation of the enzyme and the iridium (Ir)/Ir oxide (IrOx) nanoparticles. This is somewhat expected, as the electrodes were constructed by hand. It is felt that more reproducible, rigorous manufacturing processes (such as mechanical aliquot deposition, or ideally spin-coating in a clean room) may result in more consistent films and hence more consistent sensor performance. Of note, recent developments in the

Birss group have resulted in GOx that is chemically coupled to the Au surface using highly-organized diazonium salts, resulting in transducers with inter-electrode variability in the range of $\pm 10\,\%$. This level of transducer-to-transducer error would be considered clinically insignificant. There is also ongoing research regarding the drying and aggregation issues that accompany mixed ethanolic-aqueous solutions. Another approach that is also being investigated to improve the surface organization of the electrodes involves growth of metal-oxide nanotubes on a metal surface. These tubes are then eroded into shallow 'nanocups', with the goal of placing GOx molecules in each of the well-ordered depressions.

Another area of interest is in the potential for result interference from other chemical species that are present in normal human blood. Research has been performed demonstrating that common chemicals such as ascorbic acid, uric acid, and acetaminophen do not interfere with this particular glucose transducer due to the Nafion® layer [73]. However, the effect of interferents that are structurally similar to glucose has not been investigated. The current transducer is intended to measure the concentration of the dextrotatory (D–) stereoisomer of glucose. Interference by molecules such as the levorotatory (L–) stereoisomer, other sugars such as dextrose or galactose, and complex starches and glycogens would be of great interest and such investigations would be relatively straightforward to perform.

The characterization of the custom miniaturized potentiostat is currently very limited, and would stand to be expanded. The current testing and demonstration is sufficient as a 'proof-of-concept' to show a predictable response to glucose concentration as well as the expected Michaelis-Menten kinetics. Characterization of the open-circuit potential stability of the potentiostat, the current amplification and current sourcing abilities, as well as a more in-depth analysis of the noise levels in the circuit would be of great value in refining both the potentiostat and the precision of its measurements.

The original e-Mosquito prototype used piezoelectric bending actuators to provide actuation of the microneedle. Two layers of piezoelectric material that exhibit different extents of deformation when a voltage is applied are bonded together, resulting in a bending cantilever

when electrically loaded. While this provided the actuation required, lengthy arm lengths (up to 20 mm) are required. In order to improve the size-profile of the e-Mosquito, improved methods of actuation are required that can be miniaturized more efficiently. Specifically, in-plane (as opposed to the current out-of-plane) actuation using shaped memory alloys (SMAs) are currently being investigated. These exotic metals can be made to remember a particular physical configuration and application of heat or electricity results in a return to that shape from the resting state. This approach is currently promising and appears to provide sufficient force to allow the microneedles to puncture skin.

Finally, improvements are constantly being considered to the communication system that, in the future, will comprise the BAN. The majority of devices that would receive and process the data produced by the e-Mosquito would reside on or near the patient's skin, with insulin pumps and wristwatch monitors being the most obvious. Hence, using a the patient's dermis as the means of transmission is being considered. This would reduce the electromagnetic pollution and interference of the device, and potentially result in increased security as well, requiring extremely close or physical contact to access data about the patient's health. Modulation of the encrypted data onto a very-low-voltage carrier signal applied to the patient's skin by the device is quite plausible, and bears further investigation for this application.

Bibliography

[1] J. D. Weiland, D. J. Anderson, and M. S. Humayun, "In vitro electrical properties for iridium oxide versus titanium nitride stimulating electrodes," *IEEE Transactions on Biomedical Engineering*, vol. 49, pp. 1574–1579, Dec. 2002.

[2] A. S. Jhas, H. Elzanowska, B. Sebastian, and V. Birss, "Dual oxygen and Ir oxide regeneration of glucose oxidase in nanostructured thin film glucose sensors," *Electrochimica Acta*, vol. 55, no. 26, pp. 7683–7689, 2010.

[3] S. A. Emr and A. M. Yacynych, "Use of polymer films in amperometric biosensors," *Electroanalysis*, 1995.

[4] S. F. G. Banting and C. H. Best, "The internal secretion of the pancreas," *The Jounral of Laboratory and Clinical Medicine*, vol. 7, pp. 251–266, Feb. 1922.

[5] J. E. Shaw, R. A. Sicree, and P. Z. Zimmet, "Global estimates of the prevalence of diabetes for 2010 and 2030," *Diabetes research and clinical practice*, vol. 87, no. 1, pp. 4–14, 2010.

[6] O. H. Franco, E. W. Steyerberg, F. B. Hu, J. Mackenbach, and W. Nusselder, "Associations of Diabetes Mellitus With Total Life Expectancy and Life Expectancy With and Without Cardiovascular Disease," *Archives of Internal Medicine*, vol. 167, pp. 1145–1151, June 2007.

[7] International Diabetes Federation, "IDF Diabetes Atlas."

[8] Centers for Disease Control, "Diabetes: Successes and Opportunities for Population-Based Prevention and Control," 2011.

[9] "Diabetes Mellitus & Hypoglycemia," in *Current Medical Diagnosis & Treatment 2010* (S. J. McPhee and M. A. Papadakis, eds.), pp. 1079–1122, McGraw-Hill.

[10] A. G. Ziegler, M. Hummel, M. Schenker, and E. Bonifacio, "Autoantibody appearance and risk for development of childhood diabetes in offspring of parents with type 1 diabetes: the 2-year analysis of the German BABYDIAB Study.," *Diabetes*, vol. 48, pp. 460–468, Mar. 1999.

[11] M. A. Atkinson and G. S. Eisenbarth, "Type 1 diabetes: new perspectives on disease pathogenesis and treatment," *The Lancet*, vol. 358, no. 9277, pp. 221–229, 2001.

[12] T. A. Sohn, K. A. Campbell, H. A. Pitt, and K. D. Lillemoe, "Quality of life and long-term survival after surgery for chronic pancreatitis," ... *Gastrointestinal surgery*,

2000.
[13] S. C. MD, D. T. MD, S. P. MD, R. S. M. PhD, S. G. MD, C. B. MD, P. P. MD, and M. F. MD, "Total pancreatectomy: Indications, different timing, and perioperative and long-term outcomes," *Surgery*, vol. 149, pp. 79–86, Jan. 2011.
[14] P. Jethwa, M. Sodergren, A. Lala, J. Webber, J. A. C. Buckels, S. R. Bramhall, and D. F. Mirza, "Diabetic control after total pancreatectomy," *Digestive and Liver Disease*, vol. 38, pp. 415–419, June 2006.
[15] N. Ewald and P. D. Hardt, "Diagnosis and treatment of diabetes mellitus in chronic pancreatitis," *World journal of gastroenterology: WJG*, 2013.
[16] "Type 2 Diabetes Mellitus," in *Williams Textbook of Endocrinology* (S. Melmed, K. S. Polonsky, P. R. Larsen, and H. M. Kronenberg, eds.), pp. 1371–1435, Saunders.
[17] "Insulin, Glucagon, and Diabetes Mellitus," in *Guyton & Hall: Textbook of Medical Physiology* (J. E. Hall, ed.), pp. 939–954, Saunders, 2011.
[18] D. Giugliano, A. Ceriello, and G. Paolisso, "Oxidative stress and diabetic vascular complications.," *Diabetes care*, 1996.
[19] X.-L. Du, D. Edelstein, L. Rossetti, I. G. Fantus, H. Goldberg, F. Ziyadeh, J. Wu, and M. Brownlee, "Hyperglycemia-induced mitochondrial superoxide overproduction activates the hexosamine pathway and induces plasminogen activator inhibitor-1 expression by increasing Sp1 glycosylation," *Proceedings of the National Academy of Sciences*, vol. 97, pp. 12222–12226, Oct. 2000.
[20] T. Nishikawa, D. Edelstein, X. L. Du, and S. Yamagishi, "Normalizing mitochondrial superoxide production blocks three pathways of hyperglycaemic damage," *Nature*, vol. 404, no. 6779, pp. 787–790, 2000.
[21] P. Poulsen, K. O. Kyvik, A. Vaag, and H. Beck-Nielsen, "Heritability of Type II (non-insulin-dependent) diabetes mellitus and abnormal glucose tolerance – a population-based twin study," *Diabetologia*, vol. 42, no. 2, pp. 139–145, 1999.
[22] P. S. Barnett and G. D. Braunstein, "Diabetes Mellitus," in *Cecil Essentials of Medicine*, pp. 697–720, Elsevier, 2010.
[23] R. C. Turner, R. R. Holman, C. A. Cull, and I. M. Stratton, "... blood-glucose control with sulphonylureas or insulin compared with conventional treatment and risk of complications in patients with type 2 diabetes (UKPDS 33)," *Lancet*, 1998.
[24] D. M. Nathan, "... and Complications (DCCT/EDIC) Study Research Group: Intensive diabetes treatment and cardiovascular disease in patients with type 1 diabetes," *N Engl J Med*, vol. 353, no. 25, pp. 2643–2653, 2005.
[25] A. L. Rosenbloom and R. Hanas, "Diabetic Ketoacidosis (DKA): Treatment Guidelines," *Clinical pediatrics*, vol. 35, pp. 261–266, May 1996.
[26] C. D. A. C. P. G. E. Committee, L. D. B. R. CDE, I. B. M. FRCPC, R. H. M. FRCPC, D. M. M. FRCPC, and V. W. M. FRCPC, "Canadian Journal of Diabetes," *Canadian Journal of Diabetes*, vol. 37, pp. S35–S39, Apr. 2013.
[27] D. E. DeWitt and I. B. Hirsch, "Outpatient Insulin Therapy in Type 1 and Type 2

Diabetes Mellitus: Scientific Review," *JAMA*, vol. 289, pp. 2254–2264, May 2003.
[28] T. W. Jones, P. Porter, and R. S. Sherwin, "Decreased epinephrine responses to hypoglycemia during sleep," *... England Journal of ...*, vol. 338, no. 23, pp. 1657–1662, 1998.
[29] P. E. Cryer, S. N. Davis, and H. Shamoon, "Hypoglycemia in diabetes," *Diabetes care*, 2003.
[30] R. P. Robertson, "Islet transplantation as a treatment for diabetes—a work in progress," *New England Journal of Medicine*, 2004.
[31] G. L. Warnock, N. M. Kneteman, E. A. Ryan, and A. Rabinovitch, "Long-term follow-up after transplantation of insulin-producing pancreatic islets into patients with type 1 (insulin-dependent) diabetes mellitus," *Diabetologia*, 1992.
[32] R. Alejandro, R. Lehmann, C. Ricordi, N. S. Kenyon, M. C. Angelico, G. Burke, V. Esquenazi, J. Nery, A. E. Betancourt, S. S. Kong, J. Miller, and D. H. Mintz, "Long-Term Function (6 Years) of Islet Allografts in Type 1 Diabetes," *Diabetes*, vol. 46, pp. 1983–1989, Dec. 1997.
[33] K. A. Johnson and R. S. Goody, "The original Michaelis constant: translation of the 1913 Michaelis–Menten paper," *Biochemistry*, vol. 50, no. 39, pp. 8264–8269, 2011.
[34] J. B. S. H. George Edward Briggs, "A Note on the Kinetics of Enzyme Action," *Biochemical journal*, vol. 19, no. 2, p. 338, 1925.
[35] L. C. Clark and C. Lyons, "Electrode systems for continuous monitoring in cardiovascular surgery," *Annals of the New York Academy of ...*, 1962.
[36] J. Wang, "Electrochemical glucose biosensors," *Chemical reviews*, 2008.
[37] H. J. Hecht, H. M. Kalisz, J. Hendle, and R. D. Schmid, "Crystal Structure of Glucose Oxidase from Aspergillus niger Refined at 2· 3 Å Reslution," *Journal of molecular ...*, vol. 229, no. 1, pp. 153–172, 1993.
[38] D. S. Goodsell, "Glucose Oxidase," *RCSB Protein Data Bank*, May 2006.
[39] G. G. Guilbault and G. J. Lubrano, "An enzyme electrode for the amperometric determination of glucose," *Analytica chimica acta*, 1973.
[40] H. A. Krebs, "Chemical composition of blood plasma and serum," *Annual review of biochemistry*, 1950.
[41] F. Palmisano, D. Centonze, and A. Guerrieri, "... interference-free biosensor based on glucose oxidase electrochemically immobilized in a non-conducting poly (pyrrole) film for continuous subcutaneous monitoring ...," *Biosensors and ...*, 1993.
[42] E. M. A. Irhayem, *Fabrication and Characterization of Nanoparticulate and Related Ir Oxide-Based Glucose Biosensors*. PhD thesis, University of Calgary, 2004.
[43] D. A. Gough, J. Y. Lucisano, and P. Tse, "Two-dimensional enzyme electrode sensor for glucose," *Analytical Chemistry*, 1985.
[44] A. Cass, G. Davis, G. D. Francis, and H. Hill, "Ferrocene-mediated enzyme electrode for amperometric determination of glucose," *Analytical ...*, 1984.
[45] J. E. Frew and H. Hill, "Electrochemical biosensors," *Analytical Chemistry*, 1987.

[46] J. Liu, A. Chou, W. Rahmat, M. N. Paddon-Row, and J. J. Gooding, "Achieving Direct Electrical Connection to Glucose Oxidase Using Aligned Single Walled Carbon Nanotube Arrays," *Electroanalysis*, vol. 17, no. 1, pp. 38–46, 2005.

[47] R. O. Potts, J. A Tamada, and M. J Tierney, "Glucose monitoring by reverse iontophoresis," *Diabetes/Metabolism Research and Reviews*, vol. 18, no. S1, pp. S49–S53, 2002.

[48] C. T.-S. Ching, T.-P. Sun, S.-H. Huang, H.-L. Shieh, and C.-Y. Chen, "A Mediated Glucose Biosensor Incorporated with Reverse Iontophoresis Function for Noninvasive Glucose Monitoring," *Annals of Biomedical Engineering*, vol. 38, pp. 1548–1555, Jan. 2010.

[49] T. Vering, S. Adam, H. Drewer, C. Dumschat, R. Steinkuhl, M. Knoll, A. Schulze, and E. G. Siegel, "Wearable microdialysis system for continuous in vivo monitoring of glucose," *The Analyst*, vol. 123, no. 7, pp. 1605–1609, 1998.

[50] J. C. Pickup, F. Hussain, N. D. Evans, and N. Sachedina, "In vivo glucose monitoring: the clinical reality and the promise," *Biosensors and Bioelectronics*, vol. 20, pp. 1897–1902, Apr. 2005.

[51] P. Trinder, "Determination of blood glucose using an oxidase-peroxidase system with a non-carcinogenic chromogen," *Journal of clinical pathology*, 1969.

[52] M. C. Moreno-Bondi, O. S. Wolfbeis, M. J. P. Leiner, and B. P. H. Schaffar, "Oxygen optrode for use in a fiber-optic glucose biosensor," *Analytical Chemistry*, vol. 62, pp. 2377–2380, Nov. 1990.

[53] W. Trettnak and O. S. Wolfbeis, "Fully reversible fibre-optic glucose biosensor based on the intrinsic fluorescence of glucose oxidase," *Analytica chimica acta*, vol. 221, pp. 195–203, 1989.

[54] S. De Marcos, J. Galindo, J. F. Sierra, and J. Galban, "An optical glucose biosensor based on derived glucose oxidase immobilised onto a sol–gel matrix," *Sensors and Actuators B ...*, vol. 57, no. 1-3, pp. 227–232, 1999.

[55] J. C. Pickup, F. Hussain, N. D. Evans, O. J. Rolinski, and D. J. S. Birch, "Fluorescence-based glucose sensors," *Biosensors and Bioelectronics*, vol. 20, pp. 2555–2565, June 2005.

[56] M. M. F. Choi, W. S. H. Pang, X. Wu, and D. Xiao, "An optical glucose biosensor with eggshell membrane as an enzyme immobilisation platform," *The Analyst*, vol. 126, no. 9, pp. 1558–1563, 2001.

[57] R. Gill, L. Bahshi, R. Freeman, and I. Willner, "Optical Detection of Glucose and Acetylcholine Esterase Inhibitors by H2O2-Sensitive CdSe/ZnS Quantum Dots," *Angewandte Chemie*, vol. 120, pp. 1700–1703, Feb. 2008.

[58] L. Heinemann and G. Schmelzeisen-Redeker, "Non-invasive continuous glucose monitoring in Type I diabetic patients with optical glucose sensors," *Diabetologia*, vol. 41, no. 7, pp. 848–854, 1998.

[59] R. Yue and Y. Wang, "Microneedle array chip, device and patch for transdermal drug

delivery utilizing the same, and preparation method thereof." United States Patent Office, Sept. 2011.
[60] M. Stiene, T. Richter, J. Allen, and J. McAleer, "Analyte measurement." United States Patent Office, May 2004.
[61] S. H. Kravitz, D. Ingersoll, C. Schmidt, and J. Flemming, "Method to Fabricate Hollow Microneedle Arrays." United States Patent Office, Nov. 2006.
[62] M. D. Black, A. M. Chambers, R. Chambers, and N. Okulan, "Body fluid sampling/fluid delivery device." United States Patent Office, Dec. 2011.
[63] M. R. Prausnitz, M. G. Allen, and I.-j. Gujral, "Microneedle Device for Extraction and Sensing of Bodily Fluids." United States Patent Office, Mar. 2008.
[64] M. Jose, J. Spoonhower, J. Agostinelli, L. Demejo, and K. Sarbadhikari, "Replaceable Microneedle Cartridge for Biomedical Monitoring." United States Patent Office, 2011.
[65] J. G. Aceti, S. E. McBride, R. M. Moroney, C. C. Gregory, and P. J. Zanzucchi, "Autonomous, Ambulatory Analyte Monitor or Drug Delivery Device." United States Patent Office, Feb. 2006.
[66] W. L. Clarke, D. Cox, L. A. Gonder-Frederick, W. Carter, and S. L. Pohl, "Evaluating Clinical Accuracy of Systems for Self-Monitoring of Blood Glucose," *Diabetes care*, vol. 10, pp. 622–628, Sept. 1987.
[67] American Diabetes Association, "Screening for Type 2 Diabetes," *Diabetes care*, vol. 27, pp. s11–s14, Jan. 2004.
[68] D. McReery and W. Agnew, *Neural Prostheses: Fundamental studies*. New Jersey: Prentice Hall, 1990.
[69] J. D. Weiland and D. J. Anderson, "Chronic neural stimulation with thin-film, iridium oxide electrodes," *IEEE Transactions on Biomedical Engineering*, vol. 47, pp. 911–918, July 2000.
[70] C. Bock and V. I. Birss, "Comparison of Ir oxide film redox kinetics in sulfuric and p-toluene sulfonic acid solutions," *Electrochimica Acta*, vol. 46, no. 6, pp. 837–849, 2001.
[71] H. Campbell, H. Elzanowska, and V. I. Birss, "Towards a reliable and high sensitivity O2-independent glucose sensor based on Ir oxide nanoparticles," *Biosensors and Bioelectronics*, 2012.
[72] J. A. Cox and R. K. Jaworski, "Voltammetric reduction and determination of hydrogen peroxide at an electrode modified with a film containing palladium and iridium," *Analytical Chemistry*, vol. 61, no. 19, pp. 2176–2178, 1989.
[73] H. Elzanowska, E. A. Irhayem, and B. Skrzynecka, "Hydrogen Peroxide Detection at Electrochemically and Sol-Gel Derived Ir Oxide Films," 2004.
[74] J. Wagner, C. Malchoff, and G. Abbott, "Invasiveness as a barrier to self-monitoring of blood glucose in diabetes," *Diabetes technology & ...*, 2005.
[75] L. Blonde and A. J. Karter, "Current evidence regarding the value of self-monitored blood glucose testing," *The American journal of medicine*, 2005.

[76] A. J. Karter, L. M. Ackerson, and J. A. Darbinian, "Self-monitoring of blood glucose levels and glycemic control: the Northern California Kaiser Permanente Diabetes registry∗," *The American journal of . . .*, vol. 111, no. 1, pp. 1–9, 2001.

[77] UK Prospective Diabetes Study Group, "Effect of intensive blood-glucose control with metformin on complications in overweight patients with type 2 diabetes (UKPDS 34). UK Prospective Diabetes Study (UKPDS) Group.," *Lancet*, vol. 352, no. 9131, pp. 854–865, 1998.

[78] C. E. Shannon, "Communication in the Presence of Noise," in *Proceedings of the IRE*, pp. 10–21, IEEE, 1949.

[79] C. L. Phillips, J. M. Parr, and E. A. Riskin, "The Fourier Transform," in *Signals, Systems, and Transforms*, pp. 199–274, 2003.

[80] D. A. Gough, K. Kreutz-Delgado, and T. M. Bremer, "Frequency Characterization of Blood Glucose Dynamics," *Annals of Biomedical Engineering*, vol. 31, no. 1, pp. 91–97.

[81] J.-F. Yale, "Nocturnal hypoglycemia in patients with insulin-treated diabetes," *Diabetes research and clinical practice*, vol. 65, pp. S41–S46, Sept. 2004.

[82] T. Veneman, A. Mitrakou, M. Mokan, P. Cryer, and J. Gerich, "Induction of Hypoglycemia Unawareness by Asymptomatic Nocturnal Hypoglycemia," *Diabetes*, vol. 42, pp. 1233–1237, Sept. 1993.

[83] J. A. Guay, "Closed-Loop Insulin Delivery," Master's thesis, University of Alberta Press, Edmonton, AB, 2001.

[84] G. Gattiker, *Designing a BioMEMS-based Blood Sampler.* PhD thesis, University of Calgary Press, 2006.

[85] G. Thomas, "Electronic Mosquito: A Feedback-Controlled Semi-Invasive Microsystem for Glucose Monitoring," Master's thesis, University of Calgary Press, Calgary, June 2009.

[86] G. E. Gattiker, K. V. I. S. Kaler, and M. P. Mintchev, "Electronic Mosquito: designing a semi-invasive Microsystem for blood sampling, analysis and drug delivery applications," *Microsystem Technologies*, vol. 12, pp. 44–51, Sept. 2005.

[87] P. Agache and P. Humbert, *Measuring the skin.* Non-invasive investigations, physiology, normal constants, Berlin: Springer, 2004.

[88] W. Montagna and P. F. Parakkal, *The structure and function of skin.* Academic Press, 1974.

[89] "Cross Section of Skin," *The Visual Dictionary.*

[90] T. D. Jones, K. Kaler, M. Fattouche, and M. P. Mintchev, "Wireless Communication and Control System for Portable Micro-Electromechanical Device for Real-Time Blood Sampling and Glucose Analysis (Electronic Mosquito)," *Information Technologies & Knowledge*, vol. 3, no. 3, p. 223, 2009.

[91] Nordic Semiconductor, "nRF24AP1 Datasheet." Nordic Semiconductor, Sept. 2006.

[92] Sigma-Aldrich, "Glucose Oxidase G6641 Product Specification," Nov. 2010.

[93] O. C. Keller and J. Buffle, "Voltammetric and Reference Microelectrodes with Inte-

grated Microchannels for Flow through Microvoltammetry. 1. The Microcell," *Analytical Chemistry*, vol. 72, pp. 936–942, Mar. 2000.

[94] R. Petrucci, F. G. Herring, J. Madura, and C. Bissonnette, *General Chemistry. Principles and Modern Applications*, Prentice Hall, 10 ed., Feb. 2010.

[95] Sigma-Aldrich, "Phosphate Buffered Saline Tablets P4417 Product Specification," June 2011.

[96] J. M. Burkstrand, "Metal-polymer interfaces: Adhesion and x-ray photoemission studies," *Journal of Applied Physics*, vol. 52, no. 7, p. 4795, 1981.

[97] M. Ammam and J. Fransaer, "A study on electrodeposition of glucose oxidase from low conductivity solutions," *Electrochimica Acta*, 2010.

[98] E. N. El Sawy and V. I. Birss, "Nano-porous iridium and iridium oxide thin films formed by high efficiency electrodeposition," *J. Mater. Chem.*, vol. 19, no. 43, p. 8244, 2009.

[99] Princeton Applied Research, "PARSTAT 4000," pp. 1–8, Oct. 2012.

[100] Y.-H. Sheu and C.-Y. Huang, "A Portable Potentiostat for Electrochemical Sensors," *Springer*, pp. 538–542, 2007.

[101] M. D. Steinberg and C. R. Lowe, "A micropower amperometric potentiostat," *Sensors and Actuators B: Chemical*, vol. 97, no. 2, pp. 284–289, 2004.

[102] P. Steffan and R. Vrba, "Single chip potentiostat measurement system," *Springer*, pp. 653–659, 2007.

[103] M. Stanacevic, K. Murari, A. Rege, G. Cauwenberghs, and N. V. Thakor, "VLSI Potentiostat Array With Oversampling Gain Modulation for Wide-Range Neurotransmitter Sensing," *Biomedical Circuits and Systems, IEEE Transactions on*, vol. 1, pp. 63–72, Mar. 2007.

[104] A. Bandyopadhyay, G. Mulliken, G. Cauwenberghs, and N. Thakor, "VLSI potentiostat array for distributed electrochemical neural recording," *Circuits and Systems, 2002. ISCAS 2002. IEEE International Symposium on*, vol. 2, pp. –II–743, 2002.

[105] M. M. Ahmadi and G. A. Jullien, "A very low power CMOS potentiostat for bioimplantable applications," in *System-on-Chip for Real-Time Applications, 2005. Proceedings. Fifth International Workshop on*, pp. 184–189, IEEE, 2005.

[106] M. M. Ahmadi and G. A. Jullien, "Current-Mirror-Based Potentiostats for Three-Electrode Amperometric Electrochemical Sensors," *IEEE Transactions on Circuits and Systems I: Regular Papers*, vol. 56, pp. 1339–1348, July 2009.

[107] H. S. Narula and J. G. Harris, *Integrated VLSI potentiostat for cyclic voltammetry in electrolytic reactions*. IEEE, 2004.

[108] C. K. Alexander and M. N. O. Sadiku, "Operational Amplifiers," in *Fundamentals of Electric Circuits*, McGraw-Hill, 2007.

[109] A. Hickling, "Studies in electrode polarisation. Part IV.—The automatic control of the potential of a working electrode," *Transactions of the Faraday Society*, vol. 38, pp. 27–33, 1942.

[110] A. J. Bard and L. R. Faulkner, *Electrochemical methods : fundamentals and applications*. New York: John Wiley, 2nd ed. ed., 2001.
[111] M. Integrated, "MAX856 Datasheet." Maxim Integrated.
[112] Texas Instruments, "TLE2426 Datasheet." Texas Instruments, May 1998.
[113] M. Z. Shrayyef and J. E. Gerich, "Normal Glucose Homeostasis," in *Principles of Diabetes Mellitus*, pp. 19–35, Boston, MA: Springer US, Nov. 2009.
[114] H. Yang, S. K. Kang, C. A. Choi, H. Kim, D.-H. Shin, Y. S. Kim, and Y. T. Kim, "An iridium oxide reference electrode for use in microfabricated biosensors and biochips," *Lab on a Chip*, vol. 4, no. 1, p. 42, 2004.
[115] J. Wang, "Glucose biosensors: 40 years of advances and challenges," *Electroanalysis*, 2001.
[116] B. Hill, "Accu-Chek Advantage: Electrochemistry for Diabetes Management," *Current Separations*, pp. 1–4, Aug. 2005.
[117] Texas Instruments, "LM741 Operational Amplifier Datasheet."

Appendix A

Michaelis Menten Sensitivity Analysis

The results of the glucose tests outlined in Chapter 3 show that the Michaelis-Menten model fits the observed experimental results to a high degree of accuracy. The Michaelis-Menten model (Section 1.3), as it applies to this system, is expressed mathematically as:

$$I = \frac{I_{max} \cdot [Glucose]}{K_m + [Glucose]} \tag{A.1}$$

The output current produced by the sensor responds to the concentration of glucose in a non-linear manner that is governed by the parameters I_{max} and K_m. Since these model parameters are a reflection of the physical properties of the enzyme layer on the substrate, some variation of these parameters between individual physical transducers is expected, and is indeed observed in the results. This variation gives rise to a significant and unpredictable error.

Understanding the effect that variation in these parameters has on the error in the result provided by the entire sensor system is important in order to determine how tightly K_m and I_{max} need to be controlled to produce transducers of acceptable accuracy. Sensitivity analysis is the term given to techniques that yield information about the magnitude and mathematical order of the relationship between a function parameter and the function result. In this case, the function is the mathematical model of the entire sensor system, and the parameters are the Michaelis-Menten constants, I_{max} and K_m.

Modelling the error as it affects the entire system, from true glucose concentration to transducer, processing electronics, and finally the reported glucose concentration, requires

two applications of the Michaelis-Menten model. Figure A.1 shows this schematically. The first use models the physical process that occurs, where current is produced by the physical phenomenon of glucose oxidation by the glucose oxidase (GOx) enzyme. The sensor device then uses the inverse Michaelis-Menten model ($\mathcal{M}^{-1}$) to convert the current generated by the transducer into a glucose concentration. In effect, the sensor is described by the following transforms:

$$G' = \mathcal{M}^{-1}[\mathcal{M}(G)] \tag{A.2}$$

A problem arises because the values of the Michaelis-Menten parameters (K_m and I_{max}) are different in the forward transform as opposed to the reverse transform. The parameters in the forward transform are the 'true' parameters and they reflect the actual operation of the physical transducer. In practice these are unknown, as each transducer can only be used once, and hence they cannot be measured prior to patient use. The parameters in the reverse transform (written here as K'_m and I'_{max}) are the values stored in the sensor software as a "best-estimate" of the transducer's real parameters. When the best-estimate is equal to the true value of the parameters, there is no error in the output from this source. This ideal situation can never exist, and the best-estimate parameters are the average values of large batch of test transducers used specifically for the purposes of calibration.

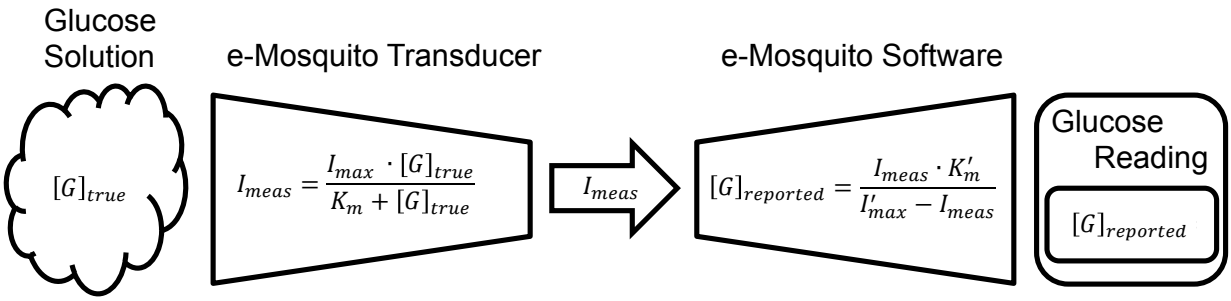

Figure A.1: Model of the complete e-Mosquito system used for error analysis. The transducer is the GOx-coated electrode that produces an electrical current I_{meas} that is proportional to the glucose concentration $[G]_{true}$ in the sample. The software takes the measured current and converts it back to a glucose level ($[G]_{measured}$) with its internally-programmed calibration parameters I'_{max} and K'_m. This is a reproduction of the same figure used in Chapter 3.

A.1 Algebraic Inspection

The most intuitive approach to determining the sensitivity of the output to variations in the parameters I_{max} and K_m is to directly manipulate and inspect the mathematical model of the system. The Michaelis-Menten model for this particular transducer is:

$$\mathcal{M} = I = \frac{I_{max} \cdot [Glucose]}{K_m + [Glucose]} \tag{A.3}$$

This is quite straightforward to interpret: the result is more sensitive to I_{max} than to K_m. Doubling the value of I_{max} will result in the output current, and hence the reported glucose reading, also doubling. This is equivalent to a 100 % error. Converseley, doubling K_m will not equivalently halve the output unless K_m is much bigger than the glucose levels being measured.

As noted above, the model is built from the combination of the standard Michaelis-Menten equation and its inverse:

$$\mathcal{M}^{-1} = [Glucose]' = \frac{I \cdot K'_m}{I'_{max} - I} \tag{A.4}$$

This clearly shows exactly the reverse relationship! In this case, the output is more sensitive to K'_m than I'_{max}. The overall system cannot be easily characterized by inspection of the underlying equations as the combination of the two is nonlinear and not superimposable. Therefore, the two equations can be combined algebraically, which results in:

$$[Glucose]' = \frac{K'_m \cdot I_{max} \cdot [Glucose]}{(I_{max} - I'_{max}) \cdot [Glucose] - I'_{max} \cdot K_m} \tag{A.5}$$

When this expression is combined with the equation for percent error, the resulting expression is shown in Equation A.6

$$PE = \frac{[G]_{true} \cdot (I_{max} - I'_{max}) + (I_{max}K'_m - I'_{max}K_m)}{I_{max}K'_m} \times 100\,\% \tag{A.6}$$

The dependence of the percent error on K_m is linear while the dependence of the error on I_{max} is non-linear with respect to glucose concentration. Equation A.6 shows this clearly. When I_{max} is equal to I'_{max}, all dependence of the error on $[G]_{true}$ disappears. This means that for a fixed deviation in the K_m of a transducer from the calibration K_m of the device, the percentage error is independent of the glucose concentration, while a fixed deviation of I_{max} from the calibration value will result in higher percent error at high glucose concentrations.

A.2 One Factor At A Time (OFAT)

The simplest heuristic approach to analyzing parameter sensitivity is to vary each parameter independently of each other and observe the resulting error. This provides information regarding which parameters are more and less sensitive to error, and whether the relationship between the parameter error and the result error is linear or exponential.

Geometrically, this is equivalent to envisioning the transducers as existing in a two-dimensional cartesian 'space' of possible sensors, with the parameter I_{max} on the horizontal

axis and the parameter K_m on the vertical axis. The first step of this process involves selecting a 'reference sensor' in the sensor space, i.e., a particular value of these two parameters that serves as the origin of this two-dimensional space. The two parameters are then varied from the reference values independently of each other (the 'error') and the predicted sensor result is compared to the calculated 'true' sensor output. This is shown in Figure A.2 at steps of 5%, 10%, and 20% error deviation in both parameters. The red line indicates the ideal response of an error-free sensor (always a straight line of $m = 1$) and the blue line indicates the response of the sensor with the indicated parameter error. Note that these plots only show the commonly accepted clinically-relevant range of 0 mM to 25 mM where the sensor will operate.

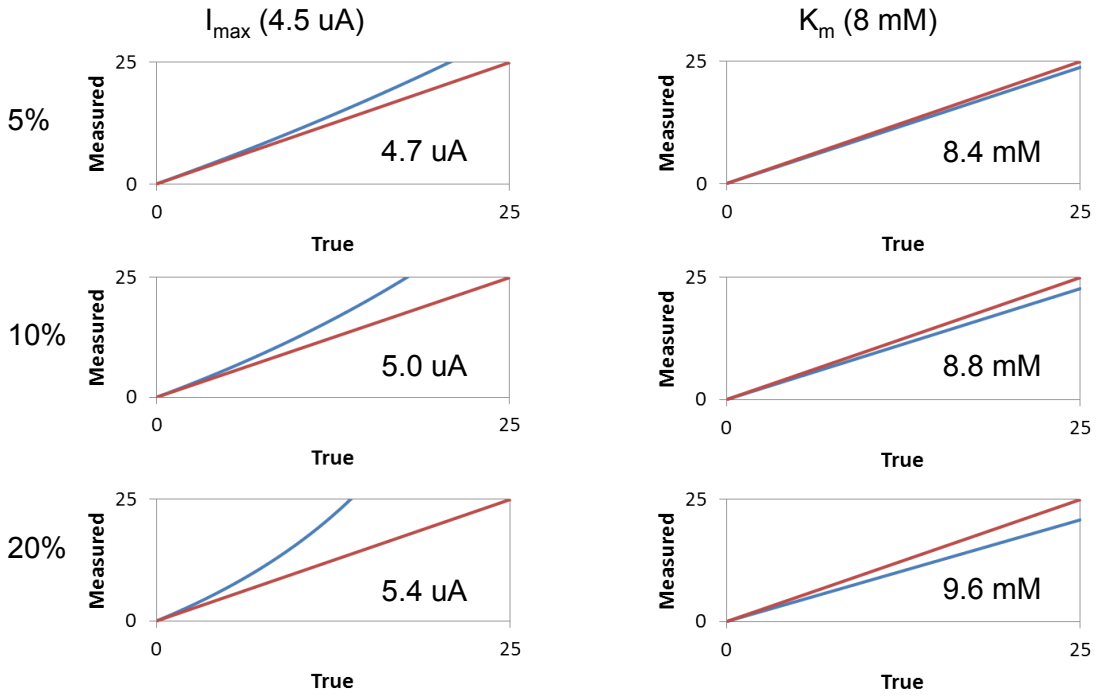

Figure A.2

These plots give an overall impression of the effect that each of the two parameters has

on the total error of the system. The K_m parameter has a linear and minimal effect on the measurement error. The I_{max} parameter, however, shows a significantly larger and non-linear effect on measurement error, especially as glucose concentration increases.

The primary importance of this result is to indicate that even fairly small deviations in the true value of I_{max} relative to the programmed calibration value of I'_{max} will lead to a sensor with measurement error so large as to be unusable. However more error can be permitted in the value of K_m as it has a smaller and more linear effect on the resultant measurement error. A 5% deviation in K_m leads to a 5% error in measurement output, while a 10% deviation leads to a 10% error and so on.

Appendix B

Transimpedance Amplifier

The most important function of a potentiostat is directly indicated in the name — to hold the electrical potential of the solution static or stable. This means that the potential difference between the reference electrode and the working electrode must be strictly controlled at all times. If the desired working potential of the potentiostat design used here is designated as V_w, then the circuit controls the reference electrode (RE) to $-V_w$ via the buffering amplifier, and the working electrode (WE) is connected directly to ground through an ideal ammeter (Figure B.1). In this way the voltage difference between the WE and the RE is $0--V_w = V_w$; this is the desired result.

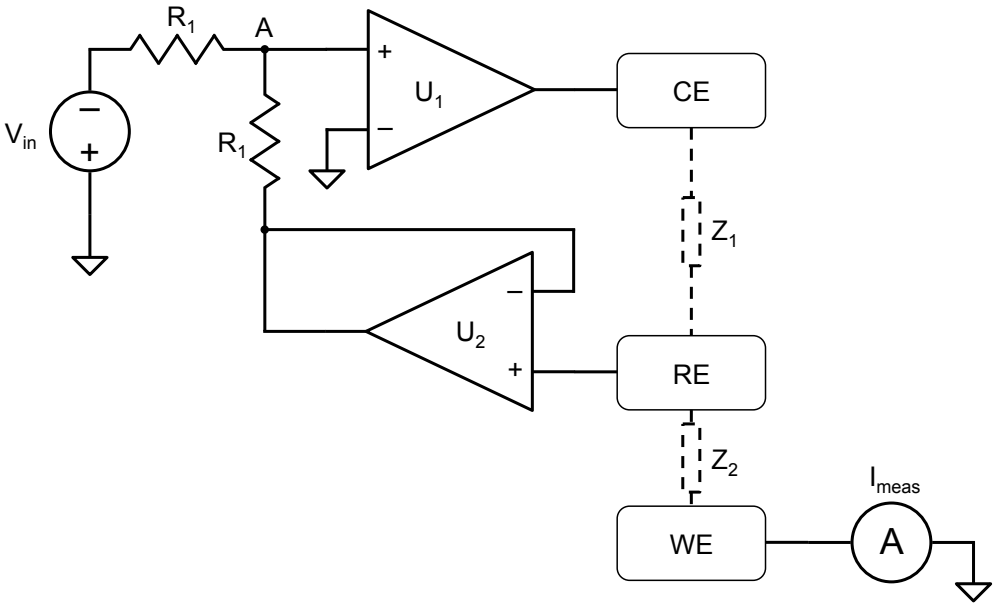

Figure B.1: Conceptual circuit diagram of the micropotentiostat circuit.

The measured variable of interest is the current flowing out of the WE and into ground, hence the ammeter. The most direct way to measure current is by forcing it to flow through a known resistance and then measuring the resulting electrical potential that is generated. In the case of the potentiostat designed here this method will have the unintended effect of introducing a potential drop (V_{drop}) that varies with the output current between the WE and ground. This is shown in Figure B.2. The voltage difference between the WE and the RE then becomes $V_{drop} - -V_w = V_{drop} + V_w$. Since it is imperative that the WE-RE potential be maintained constant for the purposes of having a predictable chemical reaction, this is unacceptable.

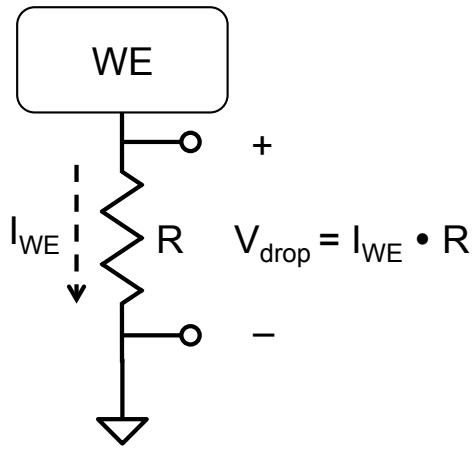

Figure B.2: Illustration of the variable voltage drop between the working electrode and ground.

The solution is a simple circuit named a transimpedance amplifier (TA). Current fed into a TA is converted to a proportional voltage by a gain factor $-R$. The second useful attribute is that the potential of the input is at virtual ground — hence 0 V as required by the potentiostat. The basic TA circuit is shown in Figure B.3.

The easiest way to understand the functioning of this subcircuit is by applying the ideal operational amplifier conditions:

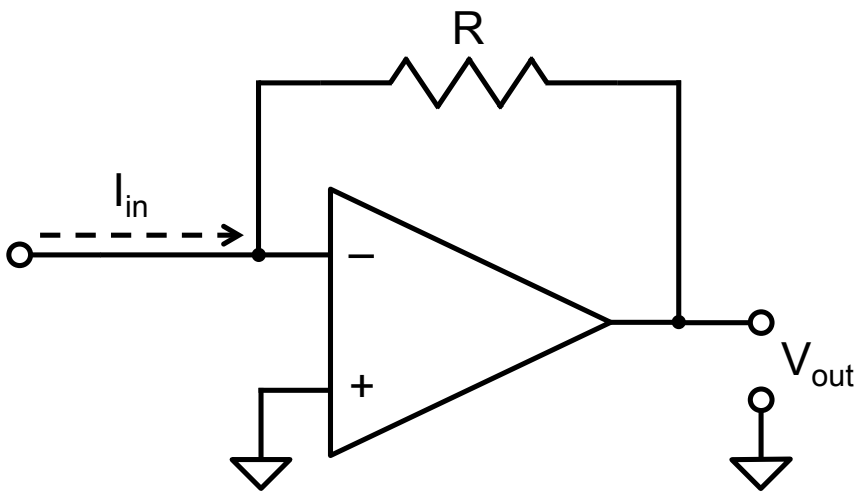

Figure B.3: Schematic of a current-to-voltage converter — a transimpedance amplifier. The input current flows entirely through the resistor R, giving rise to a voltage of $I_{in} \cdot R$ at the output.

- Infinite input impedance
- Infinite open-loop gain
- Infinite bandwidth

The principle effect of these constraints is that the output acts to keep the voltage difference between the two inputs at zero, and no current flows in to either input. Strictly speaking, these conditions can only be met in a feedback configuration such as that found in the TA circuit. From this it follows that all of the current entering the circuit (I_{in}) must flow through the resistance R, resulting in a voltage drop of $I_{in} \cdot R$. Since the second effect is that the two inputs are at the same voltage and the non-inverting (+) input is at ground, the input-side of resistor R is also at ground — a virtual ground. Hence the potential at the output is $V_{out} = 0 - (-I_{in} \cdot R) = -I_{in} \cdot R$. Thus the gain factor of the TA is simply the value of the resistor in the feedback loop. A properly connected analog-to-digital converter (ADC) can be used to digitally read the output potential and software can then convert that to the original current (provided that the value of R is known). The other requirement for this circuit is also met as the input is held at ground voltage, hence if this is connected directly to the working electrode, it too will maintain ground potential.

Of course real operational amplifiers are not ideal amplifiers, and cannot have infinite or zero values for any parameters. However in this application, a high-end real operational amplifier is more than sufficient for the task. While input impedance is not infinite, it is immensely large; typical input bias currents are on the order of 10 nA (for instance the LM741 datasheet lists a typical input current of 3.0 nA [117]). These currents are approximately 30,000 $\times$ lower than the transducer output currents and hence the error produced is acceptably low.

The open-loop gain of a real operational amplifier is also not infinite. Returning to the LM741, the open-loop gain is between 50,000 and 200,000. This gives a loop gain of $50 \times 10^3 \cdot R$ where R is in the range of $10k\Omega$ to $50k\Omega$. This results in a very large loop gain, meaning that the system gain is determined essentially exclusively by the feedback gain, and not by the open-loop gain.

Finally, the bandwidth requirement of the sensor is very low: output change occurs over the course of seconds to minutes, while real operational amplifiers (such as the LM741) have bandwidths of kHz to MHz.

Appendix C

Construction Method Flowchart

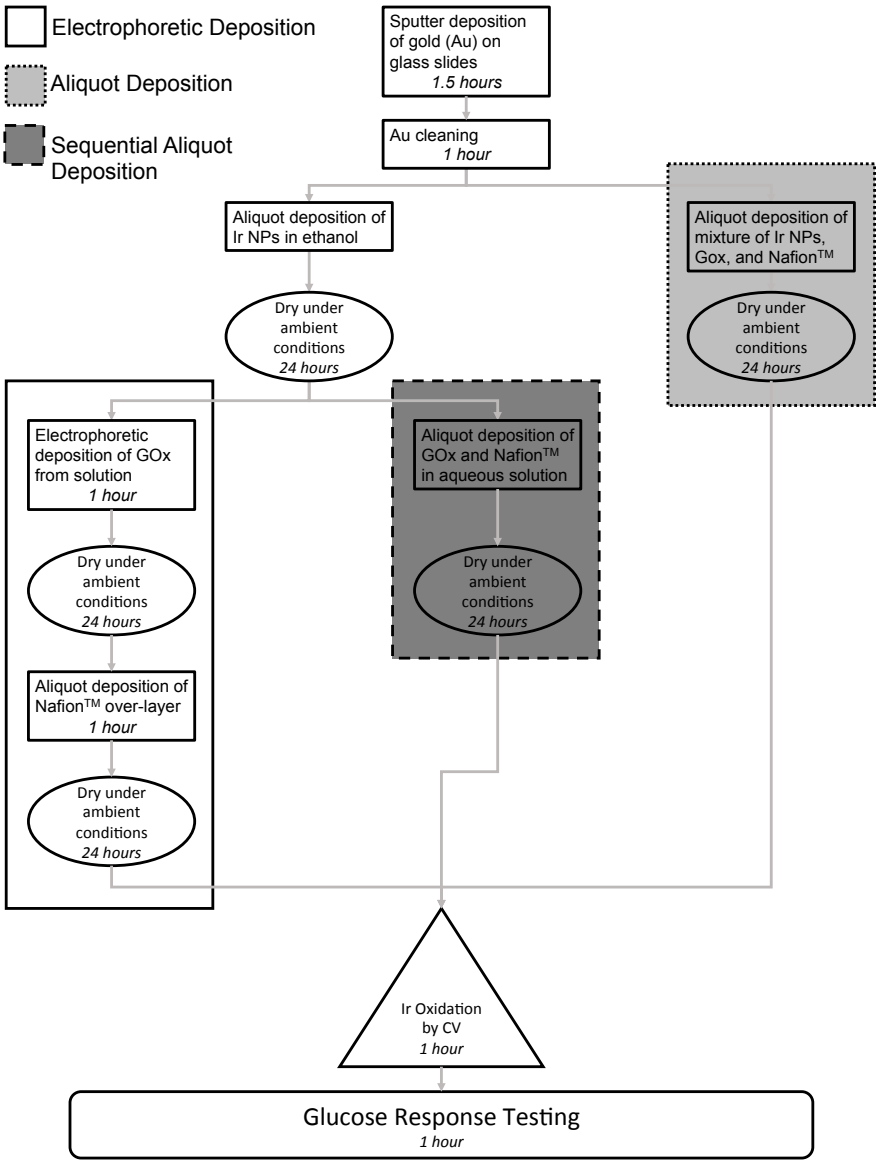

Figure C.1: Flowchart showing the various construction methods used to create transducers, and the approximate time required for each step.

Appendix D

Component List

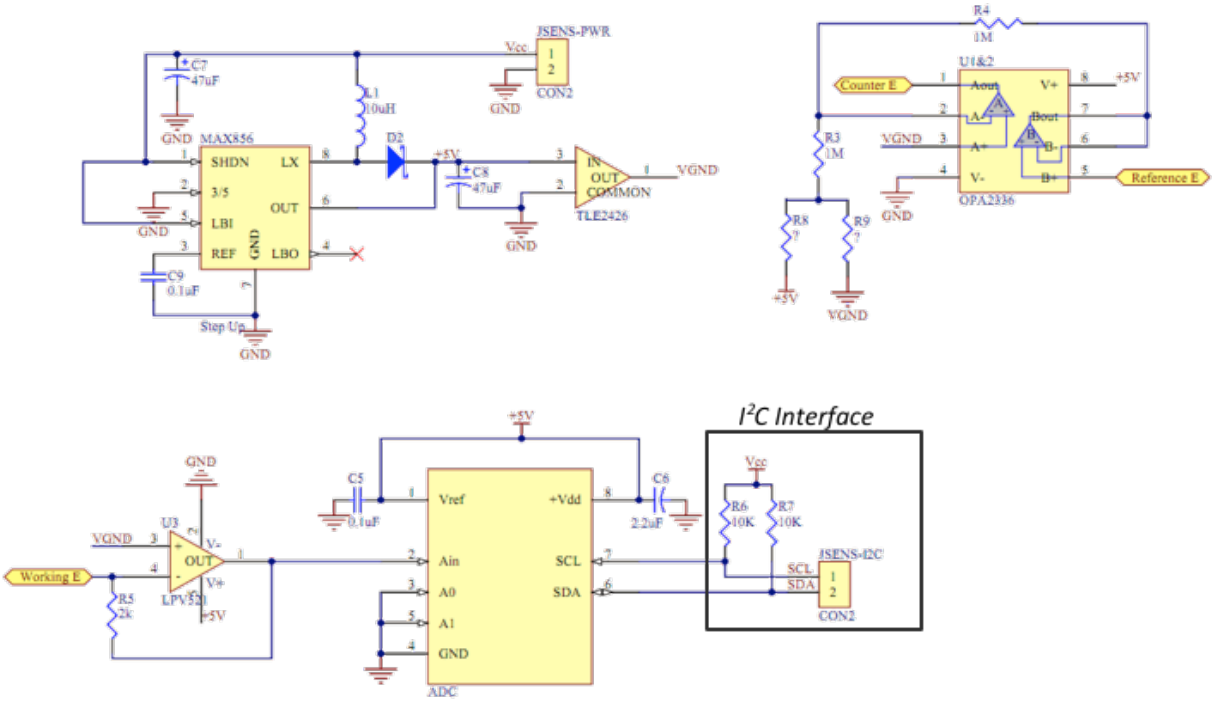

Figure D.1: Final circuit design for the e-Mosquito potentiostat.

- **U1/U2** — Texas Instruments OPA2336 Operational Amplifiers (2 OPA336 in a single package)
- **U3** — Texas Instruments LPV521 Operational Amplifier
- **U4** — Maxim Integrated MAX851 Regulated, Negative Charge Pump Power Supply
- **U5** — Texas Instruments TLE2426 Rail Splitter Precision Virtual Ground

- **ADC** — Texas Instruments ADS7823 12-bit I2C Analog-to-Digital Converter
- **D2** — Fairchild Semiconductor 1N5817 Schottky Diode
- **R3/R4** — 1 MΩ Resistor, 1% tolerance
- **R5** — 49.9 kΩ Resistor, 1% tolerance (a 2 kΩ 1% resistor was used in an early testing phase)
- **R6/R7** — 10 kΩ Resistor, 5% tolerance
- **R8/R9** — Resistor, 1% tolerance (the resistances were varied to attain the desired input potential)
- **C5/C9** — 0.1 µF Ceramic Capacitor, 10% tolerance
- **C6** — 2.2 µF Electrolytic Capacitor, 20% tolerance
- **C7/C8** — 47 µF Electrolytic Capacitor, 20% tolerance
- **L1** — 10 µH Inductor, 20% tolerance
- **CON1/CON2** — Female 4-pin Jumper Header